Dye Sensitized Solar Cells Fabricated from Obliquely Sputtered Nanoporous TiO_2 Thin Films: Characterization, Electron Transport and Lifetime Studies

By

Sebastian M. Waita

A thesis submitted in fulfillment of the requirements for the degree of Doctor of Philosophy (Physics) of the University of Nairobi.

Department of Physics, University of Nairobi

January, 2008

DECLARATION

This thesis is my original work and has not been presented for examination in any other University.

Sebastian M. Waita

Sign.....

Date 10.9.2008

This work has been presented for examination with our approval as supervisors.

1. Prof. B.O. Aduda

   Dept of Physics

   University of Nairobi

   Sign:.....

   Date: 11/9/2008

2. Dr. J. M. Mwabora

   Dept of Physics

   University of Nairobi

   Sign:.....

   Date: 10.9.2008

DEDICATION

To my beloved wife Jedidah who had to patiently and willingly accept to remain alone at times while I studied. And to our children, Emmanuel and Ndinda who had to miss dad for long periods

To my mother Esther for her care and love

To the memory of my father Waita

ACKNOWLEDGEMENTS

I am grateful to my Kenyan supervisors Prof. B. O. Aduda and Dr. J. M. Mwabora; my Swedish advisors Prof Sten-Eric Lindquist, Prof. G. Niklasson, Dr. G. Boschloo, Prof. Anders Hagfeldt and Prof. C.G. Granqvist for their encouragement, guidance, constructive criticism and helpful suggestions which made this work a success. I thank Prof. B. O. Aduda, for support in administrative matters pertaining to this work during his tenure as chairman of the Department of Physics, University of Nairobi.

I am greatly indebted to the International Science Programmes (ISP), Uppsala University, Sweden for providing fellowships to visit Uppsala University, Sweden. Prof. Anders Hagfeldt and Prof. C.G. Granqvist and their research groups are thanked for their hospitality and for allowing me to use their research facilities.

A truck load of thanks and appreciation to the Deutscher Akademischer Austausch Dienst (DAAD) i.e., German Academic Exchange Service for a scholarship that enabled this work to become a reality. I am grateful to the University of Nairobi for offering me study leave(s) that accelerated the completion of this work.

Last but not least, I bow in honour to my beloved wife Jedidah for granting me an 'academic leave' and committedly taking care of our children, Emmanuel and Ndinda during my absence.

LIST OF CONTENTS PAGE

CHAPTER 3 THEORETICAL BACKGROUND

LIST OF SYMBOLS

a	Area.
Ar	Argon.
B	Magnetic field flux density.
c	Speed of light.
Cu-K_α	Alpha radiation of K in copper.
d	Crystalline atomic spacing.
D_{ps}	Particle size.
D	Unexcited dye.
D*	Excited dye.
D_n	Diffusion constant in the p-region.
D_e	Electron diffusion coefficient.
D_{ox}	Density of empty states.
D_p	Diffusion constant of electrons in the n-region.
D_{red}	Density of occupied states.
E	electric field.
E_{atoms}	Ejected atoms.
e^-	Electrons.
e^- (cb)	Electrons in conduction band.
E_F	Fermi level.
E_g	Energy band gap.
$E_{red/ox}$	Potential of redox couple.
$E^o_{red/ox}$	Standard redox potential.
F	Faraday constant.
F_L	Lorenz force.
FF	Fill factor.
h	Planck's constant.
h^+	Holes.
I	Current.

I_{ions}	Incident ions.
I^-	Iodide ions.
I_3^-	Poly/tri-iodide ions.
I_D	Diode current (junction current).
I_L	Generated photocurrent.
I_m	Current at maximum output power.
I_i^*	Current data point obtained by fitting.
I_{il}	Incident light intensity.
I_o	The diode saturation current or dark current.
I_{ph}	Photocurrent.
i_{phd}	Photocurrent density.
I_{sc}	Short circuit current.
k	Boltzmann's constant.
L_D	Eectron diffusion length.
k_{pd}	Photon density.
m_e	Mass of the electron.
m_f	Mass of the film.
n-type	Material whose majority carriers are electrons.
n	number of electrons transferred in the redox reaction.
N	Number of experimental data points for fitting.
n_{ed}	Electron density.
n_{if}	Ideality factor.
n_{do}	Diffraction order.
n_p	Equilibrium density of electrons in the p-region.
n_o	Equilibrium electron concentration in dark.
O_2	Oxygen.
$\{ox\}$	Oxidized species of the redox molecule.
P	Power.
P_{opt}	Optical power.

$P_{porosity}$	Porosity.
P_{in}	Power due to incident radiation.
P_m	Maximum output power.
p_n	Equilibrium density of holes in the n-region.
p-type	Material whose majority carriers are holes.
q	Elementary charge of an electron.
Q_{SC}	Electrons accumulated in the TiO_2 under short circuit conditions.
R	Reflectance.
R_{series}	Series resistance.
R_{shunt}	Shunt resistance.
R_g	Gas constant.
r	Radius of circular path.
$\{red\}$	Reduced species of the redox molecule.
T	Absolute temperature.
T_d	Electron transit time.
T_m	Melting point of deposition
T_{n-p}	Lifetime of electrons in the p-region
T_n	Electron lifetime.
T_{n-n}	Lifetime of electrons in the n-region.
T_s	Substrate temperature.
V	Voltage.
V_f	Volume of the film.
V_i^*	Voltage data obtained by fitting.
V_{oc}	Open circuit voltage.
V_m	Voltage at maximum output power.
x	Dye position in TiO_2 where electrons are released.
$Y_{sputter}$	Sputter yield.
α	Angle between substrate normal and sputter beam direction.
$\alpha(\lambda)$	Absorption coefficient of the sensitised TiO_2 film.
β	Angle between film columns and substrate normal.

β_{FWHM}	Full-width-at-half-maximum (FWHM).
δ	Small constant number.
μc-Si	Microcrystalline silicon.
μm	Micro meter.
η_{ce}	Conversion efficiency.
η_e	Charge collection efficiency at the back contact.
η_{eic}	Electron injection efficiency.
$\eta_i(\lambda)$	Internal quantum efficiency/number of photons at each wavelength.
ω	Modulation frequency.
$\omega_{d\text{-}min}$	Minimum modulation frequency for IMPS.
$\omega_{n\text{-}min}$	Minimum modulation frequency for IMVS.
π	Pie.
τ_{imps}	IMPS time constant/electron transport time.
Φ_{inj}	Quantum yield of electron injection.
θ	Angle between sun's position at zenith and any other position.
θ_{diff}	Diffraction angle.
θ_e	Angle between electron direction and flux density.
λ	Wavelength.
v	Frequency.
v_e	Velocity.
$v_{d\text{-}min}$	Minimum frequency for IMPS.
$v_{n\text{-}min}$	Minimum frequency for IMVS.
ρ_d	Density of a non-porous film.
ρ_f	Film density.
$\sigma(I)$	Noise levels in the current.
$\sigma(V)$	Noise levels in the voltage.

LIST OF ABBREVIATIONS/ACRONYMS

ac	Alternating current.
AFM	Atomic force microscope.
AM	Air mass.
APCE	Absorbed photon to current conversion efficiency.
a-Si	Armophous silicon.
ASTM	American Society for Testing and Materials.
DC	Direct current.
DSSC	Dye sensitized solar cell.
DSSCs	Dye sensitized solar cells.
EE	Illumination from the electrolyte side.
FEG	Field emitting gun.
FTO	Fluorine tin oxide.
G	Global
HOMO	Highest occupied molecular orbital.
IMPS	Intensity modulated photocurrent spectroscopy.
IMVS	Intensity modulated photovoltage spectroscopy.
IPCE	Incident photon to current conversion efficiency.
LHE	Light harvesting efficiency.
LUMO	Lowest unoccupied molecular orbital.
NASA	National Aeronautics and Space Administration.
NIR	Near infrared.
PEC	Photoelectrochemical.
SE	Illumination from the back contact side/TiO_2 side.
SEM	Scanning electron microscope.
STM	Scanning transmission microscope.
UV	Ultra violet.
VIS	Visible.
XRD	X- ray diffraction.

CHEMICAL NAMES

CdTe	Cadmium Telleride.
CIGS	Copper Indium Gallium Selenide.
CIS	Copper Indium Selenide.
GaAs	Gallium Arsenide.
GaInP	Gallium Indium Phosphorous.
Ge	Germanium.
InP	Indium Phosphorous.
SnO_2:F	Fluorine doped tin oxide.

LIST OF FIGURES

LIST OF TABLES

ABSTRACT

Nanoporous titanium dioxide (TiO_2) thin films have been obliquely deposited by reactive direct current (DC) magnetron sputtering onto conducting glass substrates for dye sensitized solar cell fabrication. Normally sputtered compact underlayer of nanocrytalline TiO_2 films, on which a porous layer of TiO_2 was deposited by the doctor blading technique, were also prepared to study the effect of the underlayer on the performance of the solar cells fabricated from porous films with underlayers.

TiO_2 films deposited on heated substrates (250 ± 5 °C) were stochiometric, and predominantly anatase, whereas films deposited on unheated substrates had to be thereafter thermally annealed at ~ 450° C for ~ 4 hours to obtain stochiometric TiO_2. Irrespective of whether the TiO_2 films were deposited on heated substrates or ambient temperatures, it was observed that the current-voltage (I-V) and incident photon-to-current conversion efficiency (IPCE) characteristics of the fabricated solar cells depended on the deposition angle. Films deposited at deposition angles equal to or greater than 60° gave higher photoelectric conversion efficiencies. These films had enhanced porosity (which creates more space for dye absorption and also enhances light scattering) which would explain the higher photoelectric conversion efficiencies seen at the higher deposition angles. For all subsequent sputter-deposited films the deposition angle was maintained at 60°, unless otherwise specified.

When the films were used as photoelectrodes in dye sensitized solar cells and from the I-V measurements done both at 100 W/m^2 (one-tenth sun) and 1000 W/m^2 (one sun), it was noted that photoelectric conversion efficiency increases with film thickness. This is because the thicker films provide larger surface areas onto which the dye molecules anchor leading to higher light absorption and corresponding higher photocurrents and photoelectric conversion efficiencies. The highest efficiencies were ~ 3.3 % at 100 W/m^2 and 2.06 % at 1000 W/m^2.

Electron transport and recombination studies carried out on these solar cells by the use of a red laser light using intensity–modulated photocurrent and photovoltage spectroscopy (IMPS and IMVS) techniques respectively showed that both the electron transit time and lifetime increase on lowering the light intensity but increased with the thickness of the TiO_2 films. These charge transport characteristics were attributed to grain boundaries with associated trap and/or energy barriers.

I-V fit model software (IVFit Version.1.83) was used to extract cell parameters (series and shunt resistances, and ideality factor) from the I-V experimental data obtained for solar cells using the one-diode equivalent circuit model. Solar cells made from heated substrates had series and shunt resistances of ~ 10^{-9} Ω and ~ 10^{2} -10^{3} Ω respectively, high dark currents of ~ 10^{-3} -10^{-4} A and high ideality factors ~ 6 – 4337. An ideal solar cell should have zero series resistance, infinite shunt resistance and an ideality factor of one. These observed cell parameters could be attributed to poor cell design leading to shorting and back electron recombination. Solar cells made of thermally annealed films had series resistance in the ~ 20 - 36 Ω range, high shunt resistances of ~ $8x10^{6}$ - $12x10^{6}$ Ω, lower dark currents of ~ $0.4x10^{-6}$ – $1.3x10^{-6}$ A and ideality factors of ~ 2.1 – 3.3. These improved values are attributed to better cell design and the role played by thicker films of ~3 -10 μm compared to cells fabricated with thinner films ~1μm. Despite the improved cell characteristics of the latter set of cells, charge transport measurements still showed evidence of back electron recombination.

The use of compact TiO_2 as a blocking underlayer in dye sensitized solar cells to minimize back reaction recombination in the solar cells was attempted. The compact TiO_2 films were prepared by normal deposition by reactive DC magnetron sputtering, followed by depositing of a porous layer of TiO_2 by the doctor blading technique. Solar cells with blocking underlayers, had increased electron-time compared to those without, confirming that the compact film minimized back reaction recombination.

CHAPTER 1

INTRODUCTION

1.1 General introduction

To meet human energy needs, man has over the years depended mainly on conventional energy resources like fossil fuels, nuclear and hydroelectric power. The dwindling of conventional energy resources together with rising global population and the rapid technological advancement however, seem to challenge mankind to rethink his future energy needs. Currently, there is more concerted effort through research and development to supply man's future energy needs through renewable energy technologies: wind, photovoltaic and biomass. The sun's energy (from its radiation) is immense and can be used to reduce the dependence on conventional fuels. It is free, environmentally friendly and also inexhaustible because of the projected life span of the sun of about 10 billion years. Electricity from solar energy would be much welcome particularly in developing countries where majority of the population resides in scattered homesteads and grid connection is expensive, and at times uneconomical.

The sun's immense energy can be converted to electrical energy using solar cells. Solar cells provide high-quality electric lighting, which improve educational opportunities, provide access to information, provide power for irrigation in farms, micro-businesses, and help families be more productive after sunset. Solar energy also brings health benefits. It allows for the refrigeration of vaccines and other essentials thus playing a part in improving public health. For many rural residents in remote areas, a shift to solar electricity from fossils fuels like kerosene improves both indoor and outdoor air quality. Solar absorbers can also be used to provide thermal energy for water heating, crop drying and space heating.

1.2 Types of solar cells

There are two main types of solar cells: p-n junction (conventional) and photoelectrochemical. P-n junction solar cells are further classified into silicon (crystalline, polycrystalline and amorphous), group III-V (GaAs, InP etc.), thin film chalcogenide (CIGS, CdTe etc), organic, and multijunction devices (GaInP/GaAs/Ge, GaInP/GaAs, GaAs/CIS, a-Si/c-Si, etc) [Green *et al.*, 2007]. In p-n junction solar cells, p- and n-type materials are brought together and the system provides a current when light shines on it. On the other hand, dye sensitized solar cells (DSSCs) consist of a semiconducting thin film deposited on a conducting glass (the film coated conducting glass substrate is referred to as photoelectrode). This photoelectrode is sensitized by soaking in a dye for some hours. The counter electrode is either a thin sheet of platinum or platinised conducting glass or sometimes even carbon. An electrolyte is then sandwiched between these two electrodes. Most of today's commercial solar cells are p-n junction and are fabricated from materials that need to be of high purity. This high level of purity escalates the material processing cost thereby making these type of solar cells expensive and out of reach to many deserving people [Green, 1992].

1.3 Why dye sensitized solar cells?

One of the current research areas in the utilization of solar energy and which has the potential for providing considerable energy in future is DSSCs. DSSCs offer a number of technological advantages compared to p-n junction solar cells:

- They offer the ability to construct transparent solar modules thus permitting application of these solar modules in windows, roof lighting, auto mobile sunroofs, and displays, etc.
- The use of dye sensitizers that can be saturated at low light energy allows the solar cell to perform under a wider range of light conditions
- DSSCs are less sensitive to the angle of incidence of radiation and can use both refracted and reflected radiation [Kroon *et al.*, 2007]
- They are less sensitive to partial light shadowing

- DSSCs can be designed to operate at a wide range of temperatures up to 70° C. The performance of p-n junction silicon solar cells reduces drastically with temperature increase
- They do not require very stringent purity requirements
- The cell fabrication is simple and cheap
- The entire cell fabrication does not emit toxic gases [Lokhande and Dhumre, 1992; Heller and Miller, 1980].

Despite these advantages, before DSSCs can be fully commercialized, more research is needed to answer some key questions in relation to efficiency, stability, sealing and manufacturability [Kroon *et al.*, 2007]. For instance, the current highest efficiency for DSSCs is ~10.1-10.7 % compared to ~24.7 % for crystalline silicon and ~32.0 % for GaInP/GaAs/Ge solar cells [Green *et al.*, 2007].

The performance of DSSCs is affected by a number of factors namely:
The material used for the semiconducting film, the morphology of the semiconducting thin film, the type of sensitizing dye, the electrolyte used and the cell fabrication. So far, iodine / polyiodide electrolyte has been reported to be the best performing [Nazeeruddin *et al.*, 2001] while titanium dioxide (TiO_2) has attracted more attention than any other material as a semiconducting thin film although other materials like zinc oxide, tin oxide, iron oxide have also been attempted [Resnmo et al., 1997]. The best performing dye so far is the black dye but N719 and N3 ruthenium dye complexes have also shown good performance [Gratzel *et al.*, 1994, Nazeeruddin *et al.*, 2001]. Solar cell fabrication on the other hand has greatly improved to the extent of having sealed solar cells which are not only easier to handle but also offer flexibility during measurements.

The morphology of the semiconducting thin film that constitutes the photoelectrode in a dye sensitized solar cell setup also determines the cell's conversion efficiency.
In particular, the film thickness, particle size and porosity play an important role in determining the solar cell's conversion efficiency. The penetration of the dye into the

pores of the semiconducting thin film as well as the electron diffusion length are coupled to the thickness, particle size and porosity of the film thickness. By varying the deposition parameters, the morphology of the semiconducting thin film can be controlled in an attempt to obtain films of different thicknesses, porosity etc.

1.4 Statement of the problem

Despite the studies that have been carried out on TiO_2 as a semiconducting thin film deposited by a variety of deposition techniques, there has not been much attention given to the structural properties of obliquely sputtered TiO_2 thin films. Furthermore the use of obliquely sputtered TiO_2 thin films in photoelectrode fabrication for DSSC applications and the corresponding characterization of the solar cells e.g. current – voltage (I-V), incident photon-to-current conversion efficiency (IPCE) and charge transport studies has not received much attention or has not been reported altogether. When the obtained I-V data is fitted into the single diode equation model, important cell parameters like the ideality factor, series and shunt resistances can be extracted. These parameters are important pointers to the solar cell shortcomings providing vital information for further solar cell improvement. This study sets to provide information on the structural properties of obliquely sputtered TiO_2 thin films, the performance of DSSCs fabricated from the films as well as determine the shunt and series resistances of the solar cells.

1.5 Justification and significance of study

This study is expected to show that a columnar structure results when oblique angle sputtering is used as a deposition technique. It will also provide a better understanding of the morphology of titanium dioxide thin films prepared by oblique-angle physical vapour deposition. The film's morphology is important in determining the optical path length of the incident light. The morphology of the films also determines the amount of dye sensitizer and electrolyte on to the film and therefore the eventual light harvesting ability of the film as a photoelectrode and hence the solar cell's efficiency. Physical vapour deposition technique due to its ability to give better control of the microstructural features of the deposited film will be used to deposit the titanium

dioxide thin films. The study will give information on the performance of DSSCs fabricated from obliquely sputtered TiO_2 thin films as well as identify some of the problems from such solar cells.

1.6 Objectives

The research aims were:

- To optimize deposition parameters for the preparation of titanium dioxide thin films prepared by oblique-angle physical vapour deposition. These parameters are: base pressure in the coating chamber, substrate temperature, angle of deposition and film's thickness.
- To characterize titanium dioxide films as prepared. This characterization will include morphological and optical studies.
- To fabricate DSSCs using the titanium dioxide as photoelectrode.
- To determine current – voltage (I-V) characteristics and incident photon-to-current conversion efficiency (IPCE) of the solar cells fabricated.
- To study the charge transfer characteristics in the fabricated solar cells.
- To fit the I-V data obtained into some existing model to provide more understanding of the limitations of the solar cells.
- To incorporate a compact TiO_2 underlayer in the solar cell to minimize back electron transfer.

1.7 Scope of the work

In this work, titanium dioxide thin films were deposited obliquely with a view to obtaining films with increased porosity and aligned columnar microstructure proposed as ideal for charge transfer. These films were characterized physically, structurally and then incorporated in a DSSC setup. The fabricated DSSCs were characterized using a number of established techniques like I-V, IPCE, intensity modulated photocurrent spectroscopy (IMPS) and intensity modulated photovoltage spectroscopy (IMVS). Compact thin TiO_2 underlayers were deposited by sputtering and characterized. A porous layer of TiO_2 was deposited by doctor blading and the setup made into thin

film solar cells with and without dye and electrochemically and photoelectrochemically characterized. The findings of the current study are presented in this thesis.

1.8 Thesis organization

This thesis is divided into six chapters. The current chapter 1 introduces us to the work done and why. Chapter 2 reviews the research and development work in the area of DSSCs to date. The theoretical background of these types of solar cells is given in chapter 3. In chapter 4, the experimental techniques used in this work are given. Results and discussion are given in chapter 5. We conclude and give recommendations for further work in chapter 6. The literature cited in this work is given in the references.

CHAPTER 2

LITERATURE REVIEW

2.1 General introduction

P-n junction solar cells come in three forms depending on the crystal purity and whether crystals or thin film: monocrystalline, polycrystalline and amorphous (thin film) Monocrystalline solar cells are the purest, most expensive and have the highest conversion efficiency while amorphous have the least efficiency and are the cheapest [Green, 1992]. The process of obtaining high grade silicon for solar cells from the parent raw material (sand) is a highly energy intensive process and contributes to the high costs of these type of solar cells [Green, 1992]. This high electrical conversion cost can be reduced by enhancing the efficiency of the solar cells (so that there are fewer cells per module) and lowering the manufacturing cost. Thin film photoelectrochemical (PEC) solar cells may offer a cheaper alternative to conventional p-n junction solar cells.

The principle operations of PEC solar cells and conventional p-n junction solar cells are different. In p-n junction solar cells, solar radiation is converted into electrical energy when photons enter a material and free electrons from a stable position in the material and the electrons have enough energy to move through the material. This electron movement gives rise to a current flow when it passes through a load. PEC solar cells on the other hand consist of a semiconductor electrode and a counter electrode immersed in an electrolyte. When semiconductor electrode is illuminated, oxidation takes place at one electrode while reduction takes place at the other. No net change in the electrolyte therefore occurs. An electric current flows when the two electrodes are connected via a load.

PEC solar cells which are potentially easier and cheaper to fabricate than p-n junction, are therefore seen as possible future cheaper sources of electrical energy [Heller and Miller, 1980; Nazeeruddin *et al.*, 1993; Rensmo *et al.*, 1997]. PEC solar cells however, have some problems. For instance, most semiconducting thin films, for

example, InP, GaP GaAs, and Si which could be used in PEC solar cells and offer potential for high efficiencies have a narrow band of spectral response and this allows not only a small percentage of the solar radiation being absorbed by the cell giving low efficiencies, but they also get corroded in the electrolyte [Rensmo *et al.*, 1997]. Large band gap materials ($E_g > 2.5$ eV) are more stable in electrolytes in comparison to small band gap materials, but are transparent to solar radiation in the visible range. This means they absorb poorly the radiation needed (visible solar spectrum) in electrical-solar conversion systems. To increase the spectral range absorptance and sensitivity of the semiconducting thin films to solar radiation, the films are coated with certain photosensitive dyes [O'Regan and Gratzel, 1991; Gratzel, 1994]. For example, O'Regan and Gratzel [1991] noted that there is enhanced light harvesting when a trimeric ruthenium dye complex ($RuL_2(\mu$ -(CN) Ru(CN) $L'_2)_2$; L is 2,2' bipyridine-4,4' dicarboxylic acid and L' is 2,2' -bipyridine) was used as a sensitizer in a TiO_2 film. An increase of almost 100 % in light harvesting at an average efficiency of 7.5 % in simulated solar light and 12 % in diffuse light was obtained for a TiO_2 dye sensitized solar cell when a TiO_2 film was dye sensitized.

As a semiconducting thin film in PEC solar cells, TiO_2 has attracted much attention mainly due to its stability to photocorrosion in electrolyte. It is also cheap and non-toxic [Pulker *et al.*, 1976; Gofuku *et al.*, 1991]. The optical, electrical and structural properties of TiO_2 as a photosensitive semiconducting film, have been studied [Radecka *et al.*, 1993; Tang *et al.*, 1994; Kim, 1996]. Gofuku *et al* [1991] and Kim [1996] have reported that TiO_2 is a hard and chemically resistant material which is transparent (60 - 92 % transmittance) in the visible wavelength (350 - 800 nm) and near infra-red (NIR); and has a high refractive index useful in interference applications. Structurally, it exhibits three phases: anatase, rutile and brookite [Deloach *et al.*, 1999]. Studies have shown that the rutile structure is more stable at high temperatures (960 ^{o}C) than the more open structured anatase which has a stronger light absorption than rutile at a wavelength of 420 nm and more. TiO_2 has a large band gap ~ 3.0 eV for rutile phase and ~3.2 eV for anatase [Radecka *et al.*, 1993], which leads to its poor spectral response, i.e., low photon absorption. O'Regan and Gratzel

[1991] have observed that the absorption spectra of TiO_2 as-deposited have an absorption edge of 3.2 eV in the ultra-violet (300 - 450 nm) region.

The light trapping abilities of TiO_2 films also play a key role in the performance of DSSCs. One way of increasing the light trapping abilities of the TiO_2 thin films is to increase the roughness of the film surface so that a larger number of dye molecules can anchor on the film nano particles thereby increasing the absorption of the solar radiation. A rough surface also scatters more light that increases absorption lengths of photons and optical confinement in the film leading to higher efficiencies. An increase in surface roughness can be achieved through the film deposition techniques like physical vapour deposition (PVD) that allow control of the deposition parameters. Besides, it is important that the film should have the required nano-sized particles so as to maximize the dye absorption on the semiconducting thin film. Highly ordered thin films with columnar structure are expected to give a more exposed film surface area and enhanced electron diffusion which may translate into more efficient solar cells [Gratzel, 2000]. The need to control the film's morphology in these solar cells therefore cannot be over emphasized.

2.2 Deposition techniques

Several techniques have been used to deposit TiO_2 thin films for photoelectrodes for PEC applications. These include: sputtering [Gomez *et al.*, 1999[a,b], 2000[a,b]; Waita *et al.*, 2007], screen-printing followed by sintering [Lee *et al.*, 2001], and screen-printing followed by compressing [Boschloo *et al.*, 2002]. The most widely used technique for preparing the PEC photoelectrode is sol - gel/screen-printing mainly because (i) the capital outlay and running costs are relatively low, (ii) no need for highly qualified operators, (iii) circuit design geometry are simple and inexpensive to implement in production, and (iv) very thick films can be produced [Chopra and Das, 1983]. Unlike PVD, the sol-gel/screen-printing technique, does not allow for the control of deposition parameters (the paste of the required material is spread on the substrate).

Reactive sputtering of TiO_2 is a widely studied research area [Weinberger and Garber, 1995; Gomez *et al.*, 1999[a,b]; Vancoppenolle *et al.*, 1999; Szczyrowski *et al.*, 1999; Dimitrov *et al.*, 2000; Gomez *et al.*, 2000[a,b]]. Meng *et al.* [1993] used sputtered TiO_2 films to investigate the effect of substrate temperature on the film properties. According to his results, temperatures below 450 °C provided films that were randomly oriented but above 450 °C, the films assume a preferred orientation. The optical properties were found to be strongly dependent on the substrate temperature. TiO_2 thin films deposited at normal incident by reactive sputtering have been found to exhibit columnar structure as a result of self-shadowing effect and limited mobility of adatoms [Gomez *et al.*, 1999[a,b]; Gomez *et al.*, 2000[a,b]]. This columnar structure ensures more surface area of the film is exposed [Tait *et al.*, 1993; Hara *et al.*, 1995] and this is particularly important if the film is being deposited for DSSC applications where the exposed film's surface area contributes to the cell's efficiency. For example, using reactive sputtering Gomez *et al* [2000[a]] deposited TiO_2 films for DSSCs and obtained a solar cell of about 4 % efficiency without pyridine treatment. The efficiency rose to about 7 % when pyridine was used to treat the solar cells [Gomez *et al*, 2000[b]]. Studies by Gomez *et al* [2000[a,b]] also established that sputter-deposited TiO_2 films give a higher photocurrent when applied as photoelectrodes in DSSCs compared to sol-gel prepared films. This was attributed to the open structure (larger surface area) obtained during sputtering. The study by Gomez *et al.* [1999[a,b], 2000[a,b]], Tait *et al.* [1993] and Hara *et al.* [1995] focused on the normal deposition of the films by sputtering.

2.2.1 Oblique angle deposition

The oblique angle deposition technique is similar to the above (reactive sputtering) but the manner in which the substrate is oriented is different. That is, in oblique deposition the line of sputter material makes a non zero angle to the substrate normal. In this method, a combination of self-shadowing and the limited adatom mobility creates a columnar structure. It has been estimated that a column of diameter 250 nm in an obliquely deposited film would give 100 times more surface area exposure than that of a normally deposited film if both were 10 μm [Weinberger and Garber, 1995].

Obliquely deposited films have high porosities suitable for applications where open structures are advantageous like in solar cells. Messier *et al* [2000] have established that films of densities as low as 10-30 % of the bulk material can be fabricated. Further work by Suzuki and Taga [2001] has established that the surface area of the films is enhanced by oblique deposition and becomes maximum at a deposition angle of 70° and that morphology related quantities like porosity and surface area of the films are functions of deposition angle [Suzuki and Taga, 2001; Paritosh and Srolovitz, 2002].

Abelmann and Lodder [1997] have done some review of literature on thin films deposited obliquely by evaporation. By considering several theoretical models, they established that the shadowing phenomenon during film growth is responsible for diffusion and creates the difference between random and directional surface diffusion. Robbie and Brett [1997] by using a combination of oblique evaporation and substrate rotation created three dimensional sculptured thin films with shapes ranging from zig-zag to helical. These types of films have potential applications in optical, biological and chemical devices and materials. Two years later, Malac *et al* [1999] used the same technique (oblique deposition-sometimes called Glancing Angle Deposition (GLAD) to produce two dimensional lattices of submicrometer pillars and helices. These types of films were found to have potential applications in photonic crystals and magnetic-storage media [Malac *et al.*, 1999; Dick *et al.*, 2003]. More recently, Kiema *et al.* [2005] fabricated DSSCs from obliquely evaporated TiO_2 thin films obtaining higher shorter current densities for large deposition angles (60-75°) and an efficiency of 4.1% for the best solar cell.

2.3 Charge transport

The morphology of the thin film semiconducting material used in DSSCs determines to a large extent how fast the electrons can travel to the back contact and hence external circuit or in other words, how efficient the solar cell can be. Charge transport studies in DSSCs are therefore important. However, charge transport in porous semi conducting materials of DSSCs is one area that has not been fully studied despite the

wealth of information that can be derived from such a study. The study of charge and electron transport in DSSCs is important since it is through a thorough understanding of the electron conduction process that adjustments in the cell fabrication properties can be made to achieve high efficient solar cells. Lately however, research interest in this area has increased [Asbury *et al.*, 1999; Solbrand *et al.*, 1999; Timoshenko *et al.*, 2000; Zhang 2000; Nelson *et al.*, 2001; Usami and Ozaki, 2001; Nelson *et al.*, 2002]. The charge transport mechanism is very important in nano-porous materials, as the movement of charge in them is quite different from the bulk material bulk [Nelson *et al.*, 2001]. Studies conducted on the effect of surface states that are as a result of surface and/or internal defects indicate that they act as traps for the photo-generated electron charge carriers [Zhang, 2000]. This trapping combined with recombination of the electron charge carriers obviously have adverse effects on the photo-generated current. A low charge separation efficiency of ~1% for every incident photon was obtained by Zhang, an indication that interfacial charge transfer occurs mainly in excited states produced in the first monolayer of the sensitizer. This study by Zhang was however only for ~80 nm thick anatase TiO_2 film deposited by electron beam evaporation.

The diffusion model is one of the simplest models to explain charge transport. Sodergren *et al.* [1994] and Solbrand *et al.* [1997] used this model for porous TiO_2 and obtained a diffusion coefficient of $1x10^{-2}$ cm^2/s for electrons that diffuse through a single colloidal particle and 10^{-7} cm^2/s for porous TiO_2 encompassing a solid electrolyte. A liquid electrolyte would give a lower diffusion coefficient than that for the single colloidal particle, but higher than that for a solid electrolyte.

Thus, the nature of the dye molecule and the surface properties of nano particles determine the rate of electron injection and back electron transfer (recombination). Obviously therefore, the size and shape of these nano particles play a critical role. The electron mobility of sol-gel fabricated TiO_2, is $6x10^{-4}$ cm^2 V^{-1} s^{-1} according to Sodergren *et al.* [1994]. Further observations showed that the complex network of the porous semiconductors determined the electronic transport indicating that the smaller

the nano structures, the slower the diffusion. Sodergren *et al.* [1994] gave a purely theoretical treatment of the charge movement and for a single colloidal particle and sol-gel fabricated TiO_2.

Both the charge transport properties and mechanism of electron movement in DSSCs are not yet well understood [Konenkamp, 2000; Bisquert *et al.*, 2004]. Electron transport properties have been studied using techniques such as intensity modulated photocurrent spectroscopy (IMPS) [de Jong and Vanmaekelberg, 1997; Peter and Wijayantha, 2000; van der Lagemaat and Frank; 2000], impedance spectroscopy [Fabregat-Santiago, *et al.*, 2002; 2003] and photocurrent transient [Solbrand, *et al.*, 1997]. Peter and Wijayantha [2000] have used IMPS to show that the electron diffusion coefficient increases while the electron lifetime decreased with illumination intensity in TiO_2 films prepared by doctor blading. Van der Lagemaat and Frank [2000] have attempted describing electron transport in nanocrystalline TiO_2 DSSCs using analytical expressions. They found that the electron–transport rate is related to the electron population by a power law due to the exponential distribution of surface states.

The movement of photoexcited electrons through the TiO_2 film to the back contact for collection is by diffusion [Peter and Wijayantha, 1999]. Charge transport studies have shown that electron transport is strongly light intensity dependent [de Jongh and Vanmaekelbergh, 1996; Dloczik *et al.*, 1997; Fisher *et al.*, 2000]. This electron diffusion constitutes a time delay between photoelectron injection and collection by the back contact which appears as a phase lag in the photocurrent response to intensity modulated light [Dloczik, *et al.*, 1997].

As observed in the preceding literature reviewed, most of the studies on charge transport in DSSCs have either been theoretical or on doctor-blade prepared TiO_2 films. There is therefore need to undertake some charge transport studies on DSSCs fabricated from sputtered TiO_2 thin films.

2.4 Effect of film porosity

Several studies have focused on the effect of the morphology of the nanocrystalline TiO_2 film on the electron transport. For instance, the porosity was found to play an important role, as it affects both the light absorption coefficient and electron diffusion coefficient [Liang *et. al*, 2006]. Electron transit time was found to increase with porosity when the solar cell is illuminated from the electrolyte side. Also the size of the TiO_2 nano particles has been investigated. Increasing the size of the nano particles was found to lead to faster electron transport and slower recombination [Nakade *et. al*., 2003]. The porosity of the thin film is therefore of strategic importance in DSSCs and hence the need to explore ways of enhancing the film porosity.

It can be said from the foregoing that although some studies on oblique deposition have been done, there has not been a detailed study and analysis of films deposited by oblique sputtering. Details of the study and characterization of DSSCs fabricated from obliquely sputtered TiO_2 thin films are also not available. In the current study, we show that columnar TiO_2 thin films are formed by oblique sputtering at various deposition angles and these films are suitable when used as photoelectrodes in DSSCs. Furthermore, we will report on the electron transport and recombination in the deposited TiO_2 thin films. We also show that electron back transfer to the electrolyte can be minimized by incorporating a compact underlayer of TiO_2 beneath a porous nanocrystalline film in the solar cell.

CHAPTER 3

THEORETICAL BACKGROUND

3.1. Introduction

Solar energy is non-exhaustible (sun's life span is estimated at 10 billion years), non-polluting and free [Deshmukh and Deshmukh, 2008]. This makes the sun an attractive source of energy; especially for solar cell applications that convert solar radiation directly to electrical energy. Solar radiation is also an invaluable source of heat and can be used for cooking and heating purposes. In 1767, Horace de Saussure built the first world's solar collector.

Around 1807, C Gunter invented the solar boiler using mirrors, sparking the current research into the utilization of solar energy [http://solarcooking.org/Saussure.htm, 2007]. The research progress in utilization of solar energy for heating purposes however rather slow owed to the availability of cheap fossil fuels like coal. It was not until the 1800's that there was some renewed momentum into solar energy research mostly inspired by the availability of funds donated by Godfrey Cabot [Sayigh, 1977]. On the other hand, there has been a lot of progress in the use of solar cells for solar energy-electrical conversion. To date, p-n junction solar cells are not only a common feature in homes and industries, but also in low power consumer devices like calculators, watches, mobile phone chargers and even in terrestrial applications. The major challenges that p-n junction solar cells and other emerging technologies must overcome are: performance, reliability, durability and efficiency. Besides, the fabrication costs of the solar cells must be low enough for them to be affordable to the majority of the people. The fabrication costs of p-n junction solar cells are quite high and this turns out to be a great drawback for these types of solar cells.

During the last two decades, solar cells fabricated from dye sensitized titanium dioxide thin films were reported. In the early 90s, dye sensitised solar cells with an efficiency of ~12 % in diffuse light were reported [O'Regan and Gratzel, 1991]. The motivation behind these types of solar cells is their easy fabrication and low assembly costs and better photo response under diffuse light compared to p-n junction solar cells.

3.2 Solar radiation

From time immemorial, man has known the sun to be a very important resource for life on earth. The fundamental and critical role the sun plays in man's development can be seen by the way great early agrarian civilizations worshiped the sun [Sayigh, 1977]. Today we do not worship the sun but do recognize and appreciate the role it plays in today's technology as a source of energy.

All countries of the world receive some solar energy even though the amount might vary from location to location. For example, considering all natural deserts of the world, an estimated area of $20x10^6$ km^2 of some deserts (the Arabic peninsula and Sahara) receives an average solar insolation of 583.30 W/m^2/day while another area of $30x10^6$ km^2 (in the northern countries and lower south America) gets 291.65 W/m^2/day [Sayigh, 1977]. Thus in total, the amount of solar insolation received by the $50x10^6$ km^2 of desert land for 8 hrs a day, ignoring seas and green land, is about 163.2 $x10^{12}$ kWh/day or 60 $x10^{12}$ kWh/year. Assuming we have solar panels with an efficiency of 1 %, this would translate into $60x10^{10}$ kWh/year [Sayigh, 1977]. Furthermore, only ten minutes of solar irradiation is enough to provide us with the world's annual needs [Nazeeruddin, 2006].

This immense energy from solar radiation is produced by fusion reactions like the combination of hydrogen with helium, which take place at the suns interior [Duffie and Beckman, 1980]. Once produced this energy is propagated to the earth's atmosphere by radiation. The energy from the sun per unit time received on a unit area perpendicular to the direction of propagation of radiation at the earth's mean distance from the sun outside the atmosphere is called the solar constant. This constant is not,

however, truly constant as it may fluctuate slightly over time. The National Aeronautics and Space Administration (NASA) and the American Society for Testing and Materials (ASTM) standard value for the solar constant is 1353 W/m^2 [Sayigh, 1991].

As the solar radiation is radiated to the earth's surface some of it is lost through absorption by ozone, carbon dioxide and monoxide and even water particles as the rays enter the earth's atmosphere. This absorption depends on the thickness of the atmosphere (air mass) through which the ray is travelling. An air mass (AM) is the path length traversed by direct solar radiation as a ratio of the path traversed to a point at sea level when the sun is directly overhead (figure 3.1).

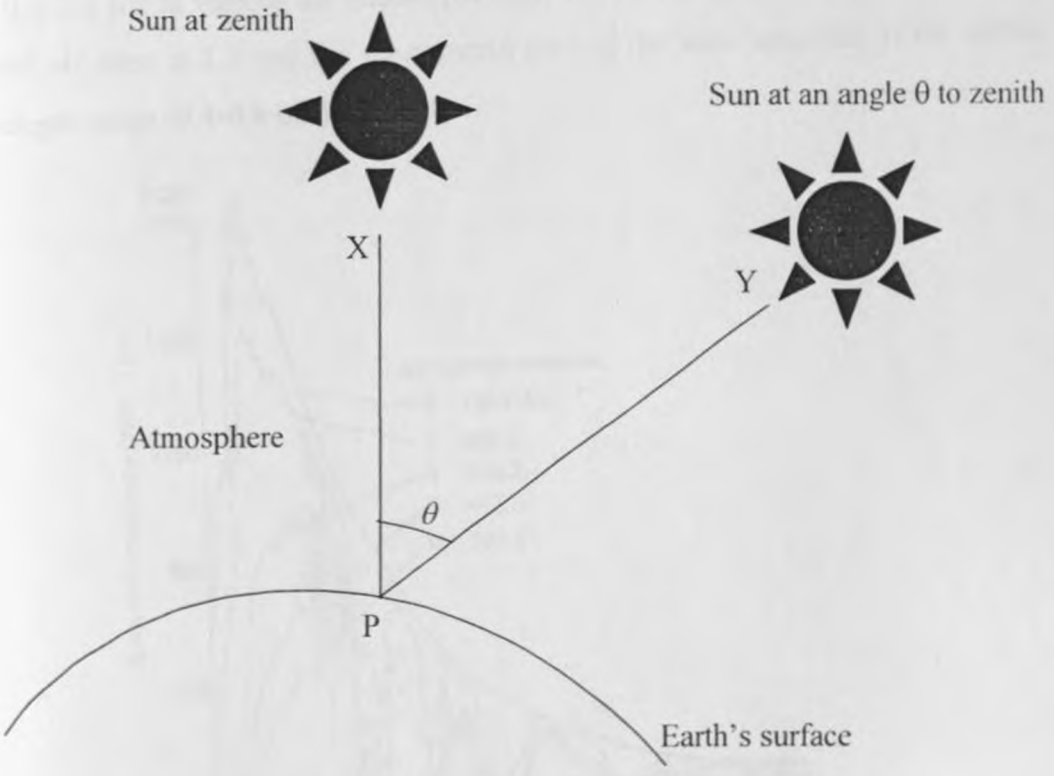

Fig. 3.1 Diagram defining air mass (AM).

Mathematically,

$$AM = 1/\cos(\theta) = PY/PX \qquad (3.1)$$

where θ is angle XPY.

Equation (3.1) is true for θ from 0^{o} to 70^{o} degrees, otherwise the earth's curvature should be taken into account. Therefore the air mass at sea level with the sun at zenith is air mass 1 (AM 1) and above the earth's atmosphere it is AM 0. It is important to note that air mass depends on the time of the day and year, and altitude and latitude of a place. Figure 3.2 below shows the extraterrestrial solar spectrum in the wavelength range 0.3-2.6 μm at various air masses [Sayigh, 1991]. For solar cell applications, the standard air mass is 1.5 and the most useful part of the solar spectrum is the visible wavelength range (0.4-0.8 μm).

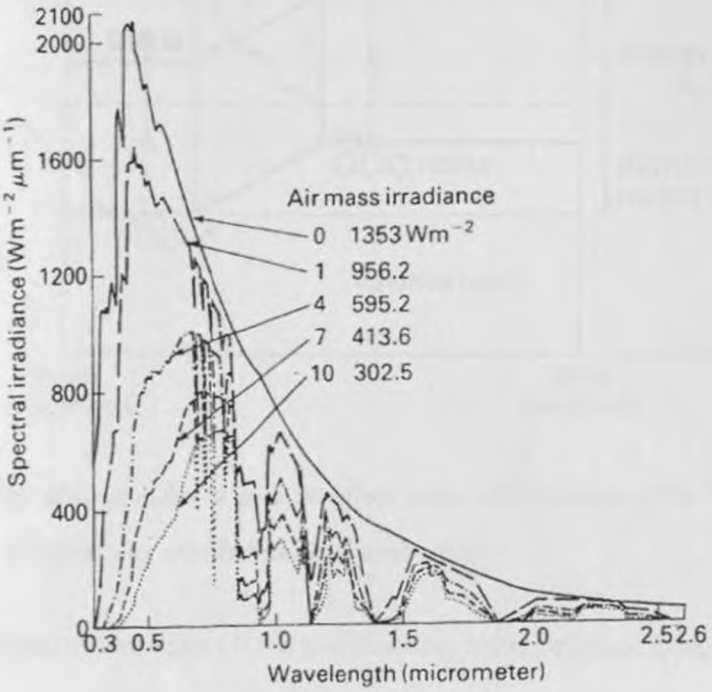

Fig. 3.2. Solar irradiance at different air masses [Sayigh, 1991].

3.3.1.1 Current-voltage (I-V) characterization

A p-n junction solar cell consists of two semiconducting materials; one doped to achieve holes (h^+) as the majority charge carriers hence called p-type and the other doped to make electrons (e^-) the majority charge carriers (n-type). When the p- and n-type parts are brought together, the junction creates a non-uniform doping profile thus creating an energy barrier. The junction separates electrons from holes when the semiconductor absorbs light. Figure 3.3 shows the energy diagram for a p-n junction solar cell.

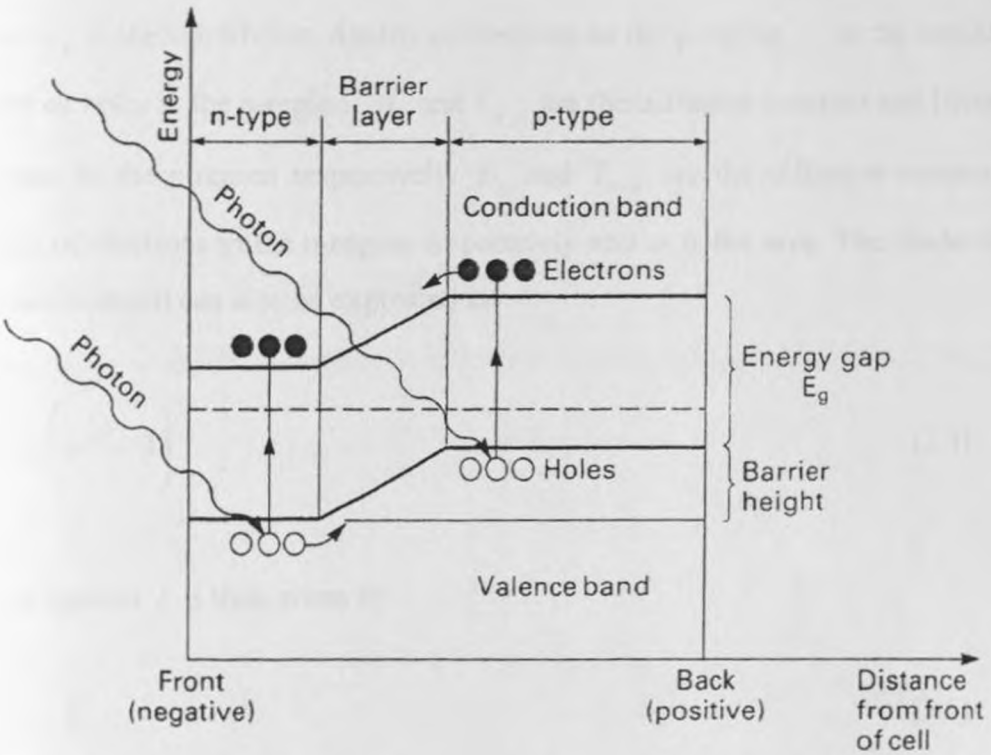

Fig. 3.3. Energy diagram for a p-n junction solar cell showing the barrier layer and the movement of electrons and holes on illumination.

The current (I) and the voltage (V) in p-n junction solar cells are related by [Sze, 1969; Green, 1992]:

$$I = I_O\left(e^{\frac{qV}{kT}} - 1\right) - I_L \qquad (3.2)$$

where I_o is the diode saturation current or dark current, q is elementary charge, k is Boltzmann's constant, T is the absolute temperature, and I_L the generated current after photon absorption. The saturation current can be expressed as

$$I_O = \left\{ qp_n \left(\frac{D_p}{T_{n-n}} \right)^{\frac{1}{2}} + qn_p \left(\frac{D_n}{T_{n-p}} \right)^{\frac{1}{2}} \right\} \times a \tag{3.3}$$

Where n_p is the equilibrium density of electrons in the p-region, p_n is the equilibrium density of holes in the n-region, D_n and T_{n-p} are the diffusion constant and lifetime of electrons in the p-region respectively, D_p and T_{n-n} are the diffusion constant and lifetime of electrons in the n-region respectively and a is the area. The diode current (junction current) can also be expressed as

$$I_D = I_O \left(e^{\frac{qV}{kT}} - 1 \right) \tag{3.4}$$

The net current I is then given by

$$I = I_D - I_L \tag{3.5}$$

The above equations describe an ideal solar cell whose simplified equivalent circuit is shown in figure 3.4.

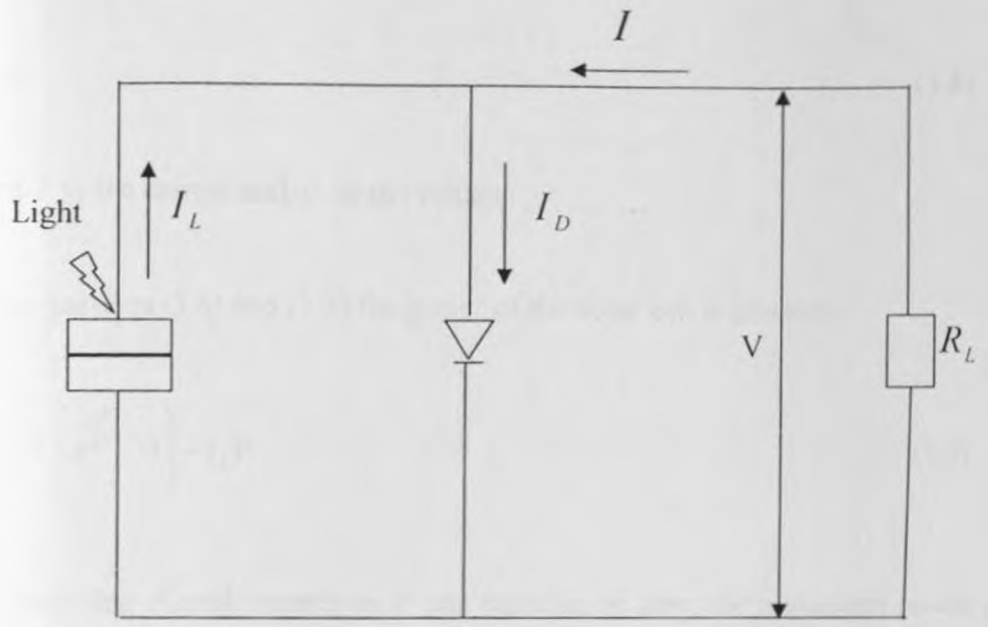

Fig. 3.4. Equivalent circuit of an ideal solar cell.

Under short –circuit conditions ($I = I_{SC}$), no voltage exists at the cell terminals and thus $V = 0$. Equation (3.2) above then becomes

$$I_{sc} = -I_L \tag{3.6}$$

Under open - circuit condition ($V = V_{OC}$), no current flows in the cell and $I = 0$ giving the open circuit voltage (V_{OC}) from equation (3.2) as

$$V_{OC} = \frac{kT}{q} \ln\left(\frac{I_L}{I_O} + 1\right) \tag{3.7}$$

The power P, of a system is given by

$$P = IV \tag{3.8}$$

where I is the current and V is the voltage.

Using equations (3.8) and (3.2) the power of the solar cell is given by

$$P = I_O V\left(e^{\frac{qV}{kT}} - 1\right) - I_L V \tag{3.9}$$

Differentiating P with respect to V and equating to zero, the maximum power points (V_m, I_m) can be obtained. This gives

$$V_m = \frac{kT}{q} In\left\{\left(\frac{I_L}{I_O} + 1\right) \Big/ \left(\frac{qV_m}{kT} + 1\right)\right\} \tag{3.10}$$

$$I_m = -I_O e^{\frac{qV_m}{kT}} \frac{qV_m}{kT} \tag{3.11}$$

The current-voltage (I-V) characteristics of an ideal solar cell under illumination would be the shaded area as shown in figure 3.5.

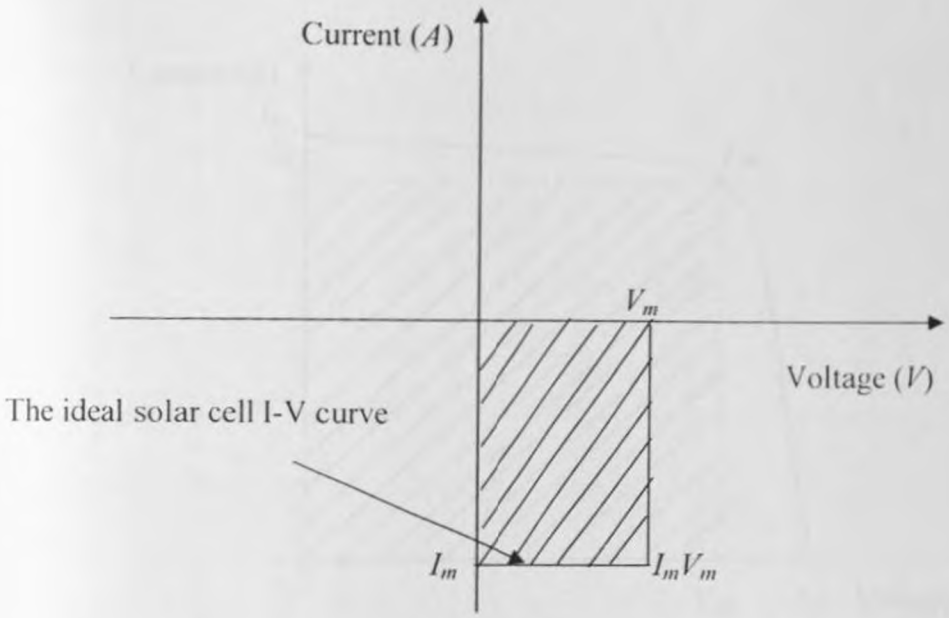

Fig. 3.5. Ideal solar cell current-voltage characteristics under illumination.

The efficiency of such a cell as in figure 3.5 would be 100 %. However, in reality the efficiencies are much lower. Several factors contribute to these low efficiencies: defects during fabrication, recombination of electrons and holes, and series and shunt resistances. Due to these factors, not only the equivalent circuit needs modification, but also the I-V curve. Figure 3.6 shows the equivalent circuit of a practical solar cell while figure 3.7 shows the inverted I-V curve of the cell.

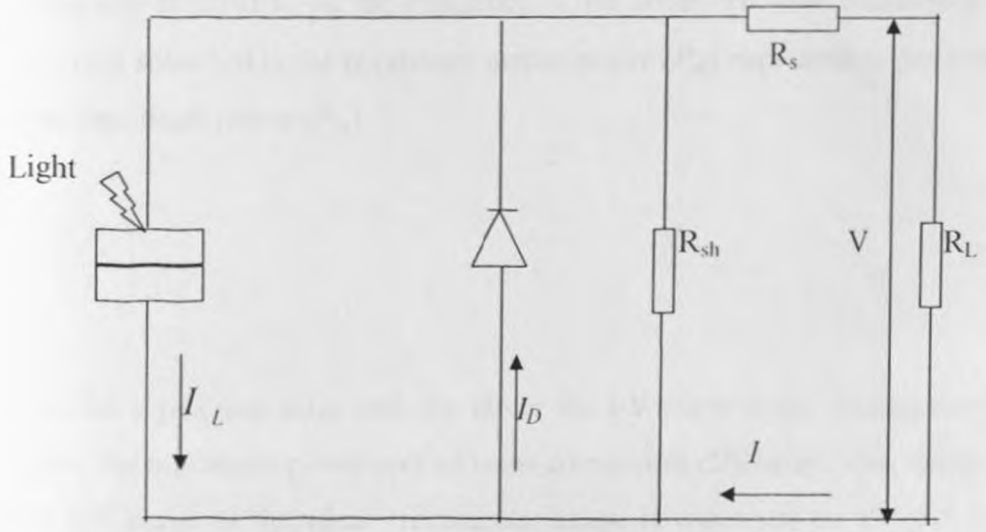

Fig. 3.6. Equivalent circuit of a practical solar cell.

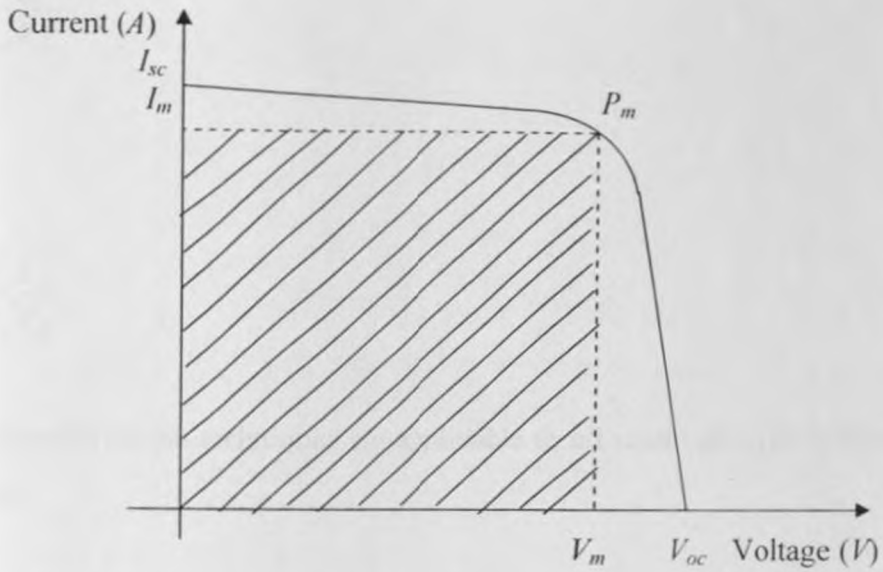

Fig. 3.7. Current-voltage characteristics of a practical solar cell under illumination.

The maximum power (P_m) is normally represented by the area of the largest rectangle that can be fitted under the curve and is defined by

$$P_m = I_m V_m \tag{3.12}$$

The ability of a solar cell to convert incident radiation into electrical power is commonly referred to as the efficiency of the solar cell. The conversion efficiency (η_{ce}) of a solar cell is the maximum output power (P_m) expressed as percentage of the input (incident) power (P_{in}).

$$\eta = \left(\frac{P_m}{P_{in}} \right) \tag{3.13}$$

Thus for a practical solar cell, the closer the I-V curve to the rectangular shape, the higher the maximum power and so is the conversion efficiency. The fitting of a solar cell I-V curve to the ideal rectangular shape is measured by the fill factor (FF) defined as:

$$FF = \frac{P_m}{I_{sc} V_{oc}} \tag{3.14a}$$

Or

$$FF = \frac{I_m V_m}{I_{sc} V_{oc}} \tag{3.14b}$$

These characterization techniques are applicable to all solar cells, conventional or dye sensitized.

3.3.1.2 Incident photon-to-current conversion efficiency (IPCE) characterization

The incident photon - to - current conversion efficiency (IPCE) is defined as the ratio of photocurrent to the number of photons incident on the system [Hagfeldt and Gratzel, 1995]. For a p-n junction solar cell the IPCE is called internal quantum efficiency and is given by:

$$\eta_i(\lambda) = \frac{(\frac{i_{phd}}{q})}{k_{pd}(\lambda)} \tag{3.15}$$

where i_{phd} is the photocurrent density (A/cm^2), q is the elementary charge of an electron, and k_{pd} is the photon density for each wavelength (λ). The photon density k_{pd} is related to optical power P by

$$P = h \times f \times k_{pd}(\lambda) \tag{3.16}$$

h is Planck's constant and f is the frequency of the incident radiation.
Noting that the speed of light c, wavelength, and frequency f, are related by $c = f\lambda$ equation (3.15) becomes

$$\eta_r(\lambda) = \frac{(\frac{i_{phd}}{q})}{(\frac{P\lambda}{hc})} \qquad (3.17)$$

For dye-sensitized solar cells (DSSCs) the IPCE is called external quantum efficiency and in most IPCE measurements for DSSCs the reflectance and absorption of the substrate are usually ignored. The IPCE for DSSCs is given by [Yang *et al*, 2006]

$$IPCE \equiv \frac{1240 i_{phd}}{q \times \lambda \times P} \qquad (3.18)$$

I_{phd} = photocurrent density ($\mu A/cm^2$), q = electronic charge, P = power ($\mu W/cm^2$), λ = wavelength (nm). The product hc is in eV nm.

3.3.2 Dye sensitized solar cells (DSSCs)

3.3.2.1 Principle of operation of the dye sensitized solar cell

Unlike in the conventional solid-state solar cell where the light absorber also plays the role of charge separation, the dye-sensitized solar cell separates the two functions. A transition metal complex dye monolayer on the semiconductor surface absorbs the photons (similar to chlorophyll in plants) and transfers the charge to the semiconductor back contact (like the lipid bilayer of plant cellular structure). These type of solar cells are therefore considered as mimicking photosynthesis and thus the name artificial photosynthesis given to them.

A DSSC is composed of four main parts: the semiconducting thin film (in this case titanium dioxide), the dye, the electrolyte (iodine/iodide) and the counter electrode (see figure 3.8).

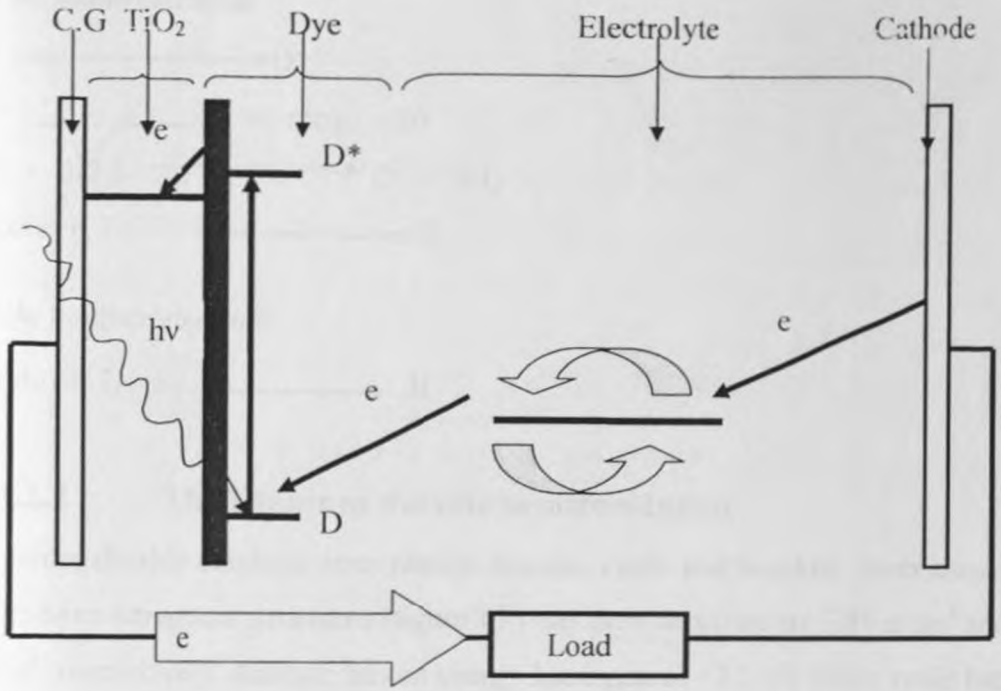

Fig. 3.8. Diagram showing the principle of operation of a DSSC. C.G stands for conducting glass.

On illuminating the photoanode, incident photons pass through to the sensitising dye D through the transparent conducting oxide (TCO) or back contact - either indium tin oxide (ITO) or tin oxide (SnO_2) and the semiconductor film (TiO_2). The dye is excited (D*) due to absorption of the photons and consequently releases electrons to the conduction band of the TiO_2. The injected electrons are collected at the back contact through the TiO_2 film by diffusion and on to the counter electrode through the external circuit. At the counter electrode, the electrons are released to the electrolyte which in turn replaces the dye electrons by injecting electrons into it. The entire process can be summarised using the equations below:

At the photo electrode

$D + h\nu \longrightarrow D^*$

$D^* \longrightarrow e^-(cb) + D^*$

$D^* + 3/2\ I^- \longrightarrow D + \frac{1}{2} I_3^-$

$e^-(cb) + I_3^- \longrightarrow 3I^-$

At the counter electrode

$e^-(cb) + I_3^- \longrightarrow 3I^-$

3.3.2.2 The titanium dioxide semiconductor

Titanium dioxide exists in three phases: anatase, rutile and brookite. Both anatase and rutile have tetragonal structures (figure 3.9) and their densities are 3.89 g/cm^3 and 4.26 g/cm^3 respectively. Anatase has an energy band gap of ~3.2 eV while rutile has ~3.0 eV [Radecka *et al.*, 1993]. Due to these high-energy band gaps, they are transparent to radiations both in the visible and infrared ranges. Rutile is more thermodynamically stable than anatase.

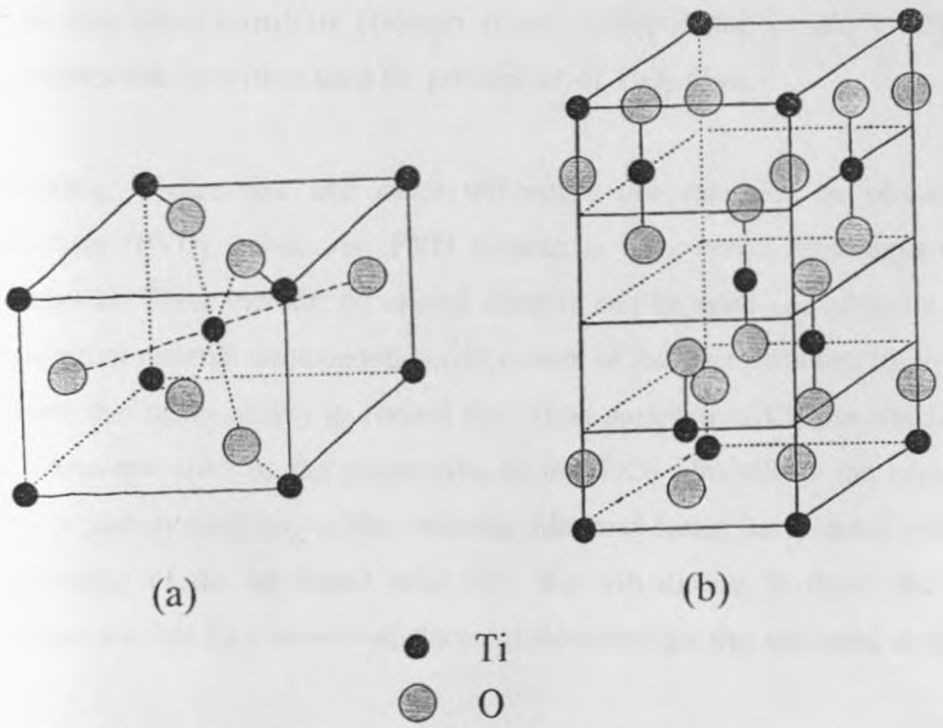

Fig. 3.9. Diagrams showing the structure of: a) rutile b) anatase titanium dioxide [Fahmi et al., 1993]

Titanium dioxide has some properties that make it of interest for industrial applications. Its high refractive index makes it favourable for use in paints while its non-toxic nature is a good property for use in cosmetics and health products. Its hard and chemically resistant nature makes it suitable for use as resistant coatings. Other applications include use in wave sensors and dielectric materials [Ferroni *et al.*, 1997], photocatalytic destruction of organic pollutants in water [Mills and Hunte, 1997], and electricity generation in the dye sensitised solar cells due to its high band gap that renders it photocorrosion resistant [O' Regan and Gratzel 1991; Kay and Gratzel, 1996; Bach *et al.*, 1998; Hagfeldt and Gratzel, 2000]. The main disadvantage with titanium dioxide in its application in DSSCs is its transparency to visible radiation. The dye on the film helps in absorption of the visible radiation.

3.3.2.3 Thin film deposition techniques

There are many techniques for deposition of TiO_2 thin films: hydrolysis [Nazeerudin *et al.*, 1993], sol-gel [O'Regan and Gratzel, 1991; Gratzel,1994] and sputtering [Gomez *et al.*, 1999[a,b]]. Thermal electron beam reactive evaporation [Pulker *et al.*, 1976] and spray pyrolysis [Golego *et al.*, 1999; Zhang *et al.*, 1992] are other techniques that have been used for preparation of TiO_2 films.

Sputtering, evaporation and other techniques are classified as physical vapour deposition (PVD) techniques. PVD techniques have some advantages over other techniques. These include: (i) several samples can be made coated at the same time (ii) minimal material contamination (iii) control of the microstructure (morphology) is possible due to the ability to control deposition parameters [Chopra and Das, 1983]. The technique used in the preparation of the TiO_2 film affects the crystal nature, porosity and morphology of the resulting film and hence has a direct effect on the performance of the fabricated solar cell. We will discuss in detail the sputtering technique for thin film deposition since it is the technique that was used in this work.

3.3.2.3.1 Basic sputtering process

The first cathodic sputtering was observed in a direct current (DC) gas discharge tube by Grove in the year 1852 [Chapman, 1980]. Sputtering destroyed the cathode and therefore was regarded as undesirable at the time. Today, sputtering is one of the important techniques used in the industries e.g., the microelectronics industry. Sputtering is favoured over many other deposition techniques due to its versatility, flexibility, simplicity of the physical process and the easy customisation. There are two main categories of sputtering: direct current (DC) sputtering and radio frequency (RF) sputtering. The former is suitable for conductive targets while the later is normally used for any target whether conducting or not. Sputtering techniques have been criticised for poor utilization of the target material. On the contrary, sputtering allows better control of deposition parameters and therefore offers better morphological control of the resulting films. In a sputtering process, the material to be sputtered (target) which is normally of disc type is used as a cathode and is connected to a power supply. Material from the target is then ejected through collisions by energetic particles like ions, neutrons, electrons or photons when they transfer their momentum to target atoms [Chapman, 1980]. The rate of deposition is described in terms of sputter yield, which is the average number of atoms or molecules ejected from a target surface per incident ion:

$$Y_{sputter} = \frac{E_{atoms}}{I_{ions}} \tag{3.19}$$

where $Y_{sputter}$ is the sputter yield, E_{atoms} the ejected atoms and I_{ions} the incident ions. The sputter yield depends on the energy of incident particles, surface structure of the target (crystal), angle of incident of sputter material and nature of target material [Wasa and Hayakawa, 1992]. Sputtering can be viewed as an atomic billiards ball game as shown in figure 3.10. When the cue ball (the incident ion in sputtering) in the billiards game hits the target balls (target atoms in sputtering) some complicated scattering process takes place and the target balls (ejected atoms or sputtered atoms) move in all manner of directions.

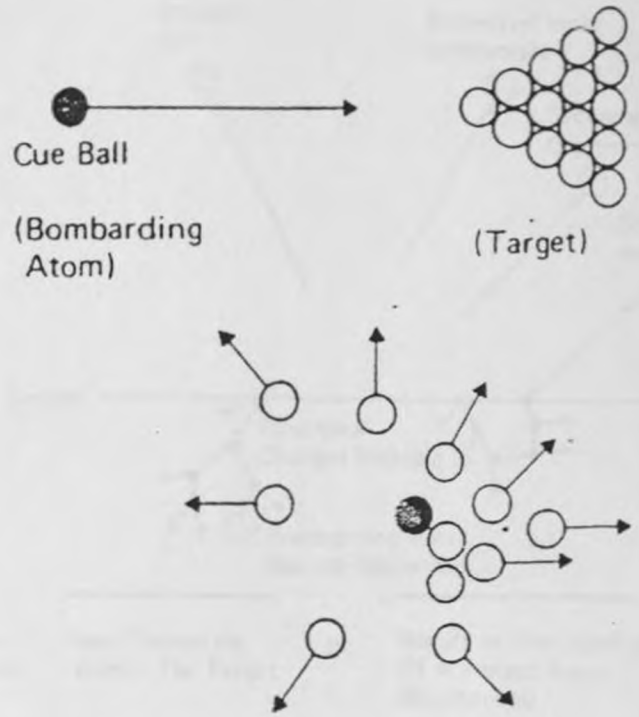

Fig. 3.10. The billiards ball model of sputtering [Chapman, 1980]

3.3.2.3.2 Interaction of ions with the target surface

When energetic ions hit the target, about five processes are likely to take place:

1. The ion is likely to be neutralized as ion scattering takes place.
2. Ejection of secondary ions takes place.
3. The ion may be permanently buried in the target-ion implantation.
4. Radiation damage to the target with structural rearrangements varying from simple vacancies and interstitials to gross lattice defects.
5. The ion impact sets up a series of collisions between target atoms leading to ejection of atoms-sputtering process [Chapman, 1980].

The five basic processes are summarised in figure 3.11.

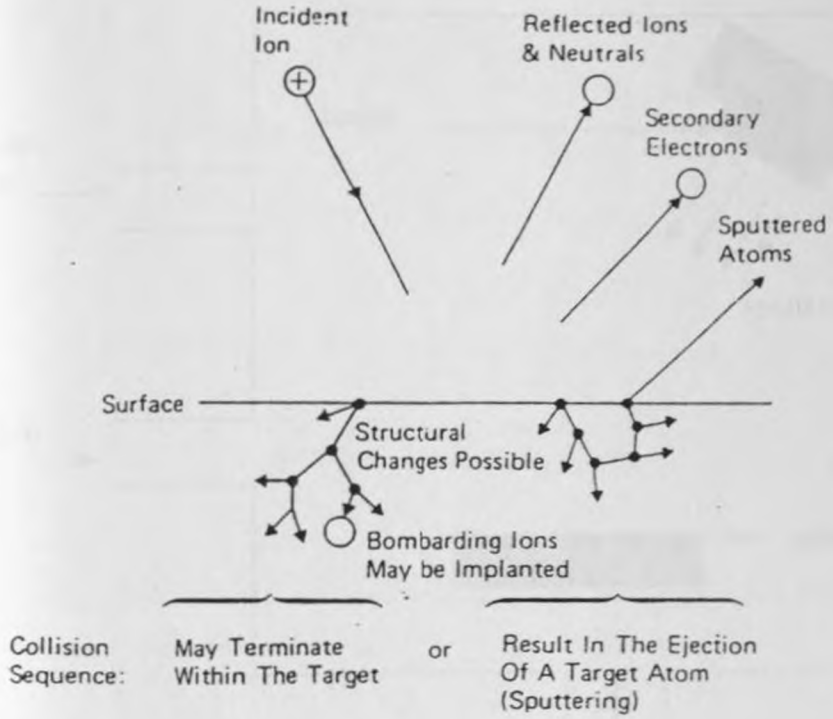

Fig. 3.11. Interaction of ions with the target surface [Chapman, 1980].

3.3.2.3.3 Reactive dc magnetron sputtering

We now discuss briefly the basics of reactive DC sputtering, the technique used in the current investigation. Reactive DC sputtering is a combination of DC glow discharge and a magnetron system, all in a reactive environment. The system consists of a cathode and an anode both of which are planar (figure 3.12). On applying a potential difference across the two electrodes in the presence of an inert gas like argon (Ar) and a reactive gas like oxygen (O_2) at reasonable pressure in the vacuum chamber, a glow discharge results. An increase of the applied potential results in an increase of the system current due to increased presence of electron and ions created by further collisions. This state is called Townsend discharge [Vossen and Cuomo, 1978]. The normal glow state (figure 3.13) is attained soon after when the number of electron and ions produced is the same and the plasma becomes self-sustaining. The brightness of the glow increases while the current raises steeply as potential drop, a state referred to as abnormal glow (sputtering state).

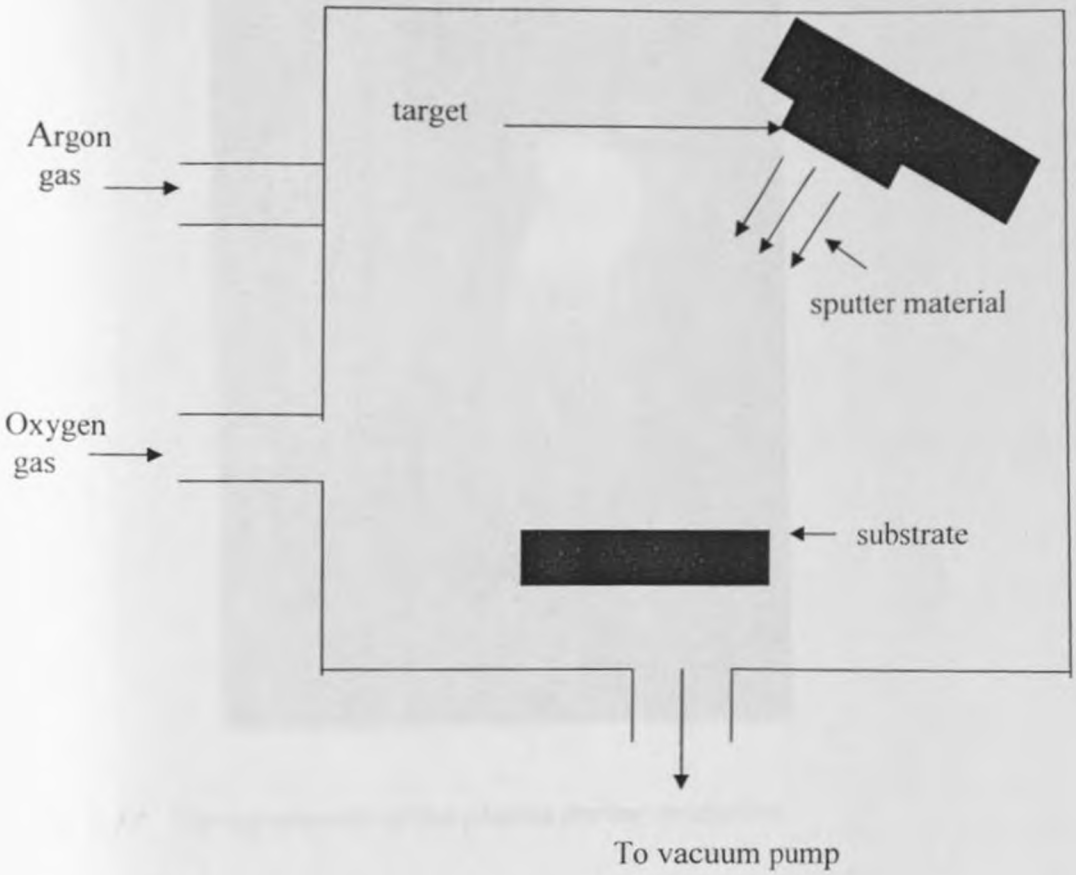

Fig. 3.12. Schematic diagram of the reactive DC sputtering system. The argon gas provides ions and atoms necessary to knock out sputter material from the target while the oxygen gas has the atoms that combine with the sputtered material to form an oxide.

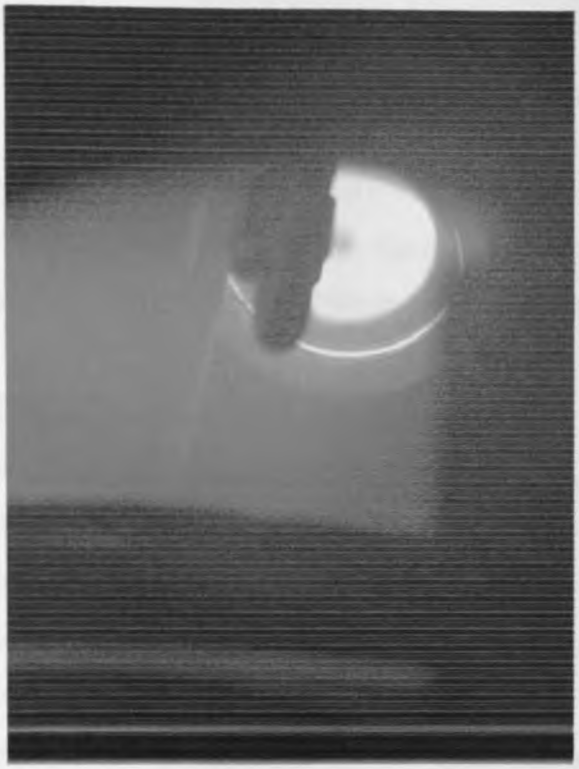

Fig. 3.13. The appearance of the plasma during sputtering.

A magnetic field is normally present in the sputtering system (that is why it is called magnetron sputtering) and the magnetic field simply increases the ionisation rate of electron by recycling electrons. When the electric field E, between the substrate and the target is subjected to a magnetic field of flux density B, the electrons between the substrate and the target experience a Lorenz force given by:

$$F_L = \frac{m_e d\upsilon_e}{dt} = -q[E + \upsilon_e \times B] \qquad (3.20)$$

where m_e, v_e and q is the mass, velocity and charge of the electron respectively.
An electron that leaves the cathode at velocity v_e and at an angle θ_e to B will experience a force $qv_eBsin\theta_e$ and which will be perpendicular to B. The electron will move in circular path of radius $r = mv_esin\theta_e/qB$. Through its helical motion, the

electron will spiral down the axis of the discharge with constant velocity $v_e cos\theta_e$. The magnetic field therefore enhances ionisation by:

1. Reducing the electron velocity to the walls to zero,
2. Increasing the path length of the electron by creating the helical orbit and creating more chances for the electron to ionise [Ohring, 1992].

3.3.2.3.4 The process of film formation

Thin film deposition basically consists of three major steps [Chopra and Kaur, 1983; Ohring, 1992; Smith, 1995]:

1. The transport of the material atoms to be sputtered to the substrate.
2. The adsorption and diffusion of the coating material (adatoms) onto the substrate surface to energetically suitable sites.
3. Movement of the coating atoms to their final rest positions by processes like bulk diffusion.

The first step is mainly controlled by the geometry of the deposition apparatus and deposition pressure while the second and third steps are controlled mainly by the substrate temperature. Figure 3.14 represents the three fore mentioned steps.

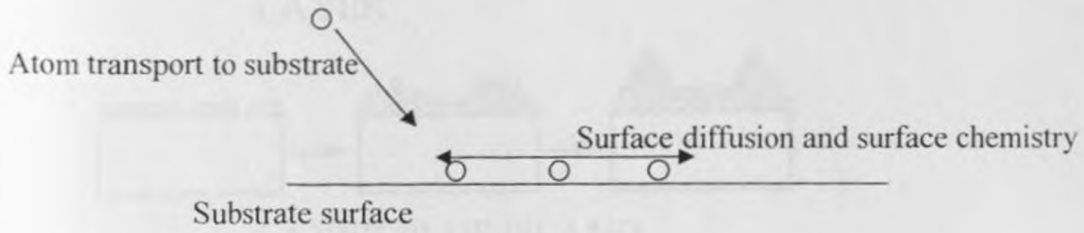

Fig 3.14. A Schematic representation of the three steps in a thin film deposition process [Thornton, 1986].

The exact process of film growth has been explained using three main models [Chopra and Kaur, 1983; Ohring, 1992]:

1. The coating species can be strongly bound to each other than they are to the substrate. This results in nucleation of the coating species and the formation

2. of islands. This is called the Island or Volmer-Weber model. Examples are metals grown on insulators.
3. In case the coating species are more strongly bound to the substrate than they are to each other, then a planar coating is produced. This is referred to as the Layer or Frank-van der Merwe model. An example is the growth of a metal on another metal of semiconductor on another semiconductor.
4. The third model combined the above two models and is the layer plus island or Stranski-Krastanov model. After the formation of one or more layers, islands begin to form because the layer formation becomes unfavourable. Growing of a metal on another metal or metal on a semiconductor is an example.

An illustration of the basic models is given in figure 3.15.

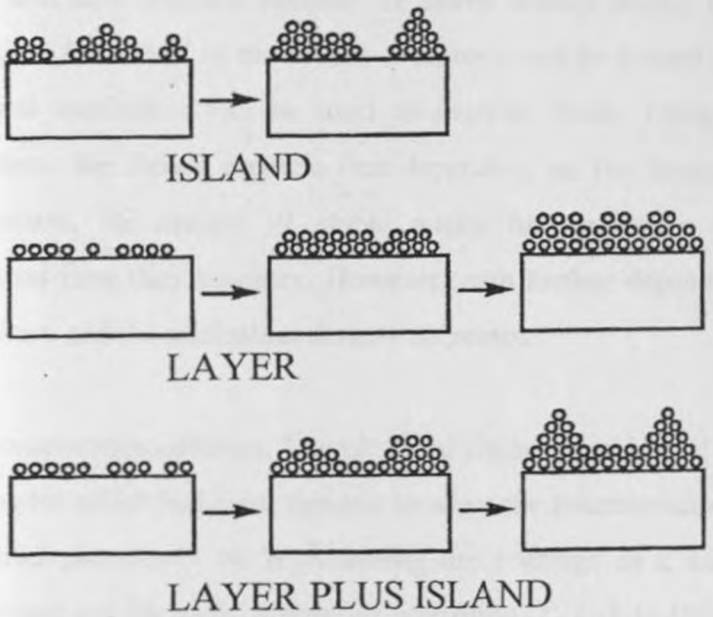

Fig. 3.15. The basic thin film growth model [Chopra and Kaur, 1983; Ohring, 1992].

Two theories have been proposed which describe the mechanism of film growth at its early stages:

Capillarity theory: This theory gives a thermodynamic description of the deposition process and presents a conceptually simple qualitative model of film formation. Through this theory, useful relations between deposition rate, film nucleus size and substrate temperature can be derived. The atoms or molecules create aggregates on the film surface that either grow in size or disintegrate into smaller pieces. The theory predicts higher critical nucleus with temperature elevation and therefore it will take longer to form a continuous film at higher temperatures. On the other hand, high deposition rates create smaller islands. However, quantitatively, it is inaccurate since thermodynamic concepts can only be applied to macroscopic systems, not a few atoms as the theory assumes.

Atomistic theory of nucleation: This theory describes the role played by individual atoms and how discrete number of atoms relates during the early stages of film formation. If clusters of molecules or atoms could be treated as macromolecules, then statistical mechanics can be used to describe them. Using the kinetic models of nucleation, the theory predicts that depending on the deposition rate and substrate temperature, the density of stable nuclei for nucleation increases linearly with deposition time then saturates. However, with further deposition nucleus coalescence takes place and the nucleation density decreases.

Using evaporation coatings, Movchan and Demchishin [1969] made the first structure-zone model which had been thought to relate the microstructure of a coating with key deposition parameters by representing the coatings as a function of the substrate temperature and the melting point of deposition (T_s/T_m). In 1974, Thornton applied this model to magnetron sputtered films [Thornton, 1974]. In his model, Thornton considered superposition effects such as surface and bulk diffusion and shadowing, a phenomenon brought about due to the angular incident of the deposition materials. The films' grain structure is determined by the physical process that dominates. When there is very low adatom diffusion, self-shadowing takes place and a columnar structure with open boundaries forms. This columnar structure with open boundaries is

particularly more pronounced at oblique incidence. The type of model can be used to predict the properties of the films and their structural characteristics.

3.3.2.3.5 Oblique deposition

In oblique deposition, vapour atoms of material to be deposited arrive at the substrate at an incident direction that makes a non-zero angle normal to the substrate as shown in figure 3.16 below. Due to the shadowing effect combined with limited adatom mobility, the resulting film assumes a columnar structure (see figure 3.17 below).

Oblique deposition was first used in 1959 by Knorr and Hoffman [Knorr and Hoffman, 1959] during an evaporation experiment and since then quite some work has been done on the subject [Robbie *et al.*, 1995; Abelmann and Lodder, 1997; Mbise *et al*, 1997; Robbie *et al.*, 1998; Sit *et al.*, 1999]. Between 1959 and1962, this technique was known and exploited in electron microscope to enhance contrast of weakly reflecting surfaces and emphasize surface roughness by decoration. It was ommercialised 30 years later using metal evaporated videotape.

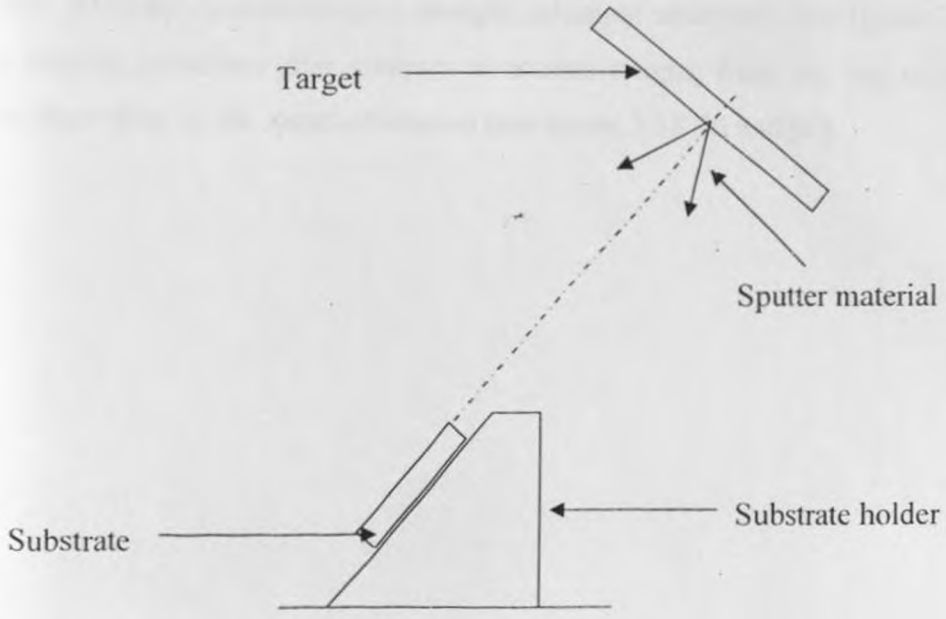

Fig. 3.16. The oblique deposition technique.

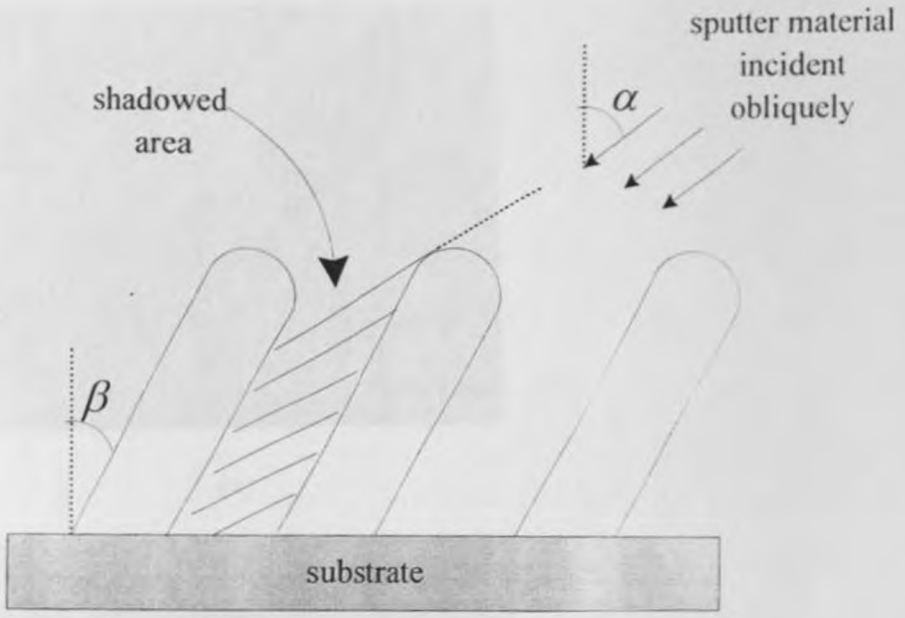

Fig.3.17. Schematic diagram showing obliquely deposited films forming columnar structure.

The substrate can either be stationary or in rotation and the resulting structures are different. Stationary substrates give straight columnar structures (see figure 3.18 (a)) while rotating substrates give complex structures ranging from zig zag to pillar to helices depending on the speed of rotation (see figure 3.18 (b) and (c)).

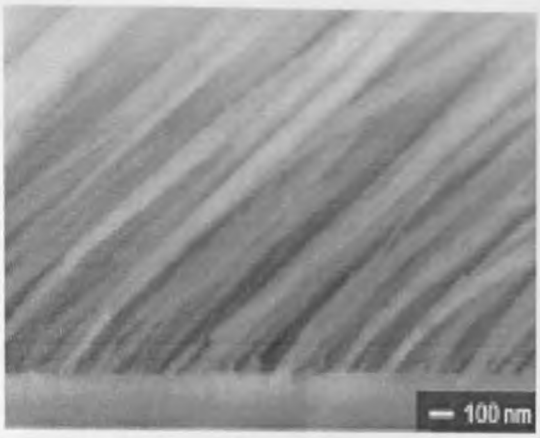

(a)

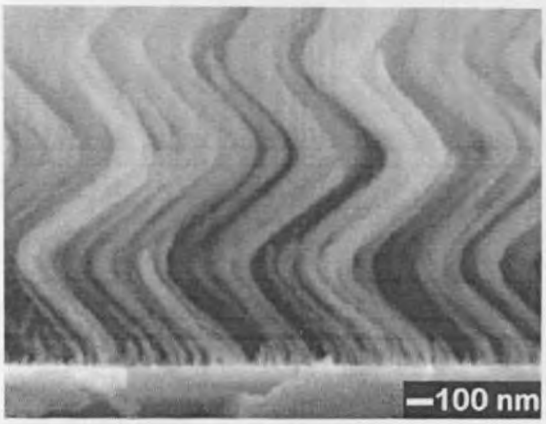

(b)

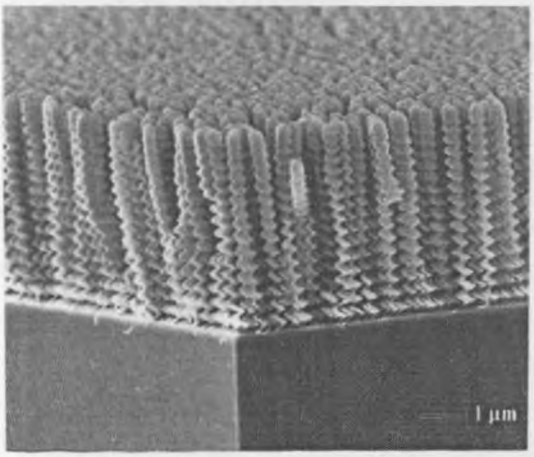

(c)

Fig. 3.18. Diagrams showing films formed on: a) stationary substrate (b) slowly rotating substrate (c) fast rotating substrate [Robbie et al., 1995; 1998].

Preliminary studies [Ohring, 1992] have tended to relate the angle between the film columns and the substrate normal (β), with the angle formed between the substrate normal and sputters beam direction (α). This famous rule is referred to as the tangent rule:

$$\tan\alpha = 2\tan\beta \qquad (3.21)$$

This rule holds true for alpha: $0 \leq \alpha \leq 90$.

This equation has no physical meaning; it is simply a description fitting a number of measurements. Further experiments have not provided any conclusive relationship between theta and beta [Messier and Lakhtakia, 1999]. Computer simulations have provided vital information on oblique deposition. Images similar to experimental findings have been obtained with two dimensional growth models simulated to low adatom mobility [Muller, 1985]. By using simple bombardment model for sputtering, surface relaxation and re-deposition of sputtered atoms, ballistic aggregation simulations have also been done [Brett, 1988]. Studies conducted using these models indicate that the films have structural, magnetic, electrical, optical and mechanical anisotropy properties.

3.3.2.4 The electrolyte.

An iodide/poly iodide (I^-/I_3^-) redox couple system was used in the present work. The iodide (I^-) prevents the recombination of the excited electron with the oxidized dye by releasing an electron to the dye while the poly iodide (I_3^-) takes the electrons regenerated at the counter electrode. The electrolyte should therefore have the properties like: a well matched redox-dye potential, a high diffusion constant and high reversibility and stability.

In a semiconductor, there are conduction and valence bands but in the electrolyte we have empty and occupied energy levels that are present in the dissolved redox system. As the redox molecules approach the semiconductor, they either donate or accept electrons depending on the energy level distribution in the redox couple. As a result of the fluctuations in the solvation shell surrounding the redox molecules, the energy

states of the redox couples are distributed within a certain range (see figure 3.19). Therefore the density of occupied states (D_{red}) and that of the empty states (D_{ox}) can be described using a Gaussian type of functions if the solvation shell approximates to the harmonic oscillator [Memming, 1980].

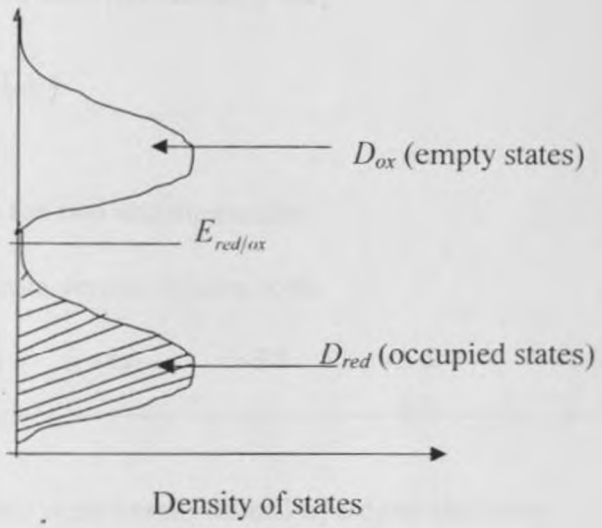

Fig. 3.19. The distribution functions of the redox system [Memming, 1984].

The energy positions of the level of the dissolved oxidized and reduced forms appear in the Gaussian function maximum. The solution redox potential of the redox couple $E_{red\,ox}$ is represented by the intersection point of the distribution of oxidized and reduced species. This is because this is the point where the probability of a level being occupied by an electron is half and so the Fermi level (E_F) in the liquid phase is represented by $qE_{red/ox}$. The potential $E_{red/ox}$ is calculated from the Nernest equation through [Memming, 2001]:

$$E_{red\,ox} = E^{o}_{red/ox} + \frac{R_g T}{nF} In \frac{\{ox\}}{\{red\}} \qquad (3.22)$$

where n is the number of electrons transferred in the redox reaction, R_g is the gas constant, T is the temperature, F is the Faraday constant, $\{ox\}$ and $\{red\}$ are the

oxidized and reduced species of the redox molecule and $E^{o}_{red/ox}$ is the standard redox potential when the concentrations of $\{ox\}$ and $\{red\}$ are equal. The redox potentials for normal hydrogen electrode and a semiconductor are different. In the former, it is defined as zero while in the latter it is the vacuum level. These two energy scales are related by [Claesson and Holmstrom, 1982].

$$E_{F} = -4.6 - qE_{red/ox}(eV) \tag{3.23}$$

Figure 3.20 shows the two absolute scales.

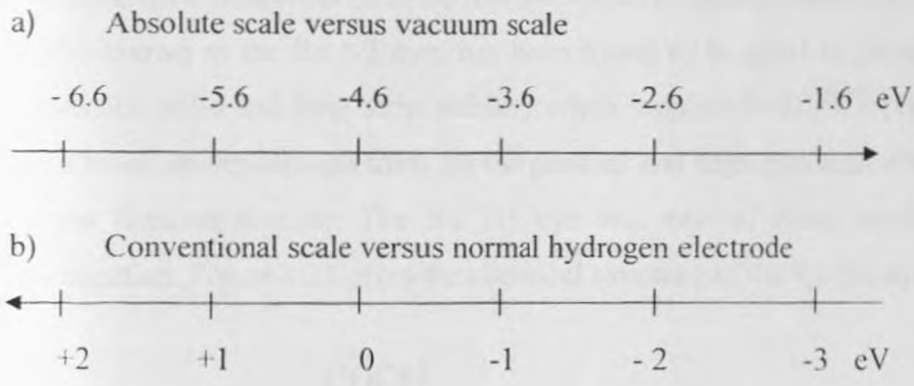

Fig. 3.20. Absolute energy scale used in semiconductors and the electrochemical scale with normal hydrogen electrode [Gomez, 2001].

3.3.2.5 The dye sensitizer

Due to photocorrosion, low energy band gap semiconductors are not appropriate for use as films in the fabrication of photoelectrodes for DSSCs. High-energy band gap semiconductors like titanium oxide are suitable since they cannot photocorrode under illumination. Their major disadvantage however, is that they are transparent to the visible part of the solar radiation (the range used for solar cell conversions). It therefore becomes necessary to incorporate a dye that should serve the purpose of absorbing the photons. It is in the dye where the incident photon energy is converted into electrical energy. The dye used in DSSCs should therefore possess these critical properties [Rensmo, 1998]. It should firmly adsorb onto the nanoparticles of the

semiconductor film, should absorb visible light of all colours (i.e., panchromatic), should have an acceptable extinction coefficient, should inject electrons to the semiconductor conduction band with 100 % efficiency, the energy level of the excited dye should match well with the lower level of the semiconductor conduction to minimise electron transfer losses, it should easily regenerate to a neutral state after electron acceptance from the redox couple and should be stable enough to withstand many years of operation.

3.3.2.5.1 The Ruthenium N3 dye

The cis-dithiocyanato-bis (2,2'-bipyridyl-4,4'dicarboxylate)-ruthenium (II) dye, which is also known as the Ru N3 dye, has been found to be good in performance both in conversion yield and long term stability when applied to DSSCs [Gratzel, 2003]. It has a broad absorption spectrum for the photons and high quantum efficiency on nano porous titanium dioxide. The Ru N3 dye was one of those used in the current investigation. Figure 3.21 gives the chemical structure of the Ru N3 dye.

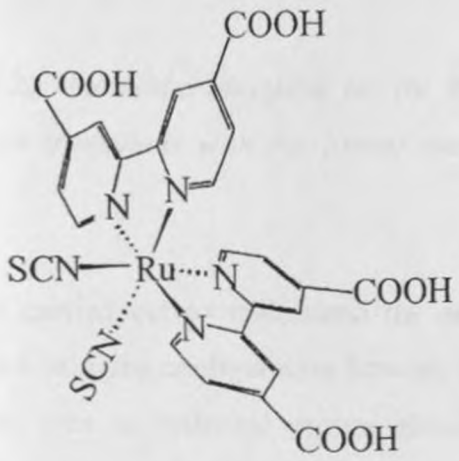

Fig.3.21. The chemical structure of cis-dithiocyanato-bis (2,2'-bipyridyl-4, 4'dicarboxylate)-ruthenium (II) dye (commonly referred to as N3) [Nazeeruddin et al, 1993].

In this type of dye, the thiocyanate groups are bound through the nitrogen and therefore the ruthenium assumes a distorted octahedral geometry. Electron

spectroscopy studies indicate that the highest occupied molecular orbital (HOMO) consists of pie (π) orbital of the NCS- groups and t_{2g} orbital of the ruthenium while the lowest unoccupied molecular orbital (LUMO) consists of mainly pie (π) orbital of the bi pyridyl groups (see figure 3.22 [Stefavovich *et al.*, 1990; Rensmo, 1998].

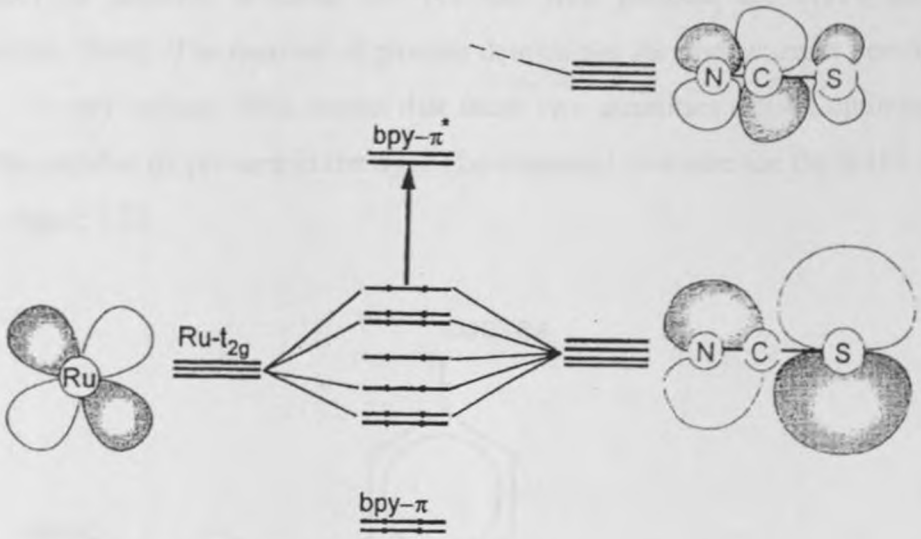

Fig. 3.22. Molecular diagram for the Ru N3 dye displaying the HOMO orbitals. Electron transitions with the lowest energy are displayed by the arrow [Rensmo, 1998].

Studies carried out to understand the orientation of the titanium dioxide particles suggest a bridging configuration between the carboxylate groups of the dye and either titanium ions or hydroxyl groups already attached to the semiconductor surface [Finnie, *et al.*, 1998; Rensmo *et al.*, 1998; Patthey, *et al.*, 1999]. The time for the injection of the electron from the dye to the titanium dioxide is in the femto second range [Asbury, *et al.*, 1999].

3.3.2.5.2 The N719 dye

Another dye used in the current study is the cis-bis(isothiocyanato)bis(2,2'-bipyridyl-4,4'-dicarboxylato)-ruthenium(II) bis-tetrabutylammonium (short formula- $RuL_2(NCS)_2$:2TBAL=2,2'-bipyridyl-4,4'-icarboxylicacid; BA=tetrabutylammonium), commonly called N719. One of the main differences between the N3 dye and N719 is the number of protons. Whereas the N3 has four protons, the N719 has two [Nazeeruddin, 2006]. The number of protons determines the photocurrent density and the open - circuit voltage. This means that these two quantities can be optimized by varying the number of protons in the dye. The chemical structure for the N719 dye is shown in figure 3.23.

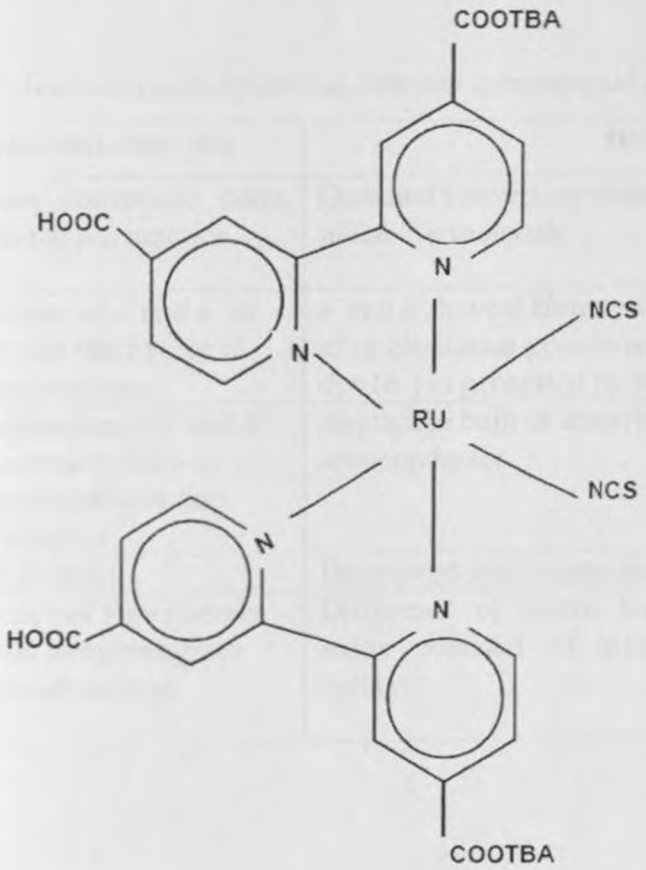

Fig. 3.23. The chemical formula for N719 dye [Nazeeruddin, 2006].

3.3.2.6 The counter electrode

The counter electrode (cathode) serves the purpose of accepting and releasing the electrons from photoelectrode (anode) through the external circuit to the electrolyte to compensate it for the electrons it released to the dye. It should therefore have a catalytic nature and should be efficient in injecting the electrons to the dye. Additionally, it should have a high surface area and high stability. Platinum has good properties for this. Either platinum is used or platinised glass substrates can be used.

3.3.3 Conventional solar cells versus DSSCs

We now mention some technological differences between the conventional solar cell and the DSSC based on our discussion above.

Table 3.1 Technological differences between conventional solar cells and DSSCs

Conventional solar cell	**DSSC**
Quantum conversion takes place in the p-n junction	Quantum conversion takes place in the dye molecule
Conduction of e^- and h^+ is similar and takes place in the semiconductor	e^- and h^+ have different conduction mechanisms. e^- after generation goes to semiconductor and oxidized dye (h^+) is generated by electrolyte
Recombination of e^- and h^+ is prevented by built-in electric potential in the semiconductor	Negligible built-in electric potential in the semiconductor
Lattice ordered	Disordered lattice nano particles.
Difference of Fermi levels of p- and n-regions gives open circuit voltage	Difference of Fermi level of semiconductor and redox potential of electrolyte gives open-circuit voltage.

3.3.4 Theory of charge transport in dye sensitized solar cells

In dye sensitised nanocrystalline solar cells, the generation and collection of electrons is described by the continuity equation [Peter and Wijayantha, 1999; 2000]:

$$\frac{\partial n_{ed}}{\partial t} = \eta_{eie}\alpha I_{ili} e^{-\alpha(\lambda)x} + D_e \frac{\partial^2 n_{ed}}{\partial x^2} - \frac{n_{ed} - n_o}{T_n} \qquad (3.24)$$

where n_{ed} is the electron density, x is the position of the dye in the TiO_2 film where electrons are released, n_o is the dark equilibrium electron concentration, η_{eie} is the net electron injection efficiency, $\alpha(\lambda)$ is the absorption coefficient of the sensitised TiO_2 film, I_{ili} is the incident light intensity, T_n is the electron lifetime and D_e is the electron diffusion coefficient. The first term on the right hand side of equation (3.24) is the rate at which the excited dye at x injects electrons into the TiO_2 film (electron injection), the second term is the rate at which electrons are transported to the back contact (electron collection) and the third term is the rate of electron trapping and detrapping i.e., electron back reaction or recombination.

3.3.4.1 Intensity modulated photocurrent spectroscopy (IMPS)

IMPS uses a frequency response analyzer or a lock-in amplifier to measure the complex ratio of the photocurrent flux to the incident light flux over a range of frequencies. This measurement is used to determine the transit time of the electrons from photon absorption to the time the electrons are detected via the external circuit. A phase shift between modulated light and photocurrent which can be detected by a response in the (+, +) quadrant of the complex plane plot indicates some recombination processes.

In the IMPS technique, a sinusoidally modulated light (illumination function-first term equation (3.24) above) having a small alternating current (ac) component (10 % or less of the dc component) is used to illuminate the solar cell. The ac component is described by the periodic time dependent function [Oekermann *et al.*, 2004]:

$$I(t) = I_o(1 + \delta e^{i\omega t}) \qquad (3.25)$$

where $\omega = 2\pi\nu$ is the modulation frequency and $\delta << 1$. The component of the incident photon flux is represented by δI_{ill}. The amplitude and phase shift of the photocurrent and photovoltage are then measured with respect to the illumination function. Usually the amplitude ratio and the phase shift give the transfer function. The transfer function can be plotted in a complex plane plot (imaginary component vs real component) or in a bode plot (imaginary or real component vs frequency).

Combining equations (3.24) and (3.25), the analytical solutions for the short circuit in IMPS is [Dloczik, *et al.*, 1997; Schlichthorl, *et al.*, 1997; Oerkerman *et al*, 2004]:

$$T_d = \frac{1}{\omega_{d-\min}} = \frac{1}{2\pi\nu_{d-\min}} \qquad (3.26)$$

T_d (electron transit time) provides an estimate of the time the photoinjected electron takes to the back contact and is determined by the film thickness as well as the amount of dye in the film, $\omega_{d\text{-min}}$ and $\upsilon_{d\text{-min}}$ are the minimum modulation and minimum frequencies for IMPS respectively.

3.3.4.2 Intensity modulated photovoltage spectroscopy (IMVS)

IMVS is a technique closely related to IMPS and it measures the complex ratio of photovoltage to incident flux for a range of frequencies. The concentration of electrons at the electrode in the steady state is determined by charge trapping, detrapping and recombination via the conduction band surfaces states. The electron lifetime, T_n is calculated directly from the semicircular plot on the complex plane according to the equation [Schlichthorl, *et al.*, 1997; Franco, *et al.*, 1999]:

$$T_n = \frac{1}{\omega_{n-\min}} = \frac{1}{2\pi\nu_{n-\min}} \qquad (3.27)$$

where $v_{n\text{-}min}$ is the frequency of the lowest imaginary component in the IMVS plot and $\omega_{n\text{-}min}$ is the minimum modulation frequency for IMVS.

Therefore for films of same thickness, T_d should provide a comparison of the electron transport properties in the films. The electron diffusion length, L_D, is calculated from

$$L_D = \sqrt{D_e T_n} \tag{3.28}$$

where D_e is the electron diffusion coefficient. L_D should be greater than the film thickness to enable efficient collection of electrons by the back contact.

3.3.3.5.2 Analysis of DSSC parameters using the equivalent circuit model

Equivalent circuit models are useful tools that help to visualize complicated devices. The equivalent circuit is a useful tool for understanding the output performance of solar cells and thereby giving information on areas of improvement.

A conventional photovoltaic solar cell can be modelled as a diode in parallel with a constant current source and a shunt resistor (see Fig. 3.6). The diode, constant current source and the shunt resistor are then in series with a series resistor [Aberle *et al.*, 1993; Koide *et al.*, 2006; Wanzeller *et al.*, 2004]. The constant current source models the photocurrent whose magnitude depends on the number of photogenerated electrons near the p-n junction. The diode models the electrical characteristics of p-n junction solar cells.

Electrical energy losses are modelled by a shunt and series resistor. The shunt resistor models all photocurrent losses. Photocurrent losses take place through current leakage across the p-n junction, exciton recombination due to the presence of crystal defects and or impurities in the cell. Photocurrents that do not flow through the external circuit flow through the shunt resistor. Shunt resistance however, has been found to have little effect on the performance of solar cell as a change of the shunt resistance from 100 Ω

to infinity only changes slightly the current-voltage curve. Solar cell performance is, however, very sensitive to series resistance [Prince, 1955]. Resistive losses mainly caused by resistance of the semiconducting materials metallic contacts, interconnections and semiconductor/metallic contacts are modelled by a series resistor [Koide *et al.*, 2006]. Part of the energy of the current through the external circuit is lost due to series resistance. For an ideal solar cell, the series resistance is zero and the shunt resistance is infinite.

By applying Kirchoff's laws to the equivalent circuit (section 3.3.1 and Fig. 3.6), we obtain equation 3.29 which is a current-voltage relationship based on the Schottky equation of thermionic emission [de Blas *et al.*, 2002; Koide *et al.*, 2006]:

$$I = I_{ph} - I_o \times \exp\left[\frac{q(V + I \times R_{series})}{n_{if} \times k \times T} - 1\right] - \frac{V + I \times R_{series}}{R_{shunt}} \qquad (3.29)$$

where R_{series} is the series resistance, R_{shunt} is the shunt resistance, n_{if} is the ideality factor ($n_{if} = 1$ for ideal solar cells and 2 for large recombination losses), I_o is the diode saturation current and I_{ph} the photo current.

Equation 3.29 applies to a single diode system and is a simplification of the real system. The Schottky approximation, however, gives good fits for most devices and can be used for general discussion of the shape of current-voltage solar cell curves. The analysis of the current-voltage curves involves determination of: short circuit current (I_{sc}), open circuit voltage (V_{oc}), maximum power output (P_m), fill factor (FF), the efficiency (η), series resistance (R_{series}) and shunt resistance (R_{shunt}).

Dye sensitized solar cells operate on a different principle to p-n junction solar cells as already discussed. This suggests that the equivalent circuit for a DSSC is different from that of the p-n junction solar cell. Indeed, comparison of the equivalents circuits for the conventional solar cell and DSSC show that the series resistance for the DSSC has two capacitors [Ferber *et al*, 1998; Koide *et al.*, 2006]. These capacitors create a

large time constant for DSSC's during measurement and therefore current-voltage measurements for DSSCs should be undertaken with prolonged delay time [Koide *et al.*, 2006]. However, since solar cells are normally operated under direct current conditions, the capacitors in the equivalent circuit of the DSSC can be omitted. This means that the equivalent circuit for the conventional solar cell can be applied to the DSSC [Koide *et al.*, 2006].

In the DSSC model, the series resistance represents the resistance due to redox reaction resistance at the platinum counter electrode, resistance due to carrier transport by ions in the electrolyte and sheet resistance of the back contact. Internal leakages in the solar cell are modelled by the shunt resistance.

CHAPTER 4

MATERIALS AND METHODOLOGY

4.1 Introduction

This chapter deals with the experimental methods and materials used in the present study. It provides information on how titanium dioxide thin films were deposited and characterized by different techniques as well as the fabrication of the dye sensitized solar cells and their characterization. Although all films were deposited in a vacuum chamber by reactive DC magnetron sputtering, some were deposited on substrates at elevated temperatures while others were deposited in ambient conditions (room temperature of the deposition chamber) followed by thermal annealing in air. In both the optimization of the deposition angle and compact underlayer, the films were deposited on a heated substrate, whereas for the thickness optimization, the films were deposited in ambient conditions prior to thermal annealing. Techniques such as x-ray diffraction, scanning electron microscopy (SEM) and atomic force microscopy (AFM) were used to characterize the films. The solar cells for optimization of deposition angle were not sealed while those for thickness optimization were sealed. The solar cells were characterized with regard to current-voltage (I-V), incident photon–to-current conversion efficiency (IPCE), intensity modulated photocurrent spectroscopy (IMPS) and intensity modulated voltage spectroscopy (IMVS).

4.2 Deposition of films by dc magnetron sputtering

4.2.1 Films deposited for optimization of deposition angle

The sputtering process was carried out in a Balzers UTT 400 vacuum chamber equipped with a turbo molecular pumping system. A titanium metal disc (5 cm in diameter and 0.625 cm thickness) and purity 99.9 %, was used as both the target and cathode, while the substrate was maintained as the anode. After pumping down to $\sim 10^{-7}$ mbars, argon gas (99.998%) was introduced into the sputtering chamber at a flow rate of 100 ml/min. A constant DC current of ~ 990 mA at power of ~ 385 W was applied to the target. To remove surface contaminants on the target, pre-sputtering was done for ~10 minutes in pure argon gas. Oxygen (99.998%), the reactive gas, was then

introduced into the chamber while maintaining the oxygen-argon gas ratio at 0.07. The working pressure was ~12 mTorr. The deposition was done on transparent conducting indium tin oxide glass substrates of sheet resistance 15Ω per square (Colorado Concept Coatings LLC) preheated to ~ 250 °C (Transparent fluorine doped tin oxide coated (SnO_2:F) or FTO glass substrates are better for solar cell applications but were not available). A vacuum tape was used to keep the substrates fixed onto the substrate holder and to provide a step for film thickness determination. The substrates were ~ 11.5 cm from the target and positioned to give a non - zero angle between the direction of the sputter beam and the substrate normal (deposition angle) as shown in figure 4.1 below.

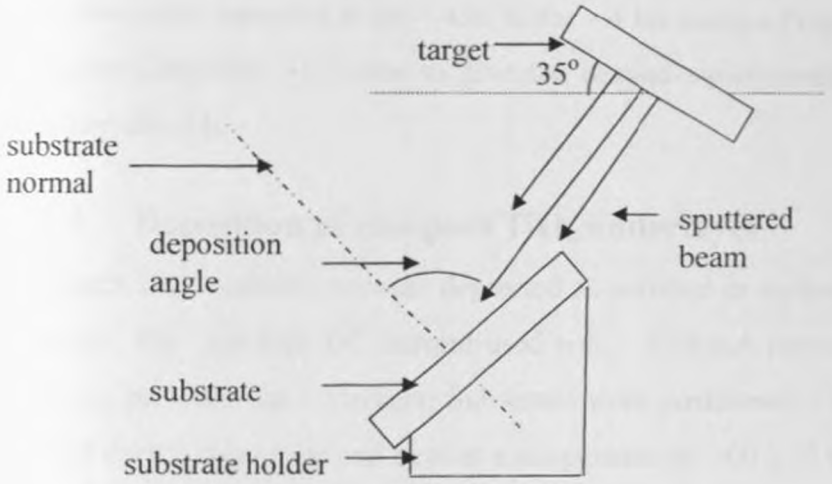

Fig. 4.1. Schematic set up of the deposition process defining the deposition angle.

To deposit films of similar thickness for comparison purposes, the reduction in deposition of sputter material due to erosion of the target was compensated by longer deposition times. Since the target erodes away as the sputtering process continues, the sputtering rate varies slightly with time during sputtering. Considering that the angle of deposition is also changing, the time needed to get a certain film thickness could therefore only be estimated. Since oblique deposition yields films that are not uniform in thickness across the substrate, the thickness indicated in our work was monitored at particular similar positions on the substrates. The pieces for SEM were cut from other parts of the film sample. The deposition angle was varied from 0 to 90 degrees and the

deposition rate was ~ 0.4 nm/s. The substrate was not rotated during the deposition process.

4.2.2 Films for thickness optimization

Deposition of titanium dioxide films for thickness optimization was done as outlined in section 4.2.1 above but with the following new parameters: The target DC current was ~750 mA at ~ 385 W. The oxygen-argon gas ratio was 0.02 with the argon gas flow rate at 100 ml/min. Transparent fluorine doped tin oxide coated (FTO) glass substrates (TCO-Hartford Glass Company, Inc.) with a sheet resistance of ~ 8 Ω/square were used as substrates. The substrate was not heated during deposition.
The films were annealed in air ~ 450 °C for ~ 4 hrs using a Programmable Nabertherm Program Controller S17 oven to give the desired stoichiometry and crystallinity of titanium dioxide.

4.2.3 Deposition of compact TiO_2 underlayer

Compact TiO_2 underlayers were deposited as outlined in section 4.2.1 but with these changes: The constant DC current used was ~550 mA powered at ~ 240 W. The working pressure was ~7 mTorr. Substrates were positioned ~ 13 cm from the target, rotated during deposition and kept at a temperature of 500 ± 5° C. The deposition rate was ~4.2 nm min^{-1}. Fluorine-doped tin oxide (FTO)-coated glass substrates (TEC 8, 8 Ω/square, Hartford Glass Company, Inc. USA) were first cleaned using detergent, rinsed in deionized water and dried in a stream of nitrogen gas, and then sonicated for 10 min in warm (55° C) acetone (>99.0 %), rinsed in deionized water and dried using nitrogen.

4.2.4 Deposition of a porous TiO_2 film on sputtered underlayer

A colloidal TiO_2 paste was applied onto the electrodes using doctor blading, followed by heating in a hot air flow at 450 °C for 30 minutes, thus forming a mesoporous TiO_2 layer of ~8 μm.

4.3 Fabrication of dye sensitized solar cells

In section 4.3.1, a detailed description of the fabrication of solar cells for the optimization of deposition angle is given while section 4.3.2 describes the fabrication of the solar cells for thickness optimization.

4.3.1 Dye sensitized solar cells for deposition angle optimization

Section 4.3.1.1 below gives a description of the preparation and sensitization of the working electrode. The counter electrode preparation is detailed in section 4.3.1.2 and both the working electrode and counter electrode are brought together to make the solar cell as outlined in 4.3.1.3.

4.3.1.1 Working electrode preparation and dye sensitization

The TiO_2 films were cut to 2.5 ×1.5 cm size for use as solar cell photoanode (working electrode). The films were heated in air at 450 °C for ~ 10 minutes to remove possible contaminants such as water vapour and volatile carbon contaminants and allowed to cool to ~80 °C before immersion into 2.3mg/10ml of alcohol cis-dithiocyanato-bis (2,2'-bipyridyl-4,4'dicarboxylate)-ruthenium (II) dye which is also known as the Ru N3 (Solaronix, S.A) in ethanol solution for a day. Excess dye was removed by dipping the sample in ethanol once.

4.3.1.2 Counter electrode (cathode) preparation

A substrate was cleaned using Kleenex ethanol and the conducting side covered with a thin film of platinum by spreading evenly, a few drops (~ 10 µl) of a solution of 5 mM H_2PtCl_6 in Isopropanol (Aldrich) and let to dry for a few minutes before heat treatment in air at ~380 °C for ~ 10 min.

4.3.1.3 Solar cell assembly

The solar cell was assembled by bringing together the photoelectrode and counter electrodes with the dyed titanium dioxide film facing the platinised side of counter electrode. To minimize short circuiting effect, a small piece of tissue paper was put between the two electrodes. The electrodes were then held in contact (with reasonable pressure) and a few drops of the electrolyte (0.5M LiI/0.05M I_2 and 0.5M 4-tert-butyl pyridine in 3-metoxypropionitrile (3-MPN)) introduced between the electrodes by capillary action. External contacts were made by applying conducting silver paint (Leitsilber, Hans Wolbring GbmH) on the conducting free side of each electrode. The cell's active area was 0.32 cm^2.

4.3.2 Dye sensitized solar cells for film thickness optimization

The dye sensitization (using N719 dye) of the titanium dioxide films for the solar cells for thickness optimization was done as explained in section 4.3.1.1 above. However, the solar cell assembly procedure was slightly different owing to improved fabrication techniques that offered more flexibility during measurements for the fabricated solar cell. In other words, this new solar cell assembly technique enables one to carry out several other measurements on the solar cell and offers better and safer handling of the solar cell.

4.3.2.1 Counter electrode (cathode) preparation

Before proceeding as in section 4.3.1.2 above, a hole was drilled on the counter electrode substrate from the conducting side using a Dremel Multipro 395VP drilling machine equipped with a diamond coated drill.

4.3.2.2 Solar cell assembly

A ring piece of surlyn 1702 frame with a 1 cm diameter hole (made by punching) was carefully cut out and cleaned in ethanol before placing it on top of the dyed working electrode. The counter electrode was carefully placed on top of the frame and held in position with a clamp with the conducting platinised side towards the working

electrode. The set up was put in a lamination device for ~ 1 min at ~100 °C in vacuum, before allowing it to cool for a few minutes. A few drops of the electrolyte (0.5M LiI/0.05M I_2 and 0.5M 4-tert-butyl pyridine in 3-metoxypropionitrile (3-MPN)) was introduced through the hole by capillary action. A square piece of surlyn (1x1 cm) was then placed on the hole and a covering glass of similar dimensions placed on the surlyn before applying heat using a soldering iron at ~250 °C for 2-3 s. Electrical contacts were made by applying silver paint (Leitsilber, Hans Wolbring GbmH) on the conducting side of each electrode. The cell's active area was 0.785 cm^2 (see figure 4.2 in section 4.4.2.2).

4.3.3 Underlayer TiO_2 thin film Solar Cells

Compact TiO_2-coated FTO working electrodes were sandwiched with thermally platizined FTO counter electrodes using a frame of thermoplastic (Surlyn 1702). An electrolyte, composed of 0.6 M tetrabutylammonium iodide, 0.1 M LiI, 0.1 M I_2 and 0.5 M 4-tert-butylpyridine in 3-methoxypropionitrile was introduced through a hole in the counter electrode that was sealed with Surlyn and cover glass afterwards. The cell's active area was 0.48 cm^2 (0.6x0.8 cm). The equivalent circuit for the thin film solar cells was obtained by fitting the data into Zview software (software for electrochemical measurements).

4.3.4 DSSCs incoporating TiO_2 underlayers

After depositing the compact and porous films as in sections 4.2.3 and 4.2.4 respectively, the substrate was let to cool to ~80 °C and the electrodes were immersed in an ethanolic solution of N719 dye overnight. After rinsing and drying, the sensitized electrodes were assembled with a counter electrode and filled with iodide/tridiode electrolyte. In some experiments a ferrocene / ferrocenium (Fc/Fc^+) redox electrolyte was used. This electrolyte was prepared by adding the oxidizing agent nitrosonium tetrafluoroborate to a solution containing 0.10 M Fc and 0.1 M $LiCF_3SO_3$ in 3-metoxypropionitrile, to obtain a final concentration of 0.09 M Fc and 0.01 M Fc^+. The cell's active area was 0.32 cm^2 (0.4x0.8 cm).

4.4 Titanium dioxide thin film and solar cell characterization

Below in section 4.4.1, we provide a description of the various techniques used to characterize the TiO_2 thin films deposited in this study. A description of the solar cell characterization technique is provided in a later section, 4.4.2.

4.4.1 Titanium dioxide thin film characterization

The details of the techniques used for TiO_2 thin film characterization are described in sections 4.4.1.1- 4.4.1.5.

4.4.1.1 Thickness determination

The film thickness was estimated using a Tencor Alpha–step 200 surface profilometry (resolution of 5 Å) equipped with a diamond stylus of radius 12.5 μm. During measurement, the stylus was moved across the film surface while keeping the sample and the sample stage stationary. The step created during the deposition process enabled the film's thickness to be read directly as the step height.

4.4.1.2 X-Ray diffraction measurements

X-Ray diffraction (XRD) measurements were used to analyse the structure of the prepared films. A computer controlled Siemens D5000 diffractometer equipped with a 1.54056 Å wavelength of Cu-Kα anode (as a spectral line) in a grazing incidence (2^{o}) set up and parallel beam geometry with an X-Ray Glöbel mirror was used. The Cu-Kα anode potential was kept constant at 45 kV at a current of 40 mA. In the XRD technique, a collimated beam of x-rays with a wavelength, λ, normally in the 0.7-2 Å range is incident on a sample and the crystalline phase of the sample material diffracts the rays according to Bragg's law. [Cullity, 1959]:

$$n_{do}\lambda = 2d\sin\theta_{diff} \tag{4.1}$$

where d is the crystalline atomic spacing and θ_{diff} is the diffraction angle and n_{do} is the diffraction order.

The intensity of the diffracted x-rays is measured as a function of diffraction angle $2\theta_{diff}$, giving some peaks for crystalline films. From the diffraction peaks, the particle sizes can be obtained. Since small crystalline particles cause peak broadening (small angular divergence) of the diffracted beam, a Gaussian fit to the diffraction peak gives the full width at half maximum of the diffraction peak. The particle sizes can then be calculated using Scherrer's formula [Cullity, 1959]

$$D_{ps} = \frac{0.9\lambda}{\beta_{FWHM}\cos\theta_{diff}} \tag{4.2}$$

where D_{ps} is the particle size, λ is the wavelength of the x- rays, β_{FWHM} is the full-width-at-half-maximum (FWHM) of the diffraction peak, and θ_{diff} is the diffraction angle. The observed diffraction patterns were compared to data from international standard files (International Center for Diffraction Data files) to identify the diffraction peaks while the particle sizes were estimated using Scherrer's formula

4.4.1.3 Porosity estimation

The film's density ρ_f, was obtained from:

$$\rho_f = \frac{m}{V_f} \tag{4.3}$$

where m is the mass of the film and V_f is the volume of the film.

The porosity $P_{porosity}$, of the film was then estimated from [Yoldas, 1980]:

$$P_{porosity} = \left(1 - \frac{\rho_f}{\rho_d}\right) \tag{4.4}$$

where ρ_d is the density of a non-porous film. The mass of the deposited film was measured by a Mettler PC 2200 weighing balance and the volume calculated from the film's surface area and thickness.

4.4.1.4 Optical measurements

Transmittance and reflectance measurements of the films (used in solar cell fabrication) in the visible light range were done using a double beam Perkin-Elmer Lambda 9 Spectrophotometer having a scan wavelength of 0.3 - 2.5 μm and equipped with a 150 mm integrating sphere. The spectrophotometer had two radiation sources: a deuterium lamp for UV range and a halogen lamp for visible (VIS) and near infrared (NIR) range. In the scanning process, the radiation source was changed automatically. During transmission measurements, the sample was placed in front of the integration sphere and behind it in reflection measurements. Some measurements were done before and after dyeing the film. The dye absorption in the film was then determined from the difference between the two measurements (transmittance before and after dyeing).

4.4.1.5 Scanning electron microscope (SEM) imaging

The morphological imaging of the films in this study was done using a Leo Gemini 1550 Field Emitting Gun (FEG) scanning electron microscope. In the SEM, electrons from a source are focused into a beam, having a spot size of, say, 5 nm and with energies of hundreds of eV to 50 KeV. Deflection coils raster the electrons over the sample surface. As the electrons strike and penetrate the surface, a number of interactions take place resulting in the emission of electrons and photons from the sample. SEM images were then obtained by the collection of the emitted electrons on a cathode ray tube.

4.4.1.6 Atomic force microscopy (AFM)

The roughness of the films was observed by the use of a Nanoscope IIIA, model NS3a atomic force microscope employing a silicon cantilever in the contact mode of operation.

In the AFM, the motion of a cantilever beam with a very small mass is measured. The AFM can be operated in two modes: contact mode (for both conducting and non conducting samples), and the tapping mode (for conducting samples). When used in the latter mode, the equipment is called a scanning transmission microscope (STM). The advantage of the AFM is its ability to take topographies of a range of surfaces, both conducting and non-conducting. During measurement, the small up and down deflections of the tip are measured as a constant force of contact is maintained at the cantilever. The cantilever has a nanoscale tip which scans across the sample surface to give the topographic image.

4.4.2 Solar cell characterization

Current-voltage (I-V) and Incident photon current efficiency (IPCE) were used to characterize the solar cells. Electron transport measurements were also undertaken to estimate the electron transit and lifetimes.

4.4.2.1 Current-voltage (I-V) measurements

In current-voltage (I-V) measurements, a constant beam of monochromatic light was incident on the cell. A sensitive current meter recorded the current as the voltage across the cell was varied. I-V measurements were done using a microwave powered sulphur plasma Light Drive 1000 lamp (type 1400-E2/1) solar simulator while data acquisition was computerized. The light intensity was measured by a Kipp & Zonen CM 11Pyranometer. Measurements were done at a solar intensity of 100 Wm^{-2} and 1000 Wm^{-2}. For DSSCs with compact underlayers, the IV curves under 1000 W/m^2

AM 1.5 G illumination were measured using a Newport solar simulator (Model 91160) and a Keithley 2400 source/meter.

4.4.2.2 IPCE measurements

Incident photon–to-current conversion current efficiency (IPCE) is the ratio of the photogenerated electron current to the photon flux incident on to the solar cell. It is calculated from the relation given in equation (3.18). IPCE measurements were done in a two-electrode set up. The light source was a 450 W Xe-lamp (Cermax model LX 300 UV lamp; ILC Technology) and the beam was transmitted through an 80 mm thick water filter into a monochromator (Schoeffel GM 252) onto a focusing lens. A beam splitter then split the beam into two: 10 % going to a reference photodiode detector and the rest, 90 %, to the sample. An optical power meter (photo dyne MODEL 44 XL) equipped with a silicon photodiode (model 400 AS) was used to calibrate the IPCE system. Action spectra (IPCE plot vs wavelength (λ)) were then obtained by illuminating the solar cell from the electrolyte side and back conduct side, commonly referred to as EE and SE illumination respectively (see figure 4.2).

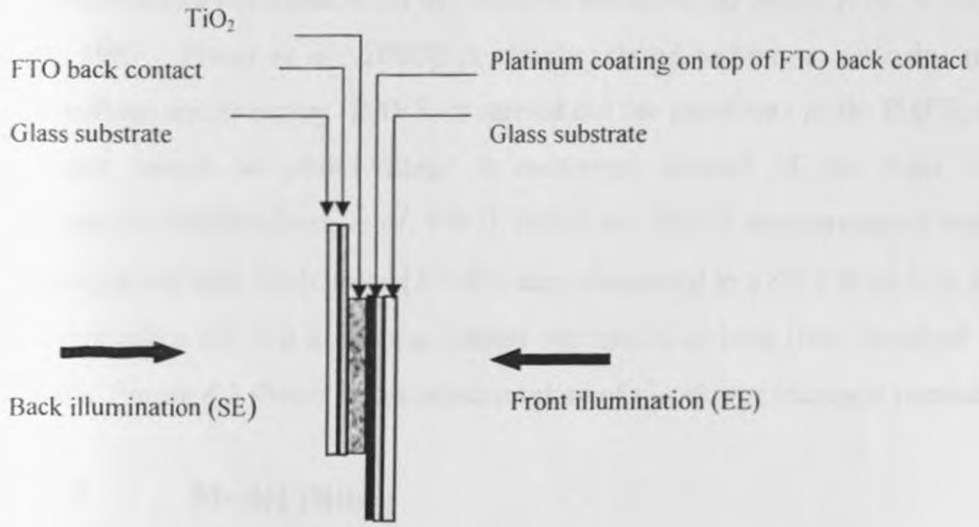

Fig. 4.2. Schematic representation of the fabricated solar cell defining back (SE) and front (EE) illumination.

4.4.2.3 Electrochemical measurements

Electrochemical characterization (linear sweep voltammetry and alternating current impedance measurements) was performed using a CH Instruments 660A potentiostat. During the measurements, the solar cells were connected to the potentiostat and the type of measurement selected from the system's computer software installed for the purpose. With the right settings for each measurement made, data was automatically taken and the files of data saved.

4.4.2.4 Charge transport measurements

Intensity modulated photocurrent spectroscopy (IMPS) is an analysis technique that provides information on the electron transit time to the back contact and on to the external circuit. Intensity modulated voltage spectroscopy (IMVS) on the other hand gives the electron lifetime before it combines with the redox. In IMPS, a small sinusoidally varying light intensity is superimposed on a larger steady background level. When the phase and magnitude of the photocurrent is measured in relation to the ac component, information on the kinetics as well as the transport of the electrons can be obtained like information on the electron diffusion [de Jongh *et al.*, 1996; Dloczik *et al.*, 1997; Fisher *et al.*, 2000]. A closely related technique, intensity–modulated photovoltage spectroscopy (IMVS) is carried out the same way as the IMPS, only that the open circuit ac photovoltage is measured instead of the short circuit ac photocurrent [Schlichthorl, *et al*, 1997]. IMPS and IMVS measurements were carried out using a red light diode laser (λ = 635 nm) connected to a SR 830 lock-in frequency amplifier and a SR 570 low noise current pre amplifier both from Stanford Research Systems. Figure 4.3 shows the schematic set up of the charge transport measurements.

4.4.2.5 Model fitting

We have used a current-voltage fitting model (IVFIT) developed by Burgers *et al* [1996] and Burgers [2004] via a simplified interface (EASYFIT software) for the same model by Filip Granek [2002]. The model is suitable for both single and double diode systems. The single diode model was used in this study (see Chapter 3, section

3.3.5) Among the techniques that one can choose from in the model is the Orthogonal Distance Regression (ODR), a mathematical technique for fitting errors in both voltage and current measurements (see the appendix for details). The error margin in our fitting was limited to a maximum of 2 %.

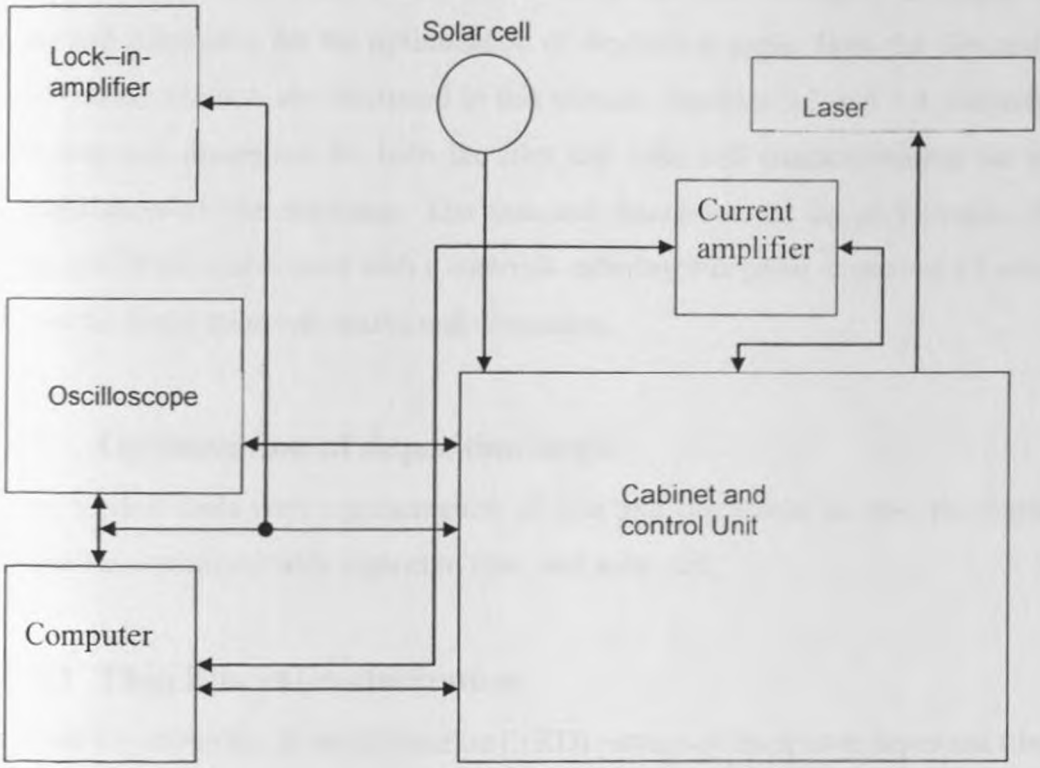

Fig. 4.3. Schematic diagram of the charge transport measurement technique. The arrows indicate the direction of signal flow.

CHAPTER 5

RESULTS AND DISCUSSION

5.1 Introduction

This chapter presents results and discussion of our work. Section 5.2 focuses on the data and discussion for the optimization of deposition angle. Both the film and solar cell characterization are discussed in this section. Sections 5.3 and 5.4 similarly give the data and discussion for both the film and solar cell characterization but for the optimization of film thickness. The data and discussion for the performance of thin film and DSSCs fabricated with a compact underlayer is given in section 5.5 while 5.6 gives the fitted solar cell results and discussion.

5.2 Optimization of deposition angle

This section deals with a presentation of data and discussion on how the deposition angle was optimized with respect to film and solar cell.

5.2.1 Thin film characterization

Figure 5.1 shows the X-ray diffraction (XRD) pattern of the sputter deposited films indicating their crystal nature. A mixture of anatase and rutile phases of titanium dioxide is evident with anatase being the dominant phase [International Center for Diffraction Data]. Anatase has been suggested as a better phase than rutile in solar cell applications due to the slow electron diffusion in rutile caused by its larger particle size [Lee *et al*, 2007; Takahashi *et al*., 2003].

The thickest film was the one deposited at 20°. The target was to have films of similar thicknesses (~1 μm) although the films were abit higher for deposition angles 0-40° mainly due to high deposition rates.

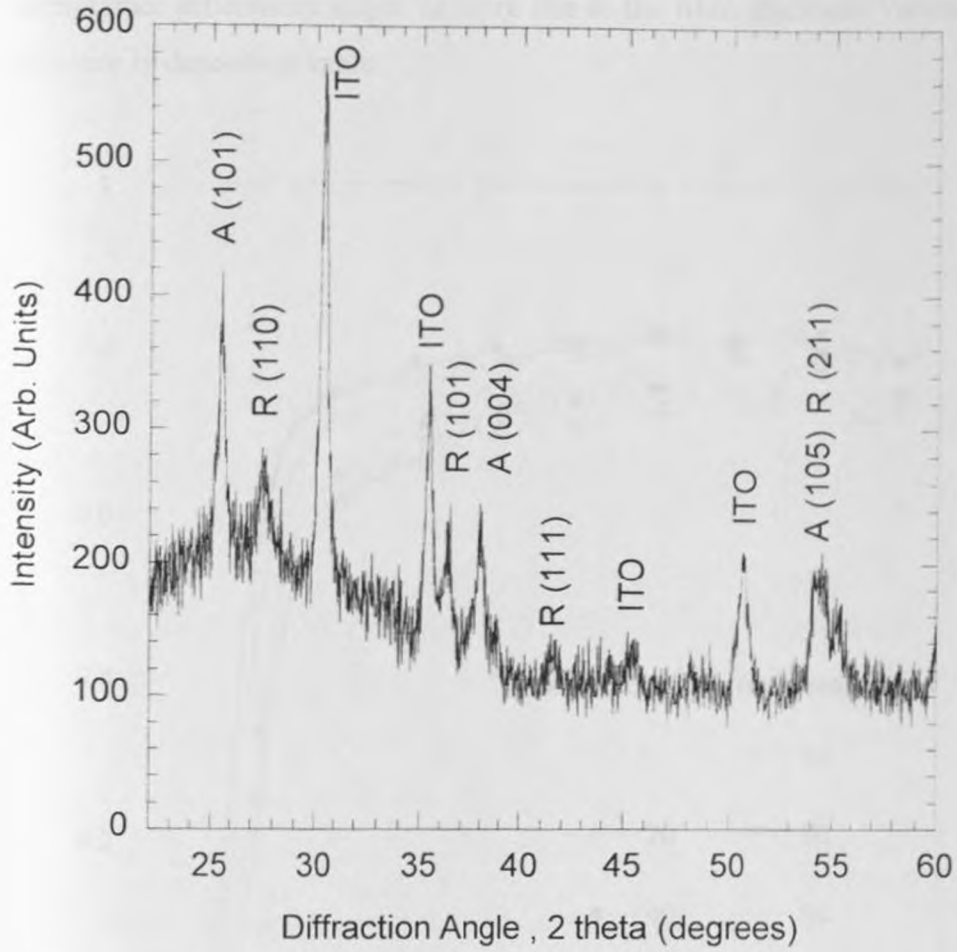

Fig 5.1. X-ray diffraction patterns of titanium dioxide thin films sputtered on ITO substrate at an elevated temperature of 250 °C. A = Anatase, R = rutile, ITO = Indium tin oxide.

The optical transmittance of the films (deposited at various deposition angles) is shown in figure 5.2. The films have a 60-80 % transmittance in the visible range. The transmittance increases with increase in deposition angle. However, the film thickness variation may also be a contributing factor. Thicker films are expected to scatter more incident light and therefore their transmittance is likely to be lower than that of thinner films; an observation evident from figure 5.2. It is also expected that the transmittance of films deposited at low deposition angles should be higher than those deposited at high deposition angles. This is not reflected in figure 5.2, suggesting that the

transmittance differences might be more due to the films thickness variation than the difference in deposition angle.

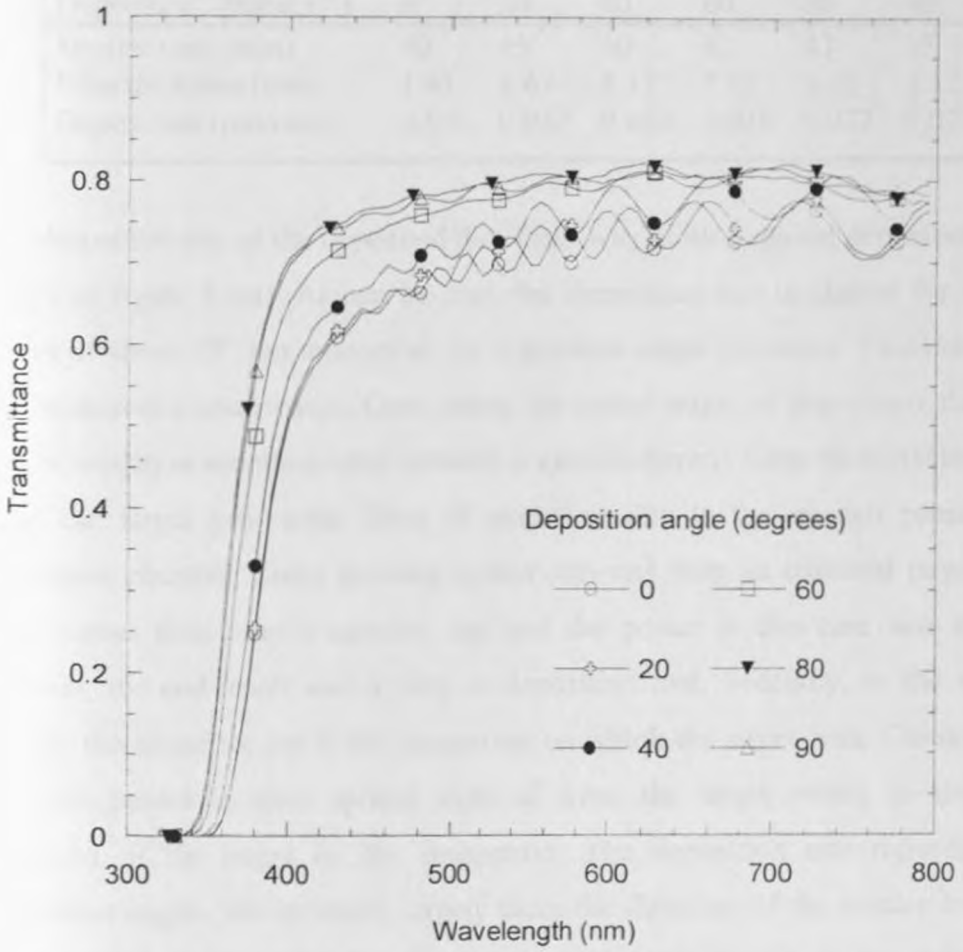

Fig. 5.2. The near-normal optical transmittance of the titanium dioxide thin films deposited at different angles as a function of wavelength.

A tabulation of the various film thicknesses at various deposition angles is shown in Table 5.1.

Table 5.1. Deposition angle and the corresponding film thicknesses obtained after sputtering at the different deposition angles.

Deposition angle (^{o})	0	20	40	60	80	90
Sputter time (min)	40	45	40	42	47	55
Film thickness (μm)	1.43	1.67	1.37	1.17	1.02	1.12
Depos. rate (μm/min)	0.036	0.037	0.034	0.028	0.022	0.020

The deposition rate of the deposited thin films was plotted against deposition angle as shown in figure 5.3(a). As can be seen, the deposition rate is highest for deposition angles of about 20°, but reduces as the deposition angle decreases. Two main reasons can explain this observation: One, during the initial stages of deposition, the target is free of oxidation and the sputter material is ejected directly form the metal target. With time, the target gets some form of oxidation due to the oxygen present in the deposition chamber. Since ejecting sputter material from an oxidized target requires more power than from a metallic one and the power in this case was maintained constant, the end result was a drop in deposition rate. Secondly, as the target gets eroded, the closer we get to the magnetron on which the target rests. Consequently, it becomes harder to eject sputter material from the target owing to the stronger attraction of the target by the magnetron. The deposition rate reduces. At low deposition angles, the substrate largely faces the direction of the sputter beam hence creating higher probability for the sputter material to deposit on the substrate with minimal losses. This is evidenced by high film thicknesses for only a short sputter time.

Figure 5.3 (b) shows film density normalized with respect to the average theoretical density as a function of deposition angle for a mixture of rutile and anatase (~ 4.05 g/cm^2). It is evident that the bulk density drops with an increase in deposition angle, implying that the film porosity increases the deposition angle is increased. This increase in porosity may be attributed to the creation of voids between columnar TiO_2 constituting the film. The effect is commonly ascribed to "self-shadowing", i.e., protrusions in the film preventing deposition in the spaces behind them; this

mechanism becomes more pronounced as the deposition angle is increased. Our findings concur with those of other researchers [Dirks and Leamy, 1977; Hara *et al.*, 1995; Mbise *et al.*, 1997]. The porosity of the photoelectrode in dye sensitized solar cell applications is important for it affects light absorption and electron diffusion; both of which determine the overall current-voltage (I-V) characteristics [Ni *et al.*, 2006].

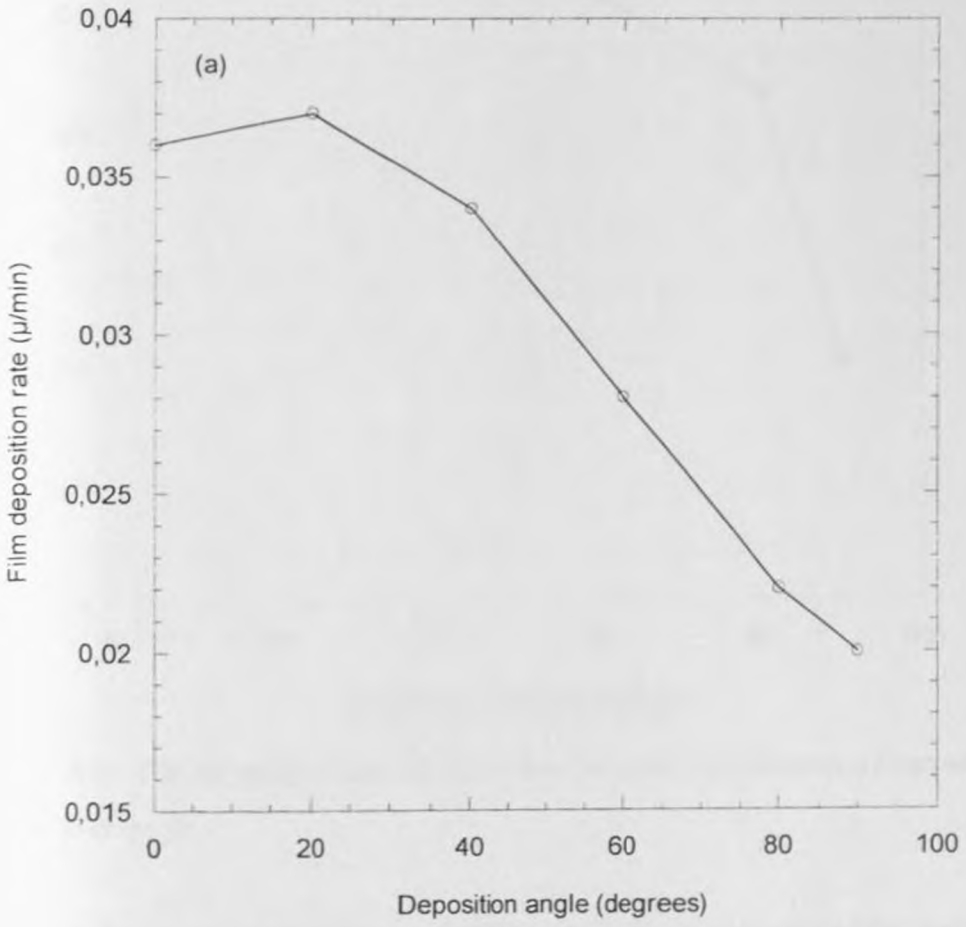

Fig. 5.3(a). Variation of the deposition rate of titanium dioxide thin films with deposition angle.

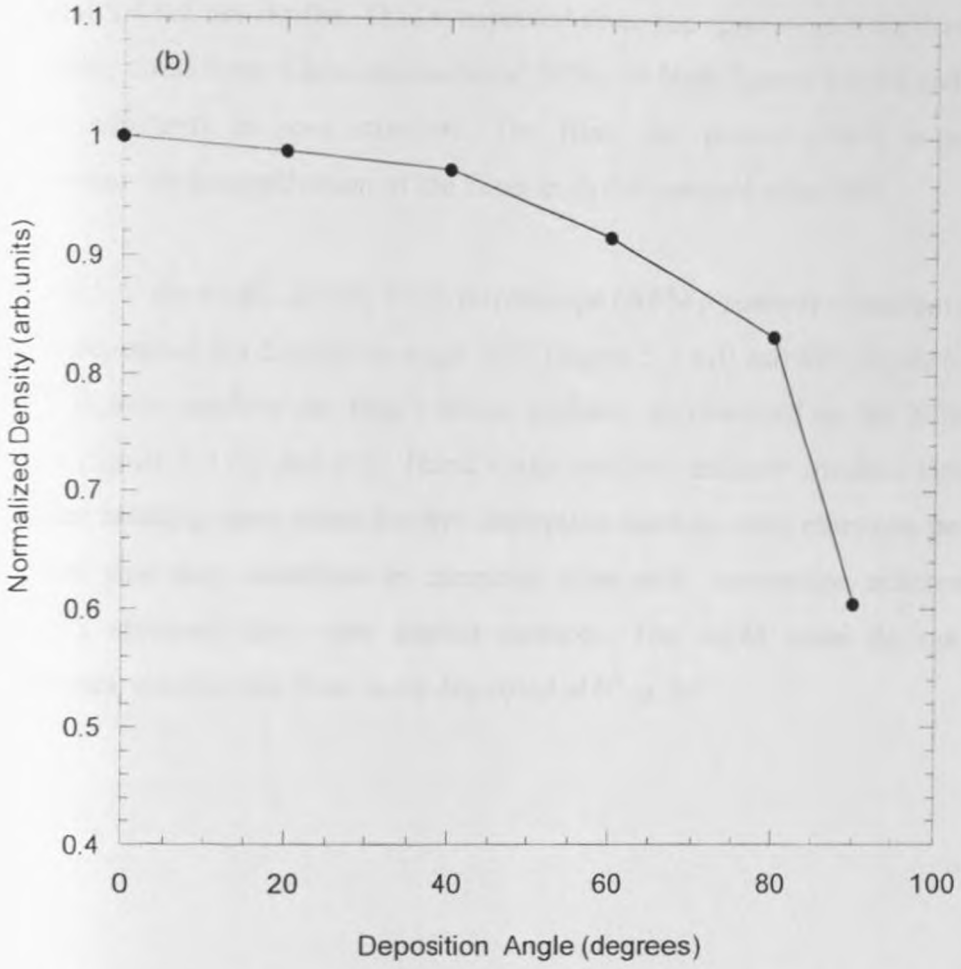

Fig. 5.3(b). The normalized density of titanium dioxide thin films as a function of deposition angle.

The top-down scanning electron microscope (SEM) micrographs of the surface of the films deposited at zero-deposition angle (normally deposited) are shown in Figure 5.4 (a). The film exhibits a rough cauliflower–like structure. Figure 5.4 (b) is the cross-sectional SEM image of the same film. Columns of TiO_2 and voids are clearly visible. The voids created during deposition provide good microstructure for dye adsorption and light scattering which subsequently increases the photocurrent when applied to dye sensitized solar cells.

The top-down SEM for films deposited at a deposition angle of 90^{o} is shown below in figure 5.4 (c) and the cross-sectional SEM in figure 5.4(d). Both top scans, figure 5.4 (a) and 5.4 (c), are similar. This is expected since the specimens were deposited under the same conditions. The cross-sectional SEMs in both figures 5.4 (b) and 5.4 (d) also show similarity in pore structure. The films are porous which is an important parameter for the application of the films in dye sensitized solar cells.

Figure 5.5 shows the atomic force microscope (AFM) scans for titanium dioxide thin films deposited at a deposition angle of 0^{o} (figure 5.5 (a)) and 80^{o} (figure 5.5 (b)).
Both figures confirm the film's rough surfaces as observed in the SEM top-down scans (figure 5.4 (a) and (c)). These rough surfaces enhance incident light scattering besides creating more space for dye absorption (and so more electrons per unit area), factors; that may contribute to increased solar cell conversion efficiency. Gomez [1999[a]] obtained films with similar surfaces. The AFM scans do not show any difference whether the films were deposited at 0^{o} or 80^{o}.

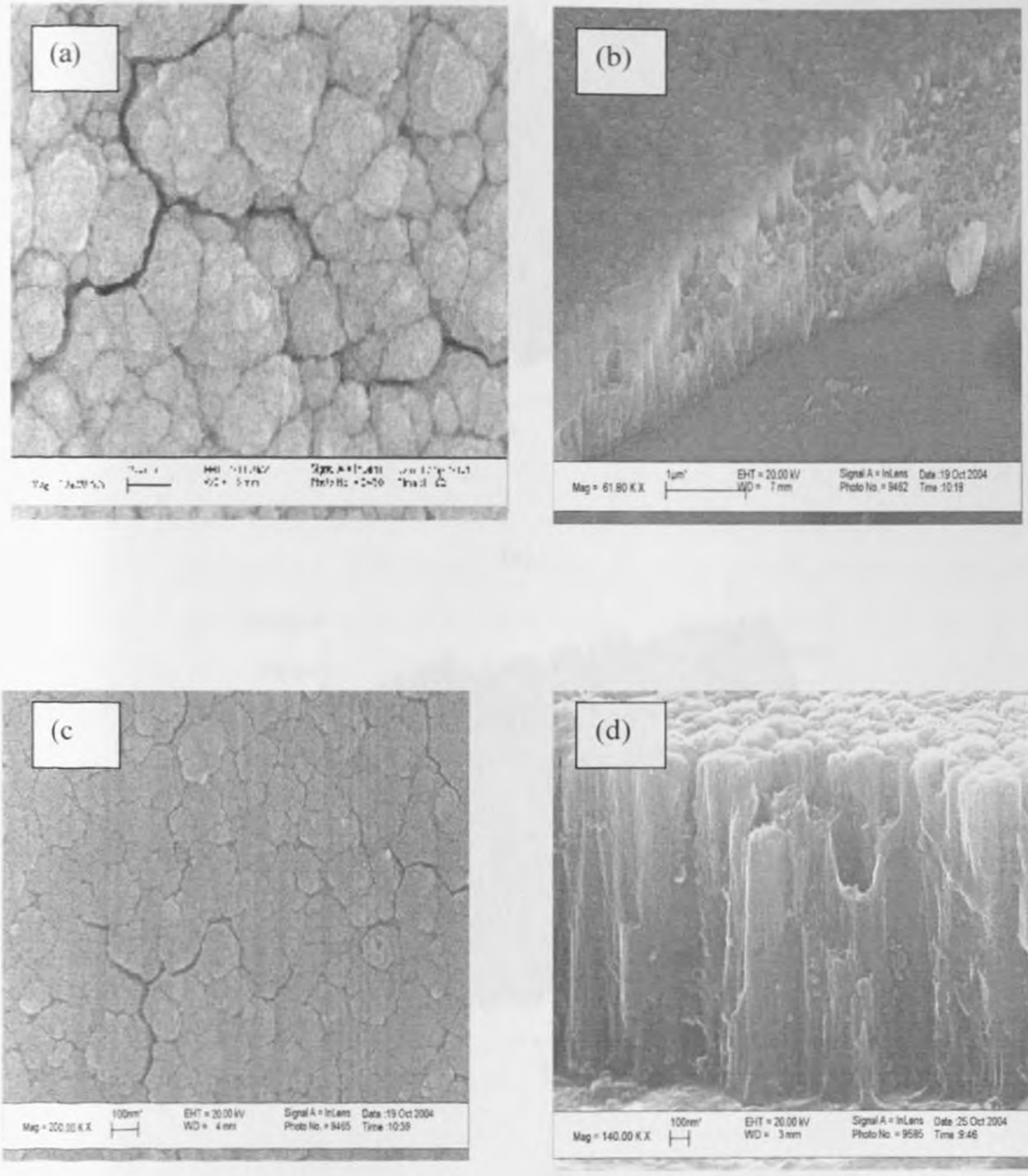

Fig. 5.4. Top-down (a) and cross-sectional (b) scanning electron microscope images for thin titanium dioxide thin films deposited at a deposition angle of 0° and top-down (c) and cross-sectional (d) scanning electron microscope images for titanium dioxide thin films deposited at a deposition angle of 90°.

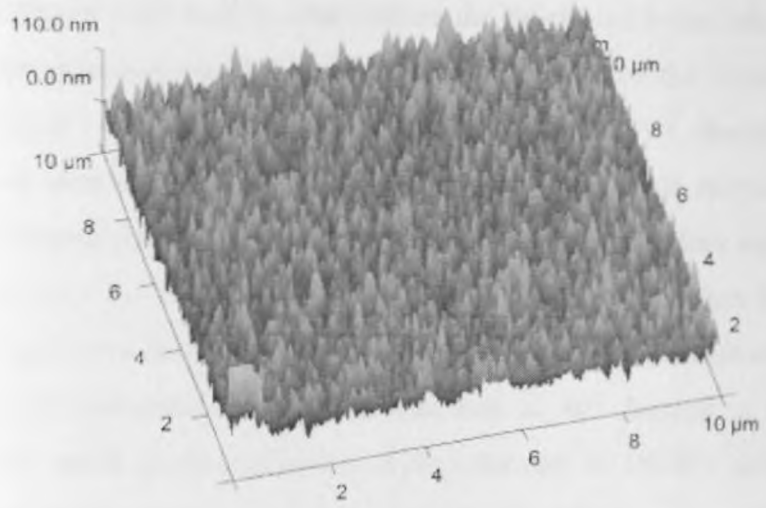

(a)

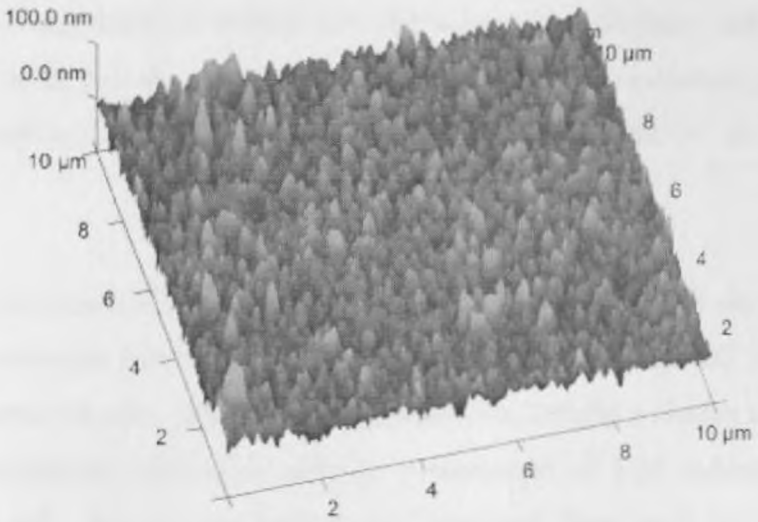

(b)

Fig. 5.5. Atomic force microscope images of titanium dioxide thin films sputtered at (a) deposition angle of 0°: scan length 10 µm (b) deposition angle of 80°: scan length 10 µm.

5.2.2 Solar cell characterization

Two techniques were used to characterize the fabricated solar cells: current-voltage and incident photon-to-current conversion efficiency. For the fabricated solar cells, Figures 5.6(a) and 5.6(b) show the current–voltage (I-V) characteristics and the variation of solar cell parameter values with deposition angle respectively. Table 5.2 gives the summarized data of the solar cell parameters. This data and the slope of the I-V curves show that the cells exhibit two short comings, *viz.*, they have a high series resistance and a low shunt resistance (from the near straight nature of the I-V curves). The solar cell fabricated from films deposited at 80° degrees is represented by a straight-line, which points to shorting of the solar cell. In DSSCs, series resistance has three components: resistance related to charge-transfer processes at the solar cell's counter electrode; resistance related to carrier transport by ions within the electrolytes; and the sheet resistance due to the substrate. Series resistance dissipates power in the solar cell and therefore reduces both the solar cell's efficiency and the fill factor. On the other hand, low shunt resistance provides an alternative current path for the photocurrent resulting in power losses and low fill factor [Koide *et. al.*, 2006; Green, 1992].

The photoelectric conversion efficiencies of the solar cells increase with deposition angle reaching a maximum level of ~1.3 % at a deposition angle of 60° (Figure 5.6(b)). The photocurrent density generated by the solar cells exhibit a similar trend to the photoelectric conversion efficiencies and has a maximum of 2.32 mA/cm^2 at a deposition angle of 60°. Suzuki and Taga [2001] obtained films with the largest surface area at a deposition angle of 70° which is close to the deposition angle that gave us the best efficiency. The open circuit voltage for the fabricated solar cells remains constant at ~0.46 V. The fill factor maintains a more or less similar trend as the open circuit voltage. The open circuit voltage is the difference between the fermi level in the TiO_2 semiconductor and the fermi level in the redox electrolyte on illumination. For the same semiconductor and electrolyte, much difference should not be expected in the open circuit voltage. For deposition angles higher than 60° drops in the efficiency and current density of the solar cells are recorded; observations

attributed to the lower film porosities (see figure 5.3(b)) and thicknesses (see table 5.1). High film porosities and thicknesses significantly contribute to higher photoelectric conversion efficiency and photocurrent density due to higher dye retention capability and therefore higher photon harvesting ability.

As observed earlier, DSSCs fabricated from thin films of thickness ~1 μm, had an open circuit voltage of ~ 0.4-0.44 V and a photocurrent density of ~0.69–2.3 mA/cm^2. Gomez *et al.* [2001] obtained an open circuit voltage ~ 0.7 V and a photocurrent density of ~0.58 mA/cm^2 for solar cells fabricated using films of ~1.1 μm in thickness. By comparing the results in this work and that by Gomez, it is noted that generally, the photocurrent density obtained in this study is higher than that by Gomez and colleagues. However, the photocurrent density for the solar cell fabricated from film's deposited at zero deposition angle is close to that obtained by Gomez but solar cells fabricated from films whose deposition angles were greater than 20° gave higher photocurrents.

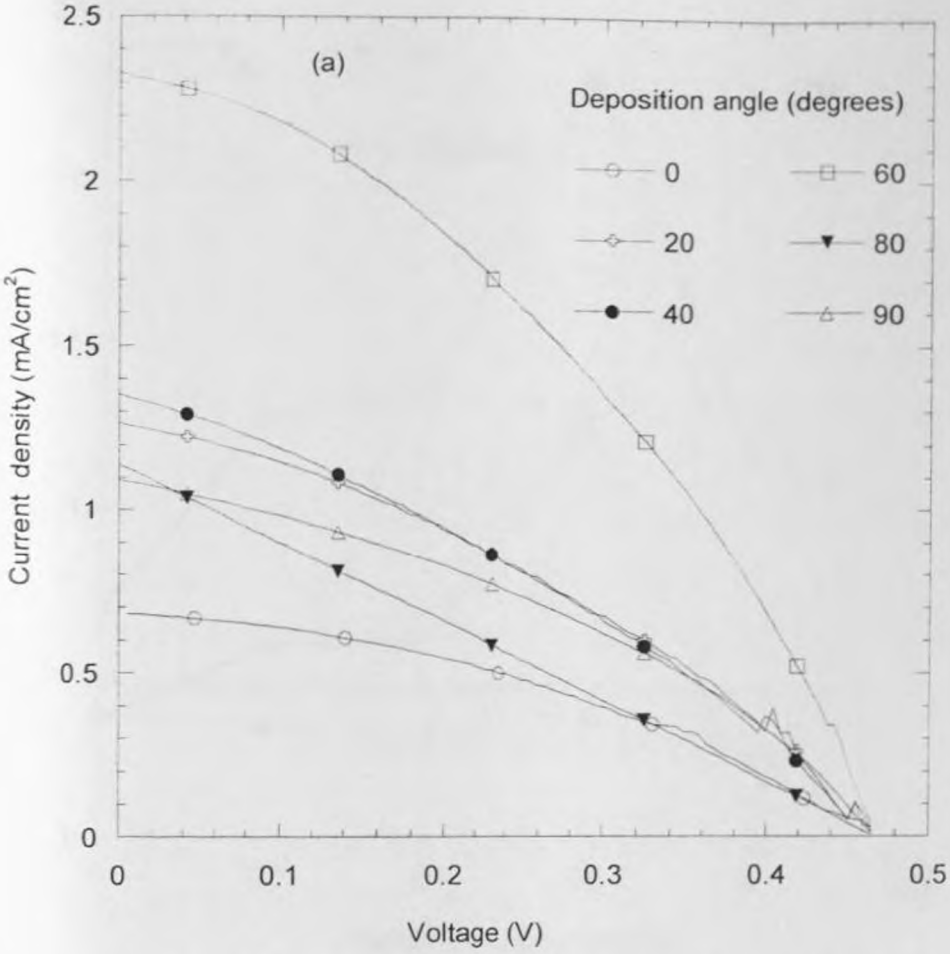

Fig. 5.6(a). Current-Voltage characteristics for solar cells fabricated from titanium dioxide thin films deposited at different deposition angles on ITO substrates at an elevated temperature of 250 °C and working pressure of ~12 mTorr.

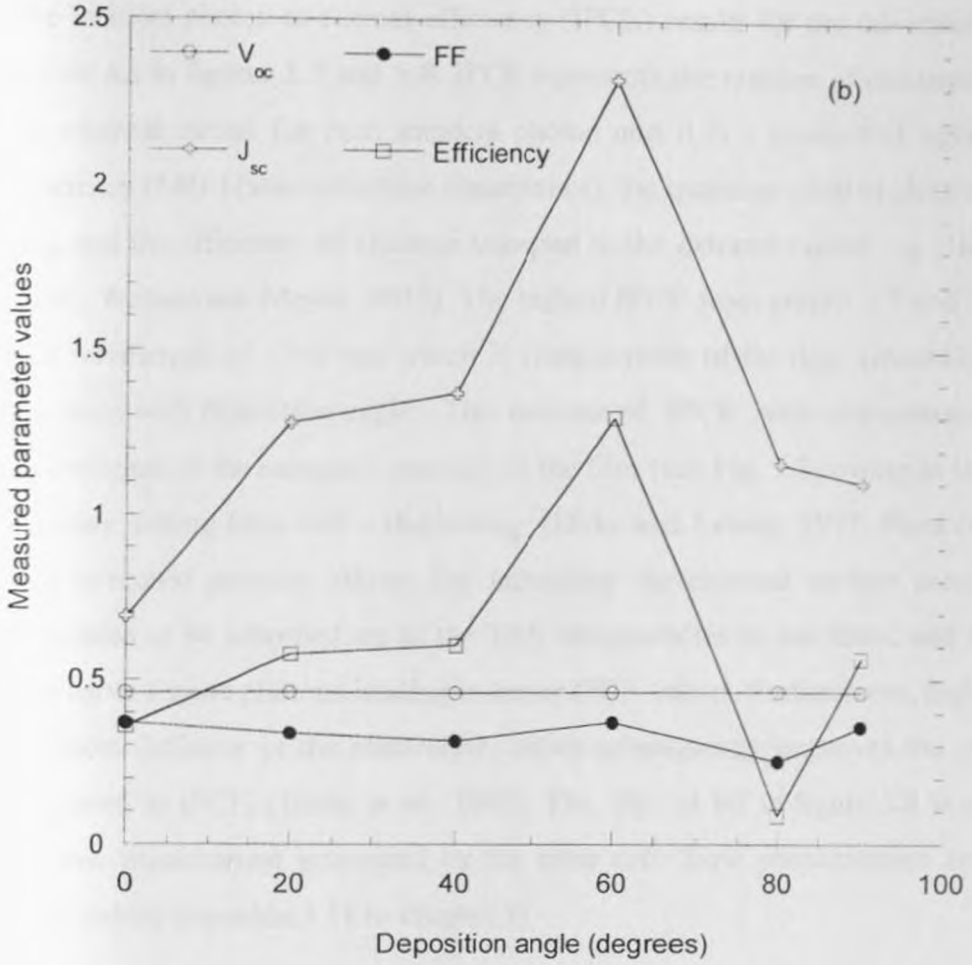

Fig. 5.6(b). Solar cell parameters extracted from experimental data plotted against the deposition angle of the semiconducting TiO_2 thin films used in fabricating the solar cells.

Table 5.2. Open circuit voltage V_{oc}, short circuit current I_{sc}, and photoelectric conversion efficiency for nano-crystalline solar cells incorporating TiO_2 films prepared at various deposition angles.

Deposition angle (°)	0	20	40	60	80	90
V_{oc} (V)	0.459	0.461	0.458	0.461	0.464	0.462
J_{sc} (mA/cm^2)	0.69	1.28	1.37	2.32	1.16	1.10
Fill Factor	0.368	0.337	0.312	0.371	0.251	0.355
Efficiency (%)	0.358	0.577	0.603	1.297	0.086	0.564

The Incident photon-to-current efficiency (IPCE) results for the fabricated solar cells are shown in figures 5.7 and 5.8. IPCE represents the number of electrons flowing in the external circuit for each incident photon and it is a product of light harvesting efficiency (LHE) (also called the absorptance), the quantum yield of electron injection, Φ_{inj}, and the efficiency of electron transport to the external circuit, η_e [Heimer *et al.*, 2000; Watson and Meyer, 2005]. The highest IPCE from graphs 5.7 and 5.8 is ~31% at a wavelength of ~540 nm which is characteristic of the dye. Generally, the IPCE increases with deposition angle. This increase of IPCE with deposition angle could be attributed to the increased porosity in the film (see Fig. 5.3) owing to the columnar structure arising from self – shadowing [Dirks and Leamy, 1977; Hara *et al.*, 1995]. The increased porosity allows (by increasing the exposed surface area) more dye molecules to be adsorbed on to the TiO_2 nanoparticles in the films, and the films in turn harvest more photons leading to better IPCE values. Furthermore, higher porosity enhances diffusion of the electrolyte, which subsequently improves the photocurrent (observed as IPCE) [Barbe *et al.*, 1997]. The 'dip' at 80° in figure 5.8 is attributed to the low photocurrent generated by the solar cell. Low photocurrents result in low IPCE values (equation 3.18 in chapter 3).

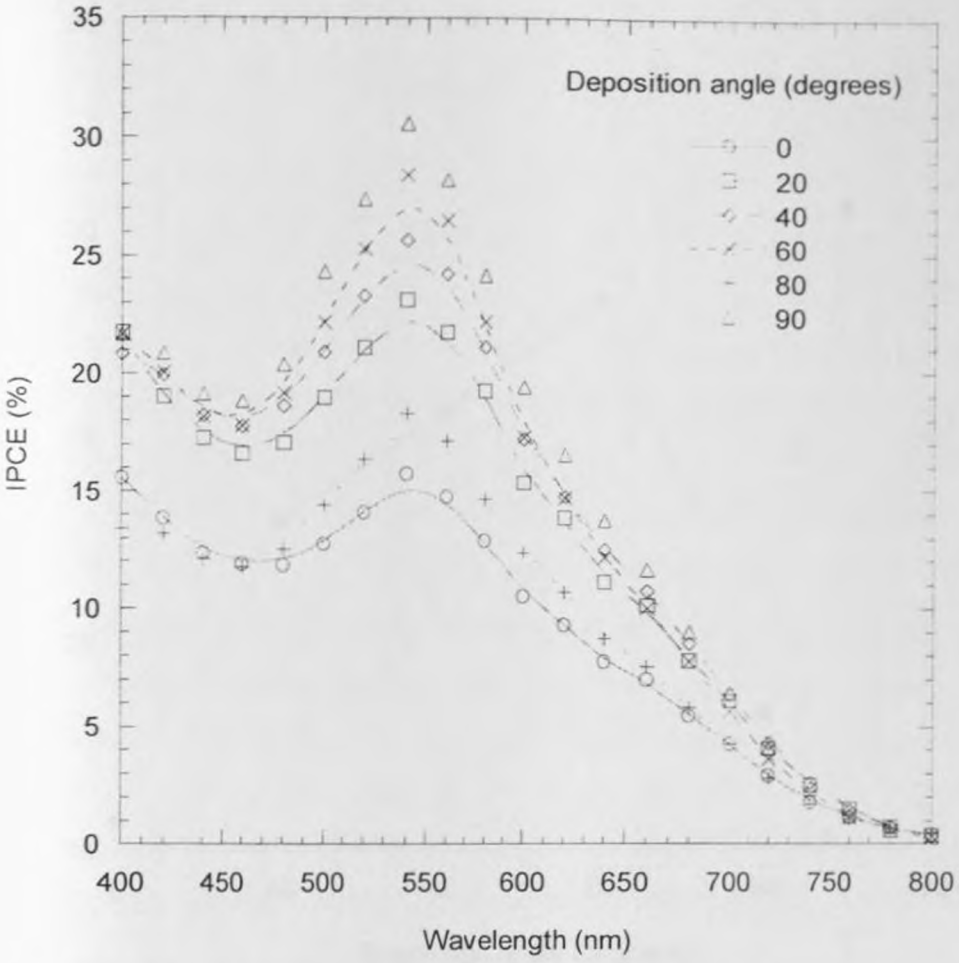

*Fig.5.7. **Incident photon-to-current conversion efficiency characteristics for solar cells fabricated from films deposited at different deposition angles.***

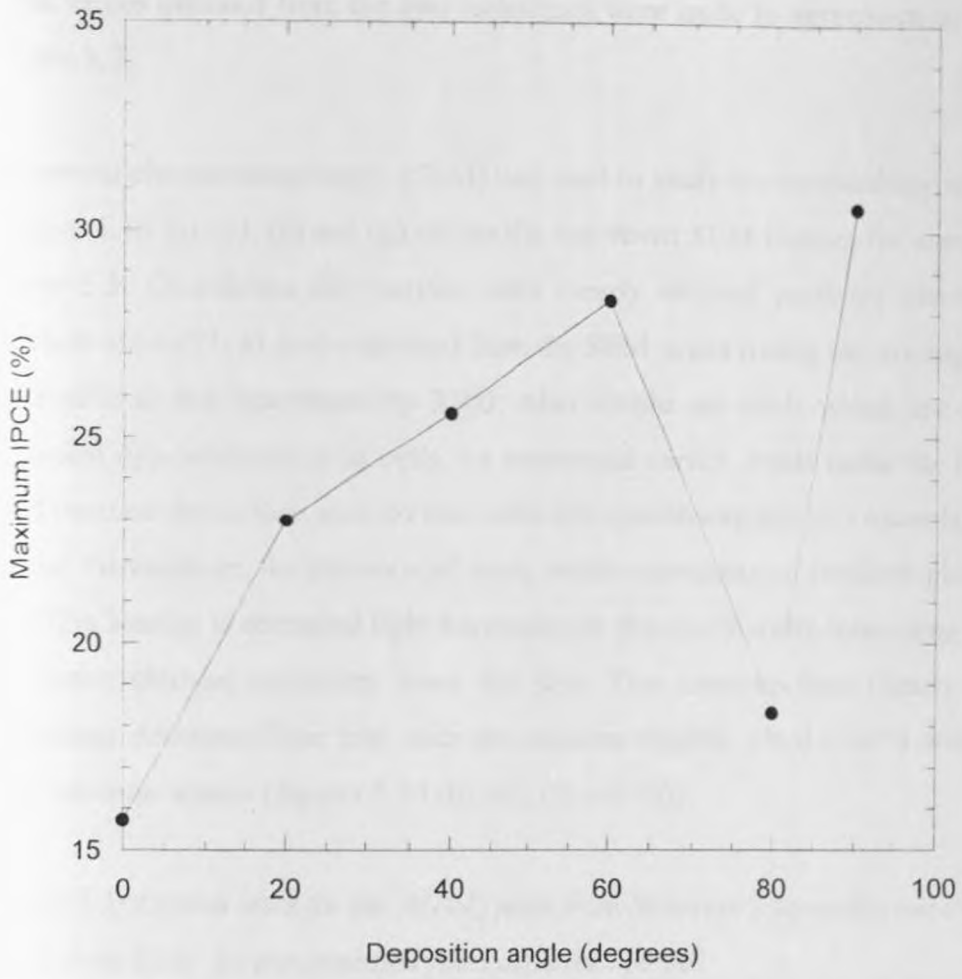

Fig. 5.8. The maximum incident photon-to-current conversion efficiency (IPCE) % (at a wavelength of 540 nm) values for the fabricated solar cells as a function of deposition angle.

5.3 Optimization of the film's thickness

5.3.1 Thin film characterization

In figure 5.9 is the X-Ray diffraction pattern for the sputtered titanium dioxide films. The as-deposited film has an amorphous structure with the observed peaks being related to the FTO back contact coating. On the other hand, the annealed films are crystalline, and predominantly anatase in phase. The particle sizes of the films were estimated from both the Scherrer's formula (equation 4.2 in chapter 4) by applying it to the A(101) peak, and from top-down scanning electron micrographs (SEM).

The values obtained from the two techniques were quite in agreement as indicated in Table 5.3.

Scanning electron microscopy (SEM) was used to study the morphology of the films. Figure 5.10 (a), (c), (e) and (g) shows the top-down SEM images for samples A-D of table 5.3. Cauliflower-like surface with clearly defined particles are visible. The particle sizes (27- 41 nm) estimated from the SEM scans (using the micrograph scales) is similar to that determined by XRD. Also visible are voids which are essential for efficient dye-sensitized solar cells. As mentioned earlier, voids make the films porous and increase the surface area, so that sufficient dye-absorption in a monolayer can take place. Furthermore, the presence of voids creates scattering of incident photons within the film leading to enhanced light harvesting by the dye thereby increasing the chances of more electron excitation from the dye. The cross-section clearly shows the columnar structure of the film with the columns slightly tilted (~10°) with respect to the substrate normal (figures 5.10 (b), (d), (f) and (h)).

Table 5.3: Crystal sizes for the A(101) peak from Scherrer's formula and the particle sizes from SEM for the annealed films deposited at 60°.

Sample	*Film thickness (μm)*	*Particle size (XRD) (nm)*	*Particle size (SEM) (nm)*
A	1.5	42.3	41.4
B	3.0	37.0	37.5
C	6.7	33.4	27.1
D	10.0	36.0	37.5

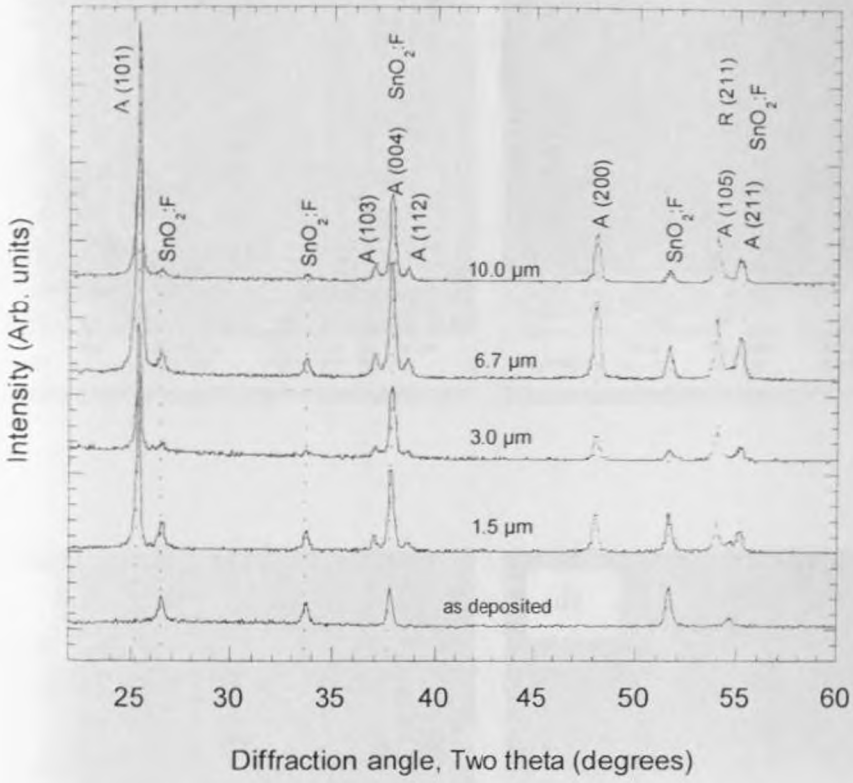

Fig. 5.9. X-ray diffraction patterns of the sputtered (deposition angle 60°) and thermally annealed titanium dioxide thin films.

Figure 5.11 (a) & (b) shows surface AFM images for samples B (3.0 µm) and D (10.0 µm) respectively scanned over a distances of 10 µm. The images show the film surfaces for both samples to be 'forests' of pillars protruding out indicating the films' rough surface. There is no distinct difference between the two images (sample D (10.0 µm) and sample B (3.0 µm)), an observation that agrees with the fact that the films were deposited under similar deposition conditions i.e., working pressure and temperature.

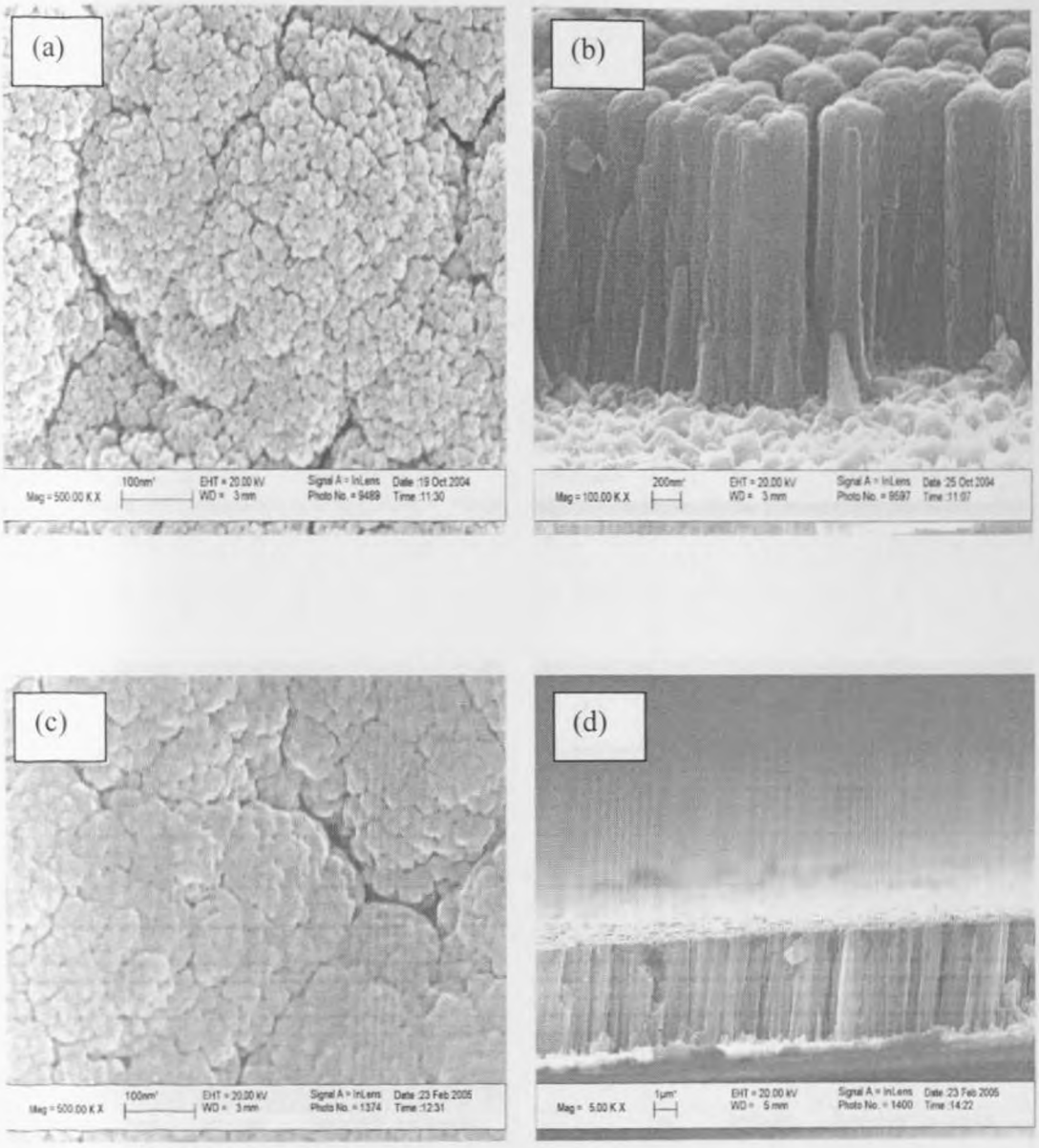

Fig. 5.10. Top-down and cross-sectional SEM images for the samples A(1.5 μm): (a)&(b); B(3.0 μm): (c)&(d); deposition angle 60°.

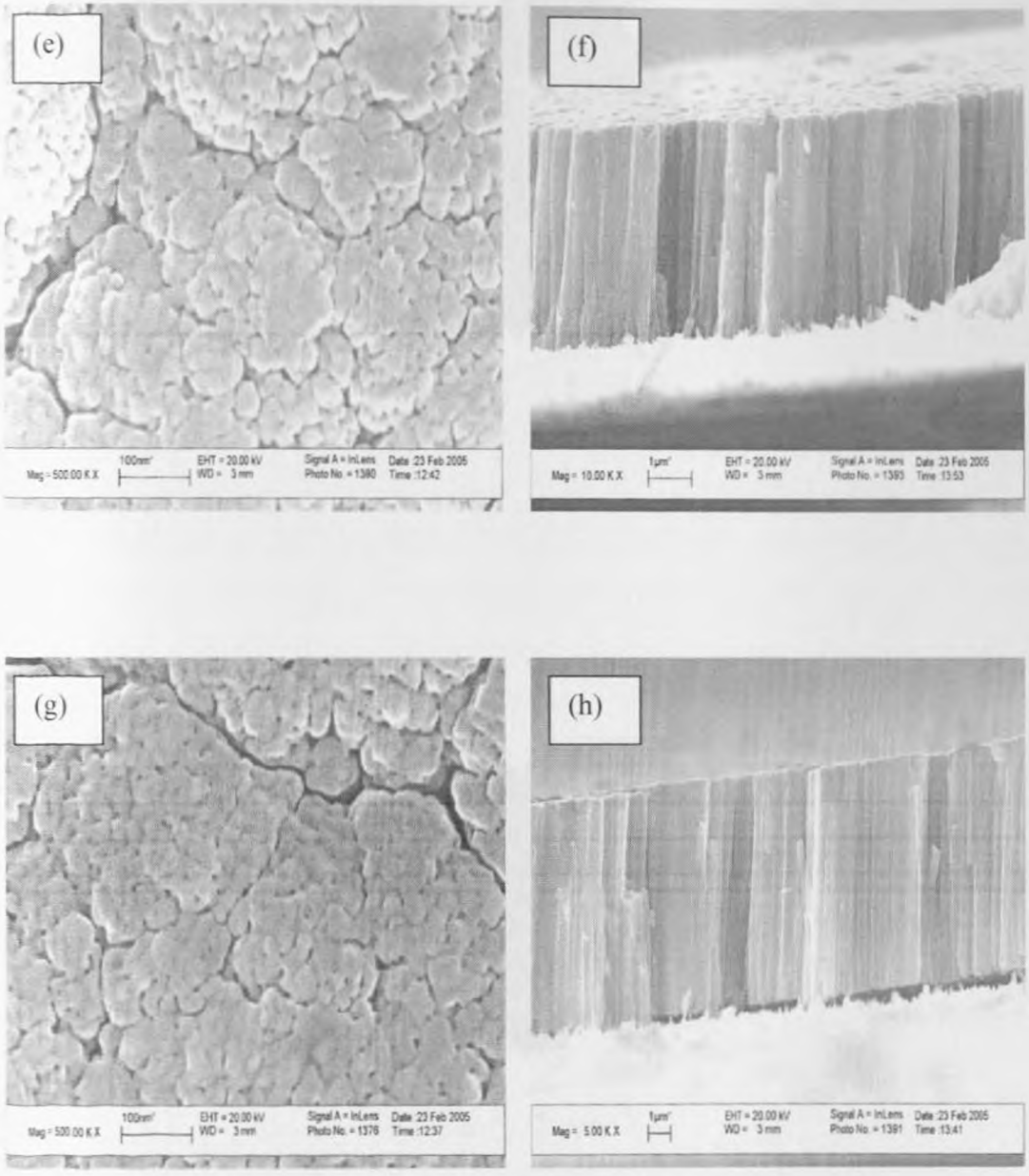

Fig.5.10. (cont) Top-down and cross-sectional SEM images for the samples C(6.7 μm): (e)&(f); D(10.0 μm): (g)&(h); deposition angle 60°.

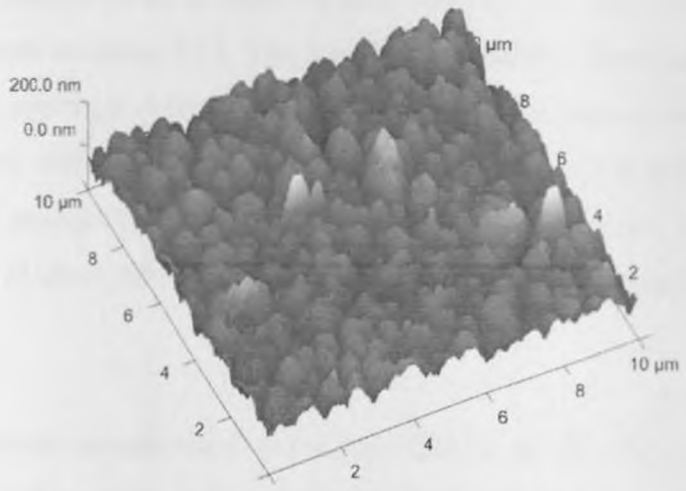

(a)

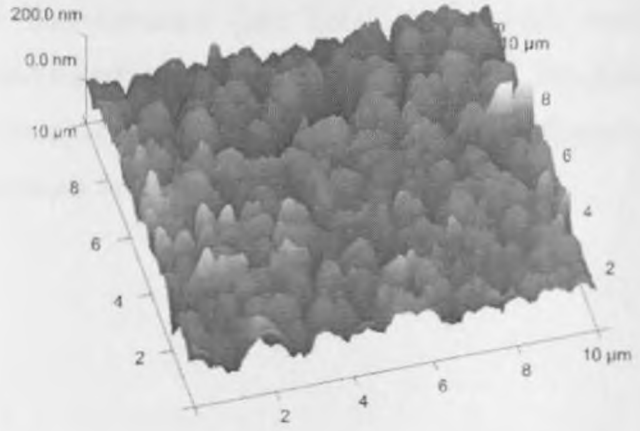

(b)

Fig. 5.11. Atomic force microscope images of titanium dioxide thin films of about 3.0 µm (a) and 10.0 µm (b); deposition angle 60°.

The optical transmittance of both the bare (with no dye) and dyed films in the visible range is shown in figure 5.12. The transmittance of the bare films was about 60 % for most of the spectrum range, whereas the dyed films show lower transmittance. The transmittance difference between the bare and dyed films is due to the absorption of the incident photons by the dye. The 'dip' in the transmittance of the dyed films at a wavelength of about 500-560 nm indicates the maximum absorption of the photons by the dye.

The total optical transmittance of the bare films is in the range of 50-60 % except at low wavelengths (<550 nm) where the transmittance seems to decrease due to increased light absorption by the films. Titanium dioxide films have been found to absorb light whose wavelengths are below 550 nm, with the strongest absorption in the ultra violet [Karunagaran *et al*, 2003]. The transmittance of the dyed films seems to decrease with increase in film thickness in the wavelength range 400-700 nm. As the film gets thicker, there is both more space creation and higher surface area owing to the longer film columns (see figure 5.10). This results in increased dye accumulation and therefore higher photon absorption. The lowest transmittances for the dyed films occur at 400 and 540 nm due to metal-to-ligand charge transfer [Bauer *et al*., 2002] as shown in Table 5.4.

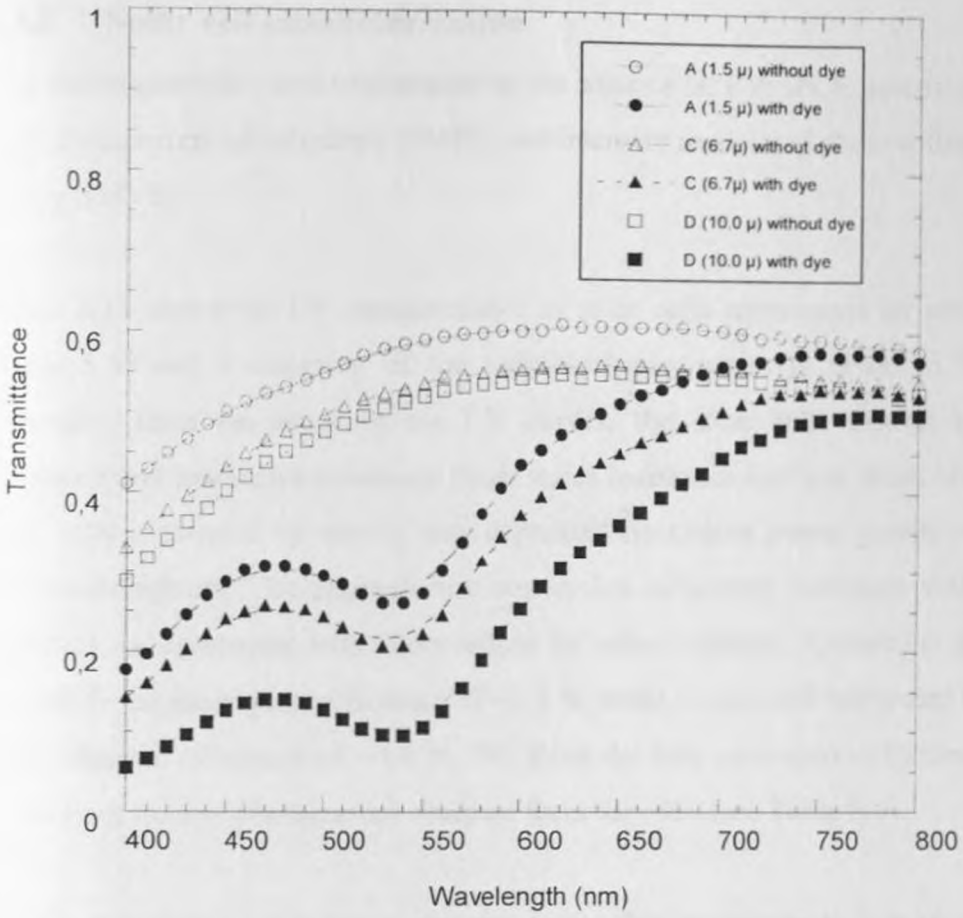

Fig. 5.12. Optical transmittance for bare-no dye (unfilled curves) and dyed (filled curves) titanium dioxide films of various thicknesses.

Table 5.4: The transmittance values of the dyed titanium dioxide films at two different Wavelengths.

Film thickness (μm)	1.5	6.7	10.0
Transmittance (%) at 400 nm	17.7	14.2	5.6
Transmittance (%) at 540 nm	26.1	20.7	9.6

5.3.2 Solar cell characterization

Four techniques were used to characterize the solar cells: I-V, IPCE, intensity modulated photocurrent spectroscopy (IMPS) and intensity modulated photovoltage spectro -scopy (IMVS).

Figure 5.13 shows the I-V characteristics of solar cells represented by samples A-D (Table 5.5) and a summary of the individual parameters is given in Table 5.5. Generally, from the shape of the I-V curves, the solar cells exhibit high shunt resistance and low series resistance (high series resistance and low shunt resistance in solar cells evidenced by curves with depressed maximum power points i.e., curves tend to straighten). The photoelectric conversion efficiency increases with the film thickness, in agreement with observations by other workers [Gomez, *et al*; 2000[a]]. Sample D has the highest efficiency of ~3.3 % while a solar cell fabricated by Gomez (2001) had an efficiency of ~4.4 %. We think the low conversion efficiency mainly stems from the low photocurrent obtained from the cells (see Table 5.5).

DSSCs experience a number of electron losses that contribute to low photoelectron currents thus reduce the overall conversion efficiencies namely: 1) the generated photoelectron from the conduction band of the titanium oxide film may fall back and recombine with the oxidized dye molecules, 2) back reaction of electrons from the back contact to the redox couple, 3) impurities in the film that act as trap-detrap centres for the electrons, and 4) excited dye electrons falling back to recombine with dye holes [Dittrich, 2000; Tennakone, *et al*., 2001; Palomares *et al*., 2003; Peng, *et al*., 2004]. All these mechanisms lead to annihilation of electrons resulting in low photocurrents and low photoelectric conversion efficiencies. However, the dye excitation process is 1000 times faster than the loss of excited dye electrons (through falling back to recombine with dye holes) and therefore loss of electrons by recombining with dye holes can be ignored. Similarly, the electron re-generation at the counter electrode is 100 times faster than the recombination of the oxidized dye molecules with the generated photoelectron from the conduction band of the titanium oxide film thus recombination of the oxidized dye molecules with the generated

photoelectron from the conduction band of the titanium oxide film can be ignored as well [Ferber *et al.* 1998]. To minimize the effect of impurities (process 3), the films were deposited in ultra-high vacuum so that the deposited films would have minimum contamination that act as trap-detrap centres and slow down electron movement. Holes generated in the dye or redox couple may also travel through the titanium dioxide film to the FTO back contact, creating a short circuit. However, even though we did not carry out an independent investigation into this short-circuit problem, we think it may not have been a problem otherwise it would have been evident in the I-V curves-figure 5.14 (by getting straight line graphs or near straight lines). The dominant electron loss may therefore be through process 2 (back transfer of electrons from the back contact to redox couple).

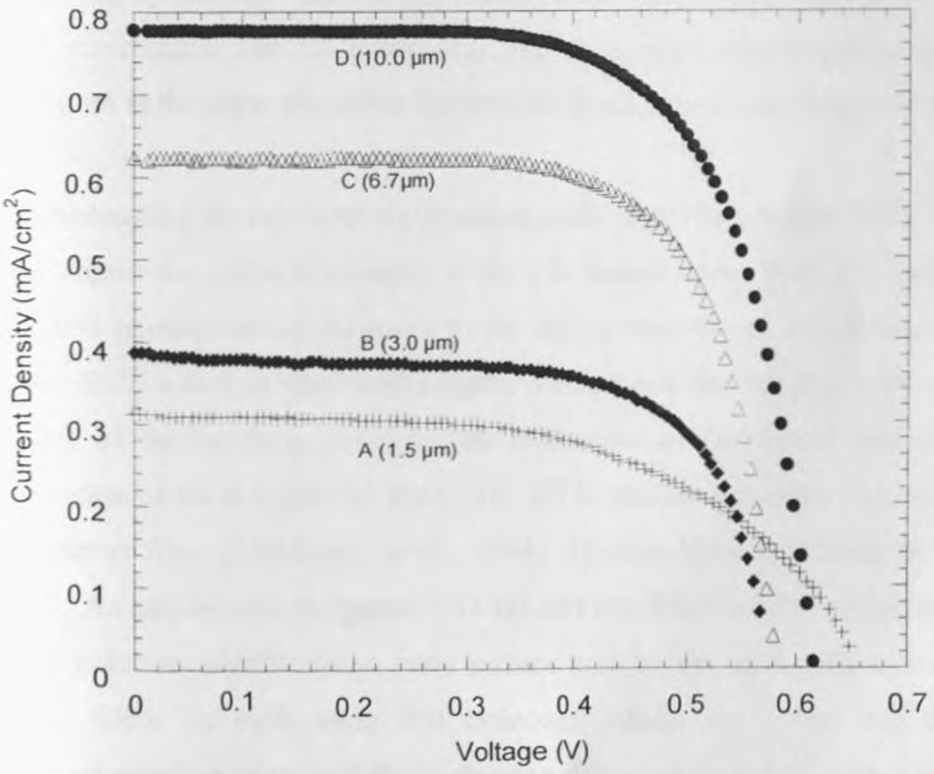

Fig. 5.13. Current-Voltage characteristics for solar cells fabricated from films of different thicknesses. The illumination level was 100 W/m².

Table 5.5. The solar cell parameters for various solar cells at an illumination level of 100 W/m^2. The deposition angle for the TiO_2 films was 60°.

Sample	*Film thickness (μm)*	*V_{oc} (V)*	*J_{sc} (mA/cm^2)*	*Fill Factor, (FF)*	*Efficiency, η (%)*
A	1.5	0.66	0.31	0.55	1.12
B	3.0	0.58	0.39	0.67	1.49
C	6.7	0.58	0.62	0.70	2.56
D	10.0	0.62	0.78	0.68	3.26

The IPCE for the samples A-D is shown in figure 5.14 (a) Front illumination - from the electrolyte side (EE), and (b) back side illumination - from the titanium oxide side (SE). Neither reflection, absorption nor scattering loss corrections were made. The different shapes of the action spectra for the same solar cell in the two figures, (a) and (b) can be explained as follows: When the solar cell is illuminated from the electrolyte side (EE), the electrolyte absorbs part of the radiation contributing to a lower light harvesting by the dye and fewer photoelectrons and hence the low IPCE values at short wavelength. The IPCE however, increases with wavelength increase and is a maximum at the point where the dye absorbs most, i.e., at wavelength ~540 nm.

On illuminating the cell from the titanium oxide side (SE), higher IPCE values at low wavelengths are noted in contrast to the EE illumination. With SE illumination, the absorbed photons excite electrons in the dye giving rise to a photocurrent and thus higher IPCE values at short wavelengths. This shows that the dye is close to the back contact of the working electrode, an indication of the film's porosity and deep penetration of the dye into the films. The IPCE spectra is usually reversed in the case of compact films [Södergren, *et al.*, 1994]. Thicker films contribute to higher IPCE values. As can be seen in figures 5.15 (a) and (b), thicker films are expected to have longer columns which expose more surface area to the sensitizing dye compared to thinner films. As such, more dye molecules adsorb onto them and this leads to increased numbers of excited electrons upon illumination, giving higher photocurrents and higher IPCE.

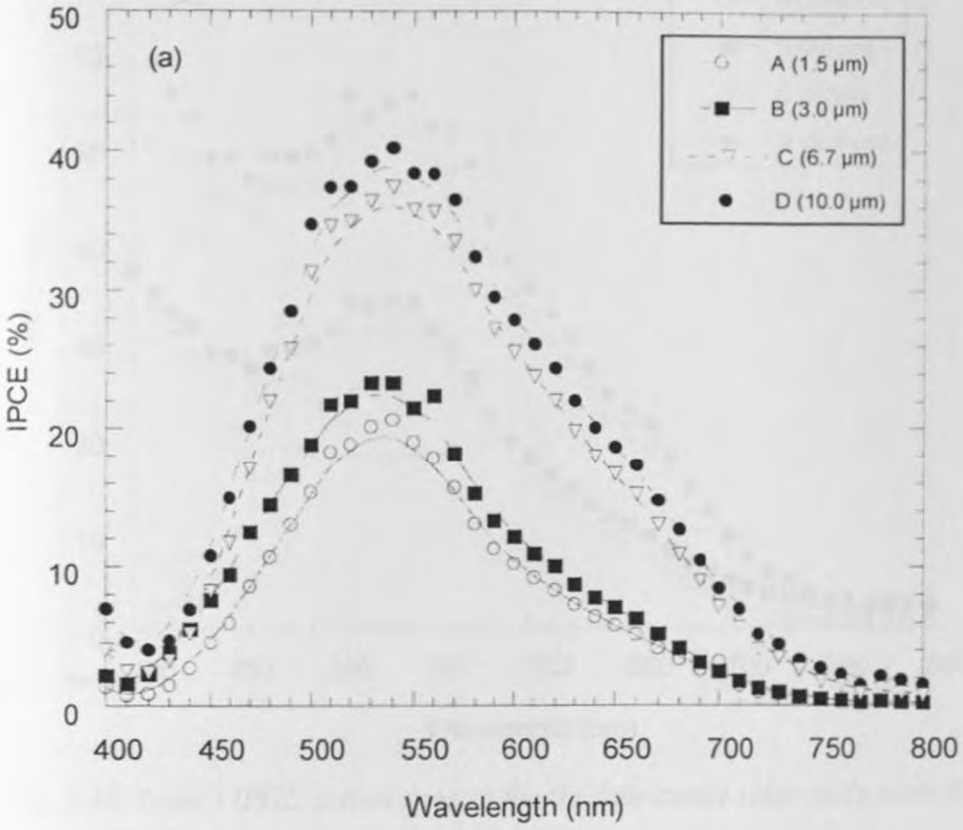

Fig. 5.14. IPCE action spectra for the fabricated solar cells with (a) front (EE) illumination

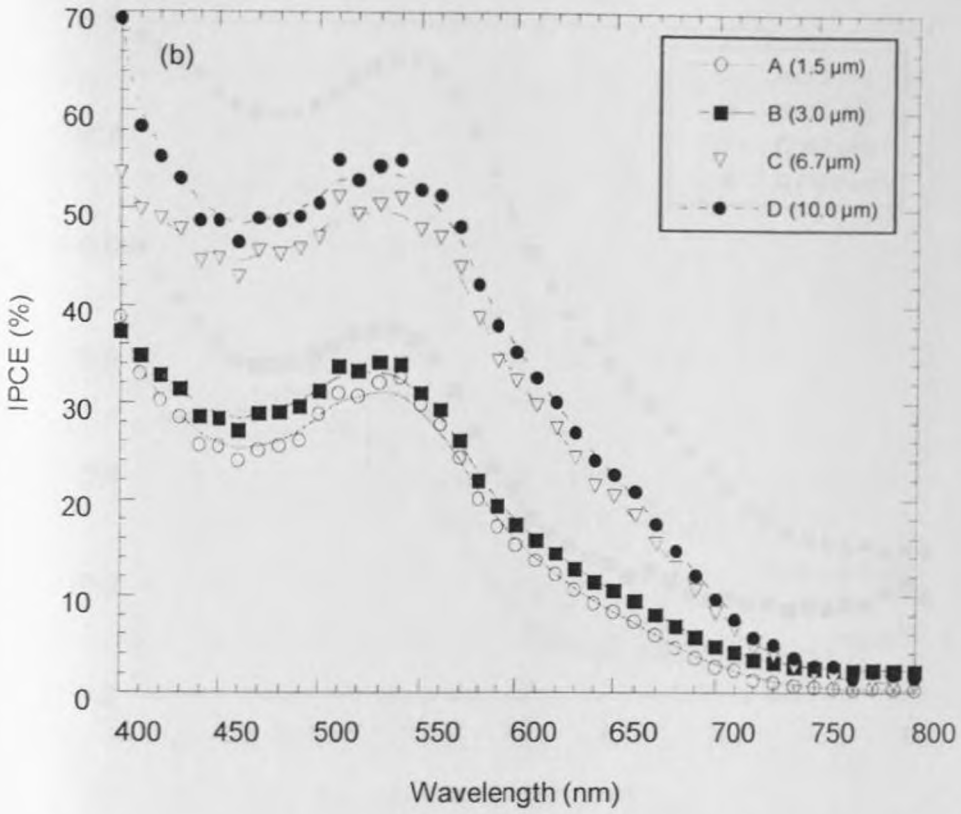

Fig. 5.14. (cont.) IPCE action spectra for the fabricated solar cells with (b) back (SE) illumination.

Figure 5.15 gives the relation between the absorptance and the wavelength for samples. The absorptance gives an idea of the amount of dye adsorbed in the film. Thicker films provide more surface area-to-volume ratio, and therefore have more space, onto which more dye molecules adsorb resulting in higher photon absorptance.

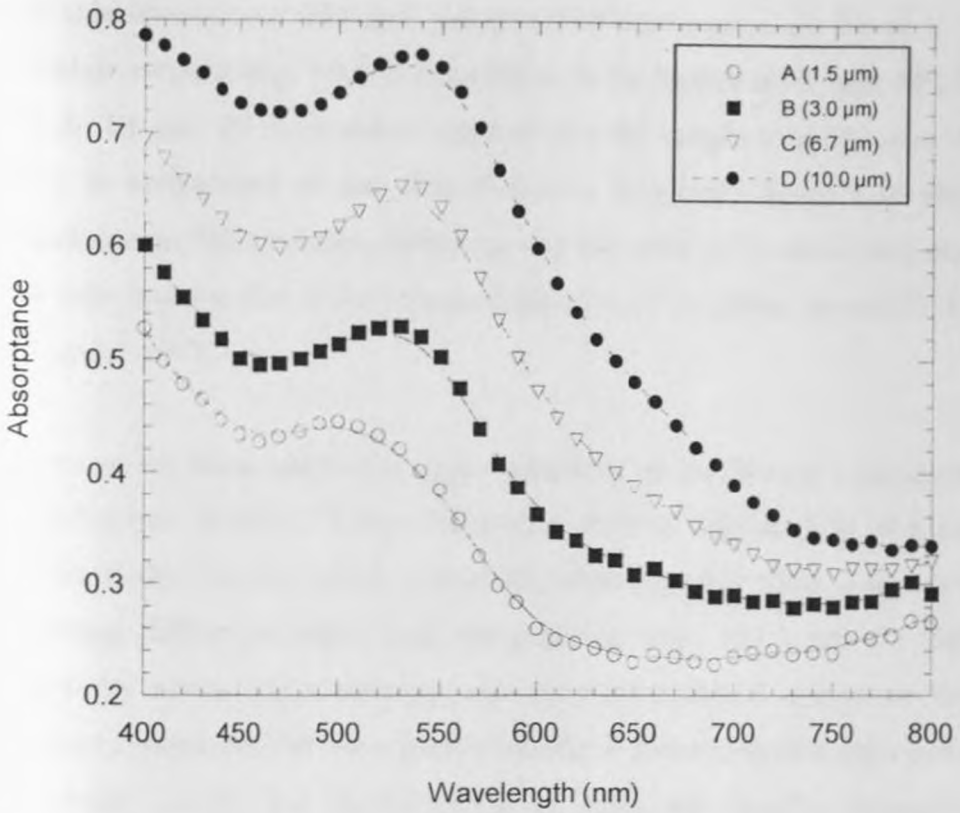

Fig. 5.15. Absorptance spectra for the various solar cells: illumination from back (SE) illumination.

The absorbed-photon conversion efficiency (APCE) gives us information on how efficient the adsorbed photon generates electrons. APCE can be calculated by dividing the IPCE with the LHE [Heimer, *et al.*, 2000; Watson and Meyer, 2005]:

$$APCE = \frac{IPCE(\lambda)}{LHE(\lambda)} = \Phi_{inj} \times \eta_e \qquad (5.1)$$

where Φ_{inj} is the quantum yield of charge injection and η_e is the charge collection efficiency at the back contact.

One would expect the APCE to be independent of both the absorbed dye and the wavelength of the incident photon because it evaluates the efficiency after photon absorption. APCE is an assessment of charge transport in the solar cell. Our results for

front side illumination (EE) and backside (SE) illumination are shown in figure 5.16 (a) and (b) respectively. What is remarkable, in the figures is the high APCE (~0.6 and ~0.8 for EE and SE illumination respectively) for sample C at 540 nm. Ideally, the APCE is independent of the film thickness. However, figure 5.16 shows APCE dependence on film thickness indicating that the solar cell's active area may not have been quite uniform due to the oblique deposition of the films. Sample C (6.7 μm) has the highest APCE.

One reason for this could be the high crystallinity of the films as evidenced by the X-ray diffraction analysis. X-ray diffraction analysis (figure 5.9) showed that the particles in this film had higher crystallinity than the other films; a fact evidenced by the strong diffraction peaks and the particles sizes (27.1 nm for SEM). High crystallinity means more ordering and more symmetrical shapes of the crystals, important components for better charge transfer in nanocrystalline solar cells [Watson, and Meyer, 2005]. The higher APCE at short wavelengths compared to long wavelengths for SE illumination can also be explained [de Jongh and Vanmaekelberg, 1996] as follows: Due to the even distribution of the electrons generated by long wavelengths, they travel longer distances to the back contact in comparison to electrons generated by shorter wavelength. Longer paths may contribute to more trapping and recombination of the electrons as they transverse through the titanium oxide conduction band resulting in lower APCE. Furthermore, in nanocrystalline titanium oxide, there is no space charge field; therefore electron transport in the film is a function of diffusion to the electron concentration gradient [Hagfeldt and Gratzel, 1995]. The long wavelength of the photon is less absorbed and thus creates a smaller electron concentration close to the back contact and this leads to a smaller force for the collection of electrons near the back contact. Slowly moving electrons are likely to be trapped lowering the APCE.

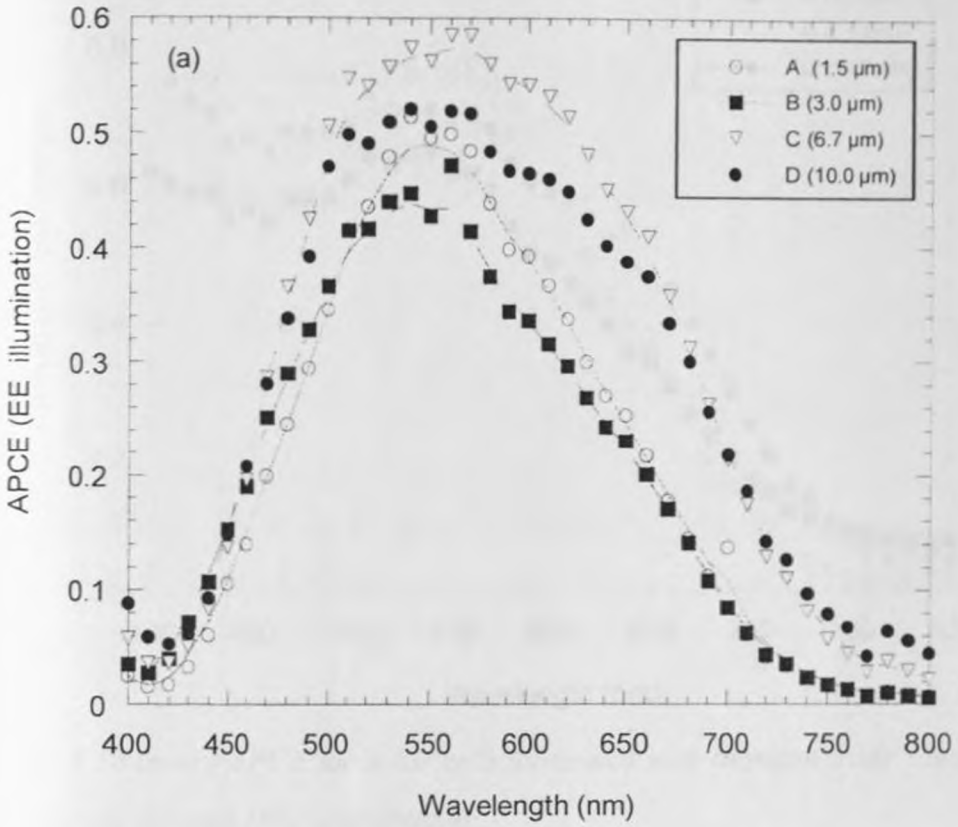

Fig. 5.16 APCE for solar cells fabricated with titanium oxide films of different thickness (a) Front (EE) illumination.

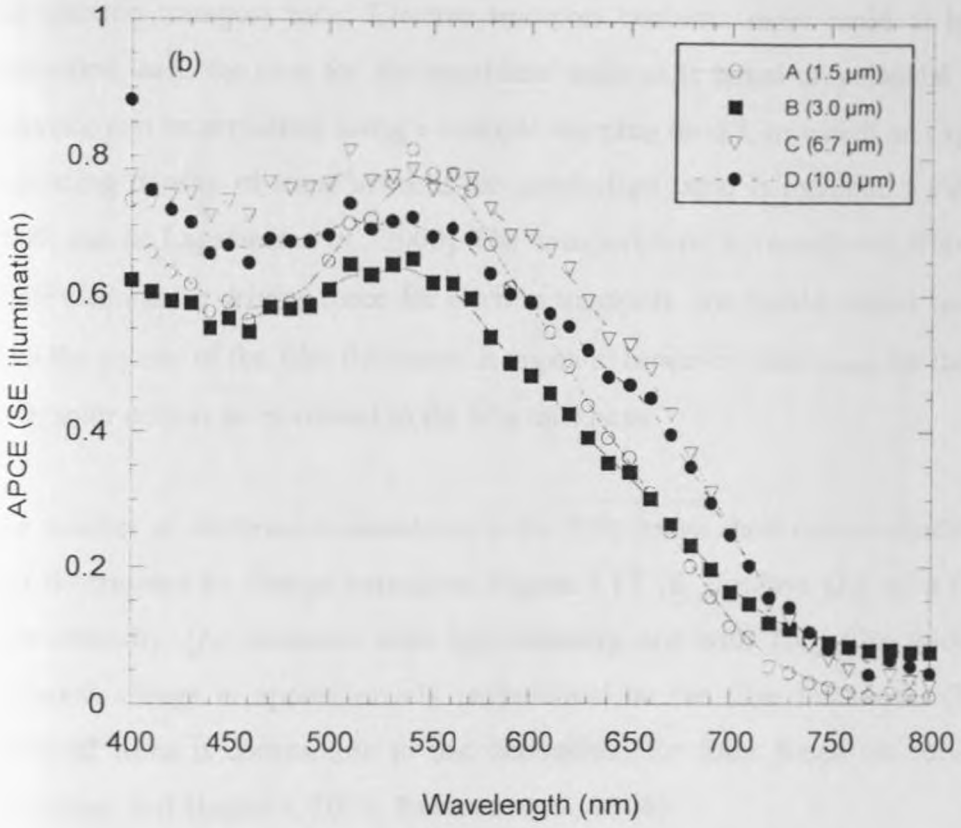

Fig. 5.16 (cont.) APCE for solar cells fabricated with titanium oxide films of different thickness (b) back (SE) illumination.

5.4 Charge transport

Transport of photoinjected electrons in the sputtered TiO_2 films was studied using IMPS at short-circuit conditions. Figure 5.17 (a) shows typical IMPS response for cells with different TiO_2 film thickness in a complex plane plot. The data forms depressed semicircles that increase in radius with increasing TiO_2 film thickness. This is a direct result of the larger photocurrents obtained in thicker films. Figure 5.17 (b) shows the real and imaginary parts of the modulated photocurrent as function of frequency, for one solar cell at different light intensities. It can be seen that the IMPS response shifts toward higher frequencies with increasing light intensities, while the amplitude of the signals remains the same. A single time constant can be extracted from the IMPS data. Figure 5.17 (c) shows the IMPS time constants (τ_{IMPS}) of the 3 cells as a function of light intensity. As will be shown later, τ_{IMPS} can be interpreted as

the electron transport time. Electron transport becomes more rapid at higher light intensities, as is the case for dye-sensitized solar cells based on colloidal TiO_2. This behavior can be explained using a multiple trapping model, in which an exponentially increasing density of traps towards the conduction band is assumed [Fisher *et al.*, 2000; van de Lagemaat *et al.*, 2000]. The transport time increases with film thickness. If diffusion is the driving force for electron transport, one would expect τ_{IMPS} to scale with the square of the film thickness. It appears, however, that τ_{IMPS} for the sputtered TiO_2 solar cells is proportional to the film thickness.

The number of electrons accumulated in the TiO_2 under short circuit conditions (Q_{SC}) was determined by charge extraction. Figure 5.17 (d) displays Q_{SC} as a function of light intensity. Q_{SC} increases with light intensity and with TiO_2 film thickness. The extracted charge is approximately proportional to the film thickness. Q_{SC} for the sputtered films is comparable to that determined for films based on colloidal TiO_2 [Boschloo and Hagfeldt, 2005; Paulsson *et al.*, 2006].

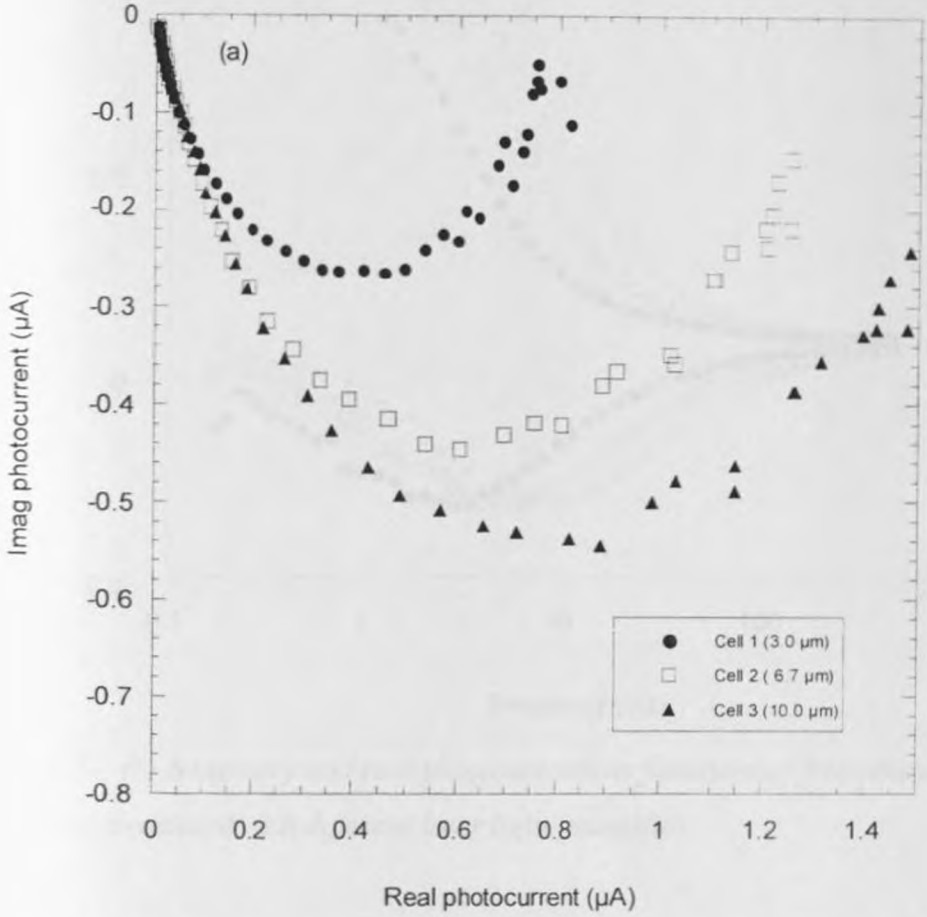

Fig. 5.17. (a) Complex plane plot of the measured IMPS spectra for the different solar cells at an irradiation equivalent to 8.28 W/m^2.

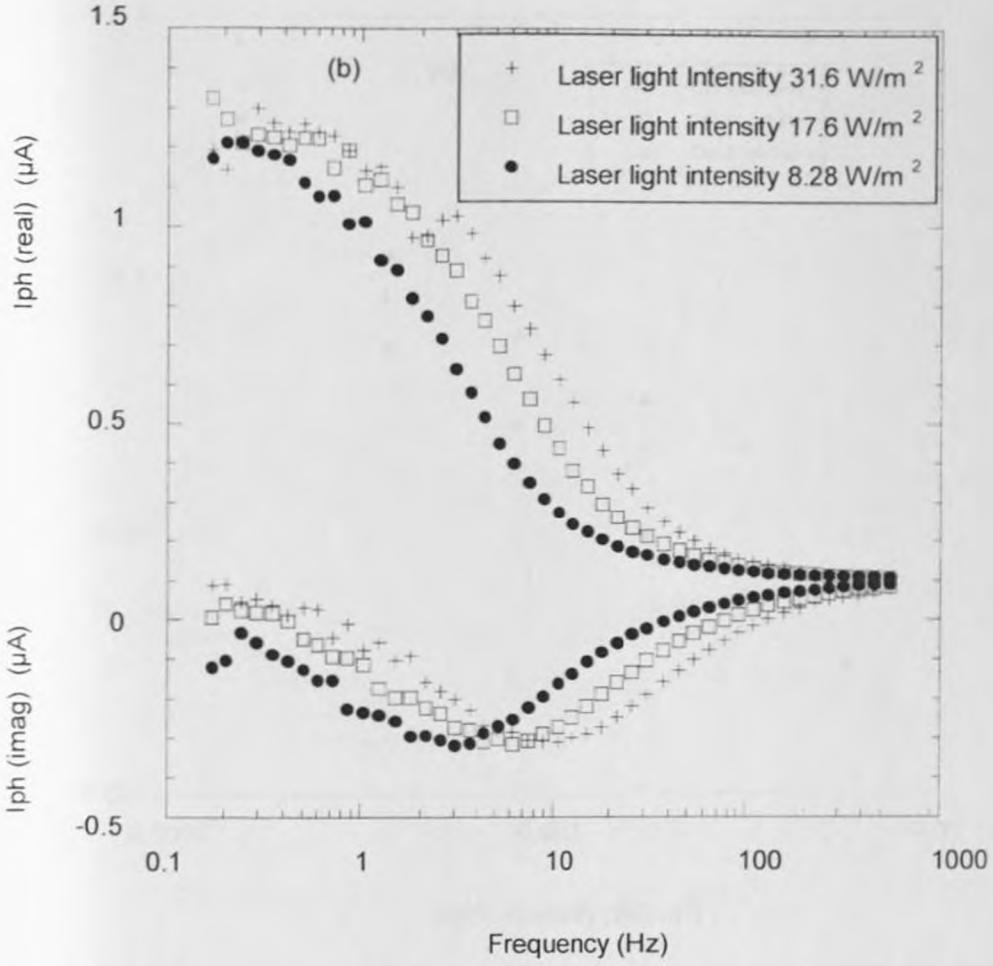

Fig. 5.17. (b) Imaginary and real photocurrents as functions of frequency for cell 2 (6.7 μm) irradiated with different laser light intensities.

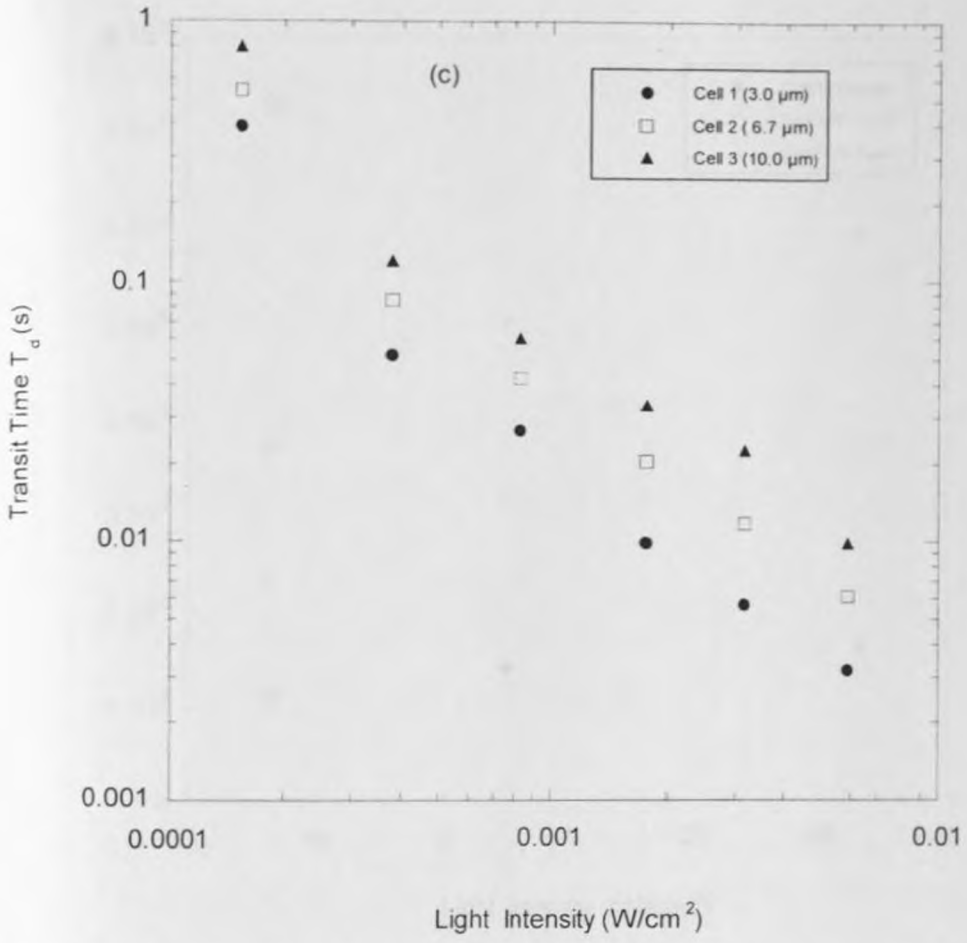

Fig. 5.17. (c) Electron transit time as a function of laser light intensity for all the solar cells.

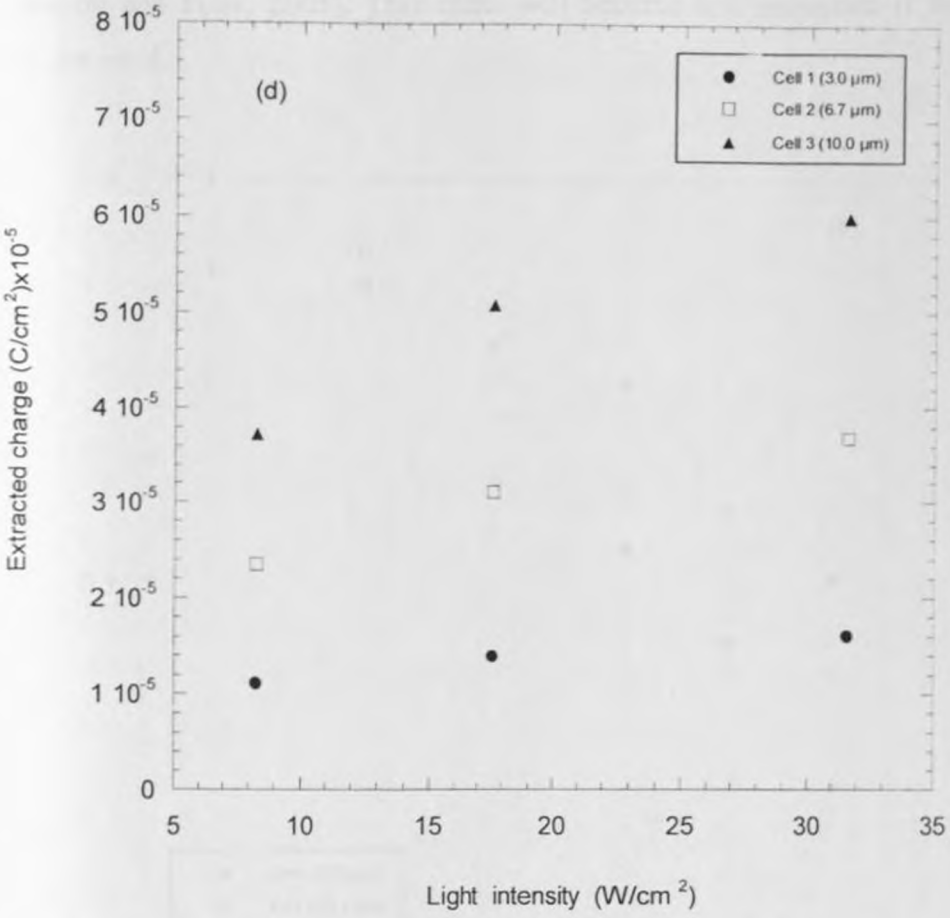

Fig. 5.17. (d) Accumulated charge in the solar cells under short-circuits conditions as a function of laser light intensity.

The lifetime of electrons in the sputtered TiO_2 films was investigated at open circuit conditions using IMVS. IMVS spectra form semicircles in the complex plane, similar to results from dye-sensitized solar cells based on colloidal TiO_2 [Schlichthörl *et. al.*, 1997]. The time constant extracted from the IMVS data corresponds to the electron lifetime τ_e and is shown as a function of light intensity in figure 5.18(a). The electron lifetime is determined by recombination of electrons in the TiO_2 with the oxidized part of the redox couple, I_3^-. τ_e was found to increase with film thickness. Plotting the lifetime against the open circuit potential, figure 5.18(b), it can be seen that at a given voltage thicker films yield longer lifetimes. As the voltage determines the electron concentration in the TiO_2 the change in τ_e is unexpected. A possible explanation is that the FTO substrate contributes to the back transfer of electrons to the redox couple

[Cameron and Peter, 2005]. This effect will become less important if thicker TiO_2 films are used.

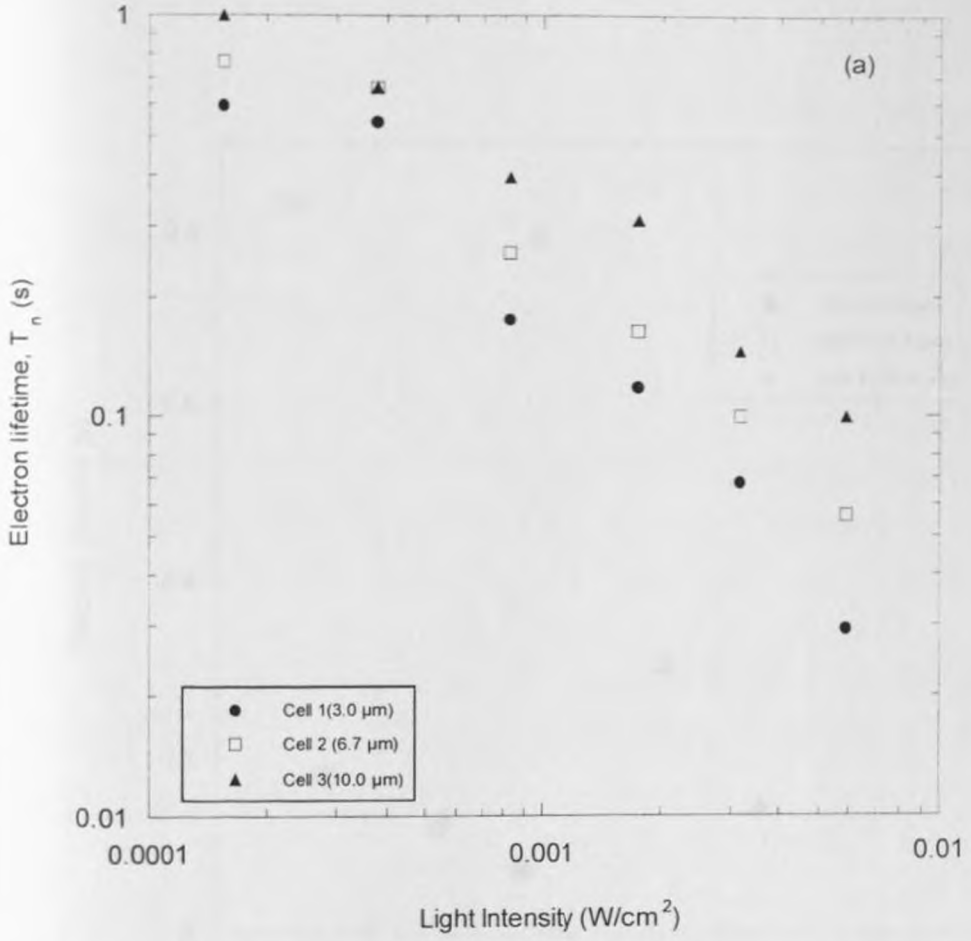

Fig 5.18. (a) Electron lifetime as a function of laser light intensity for all the solar cells.

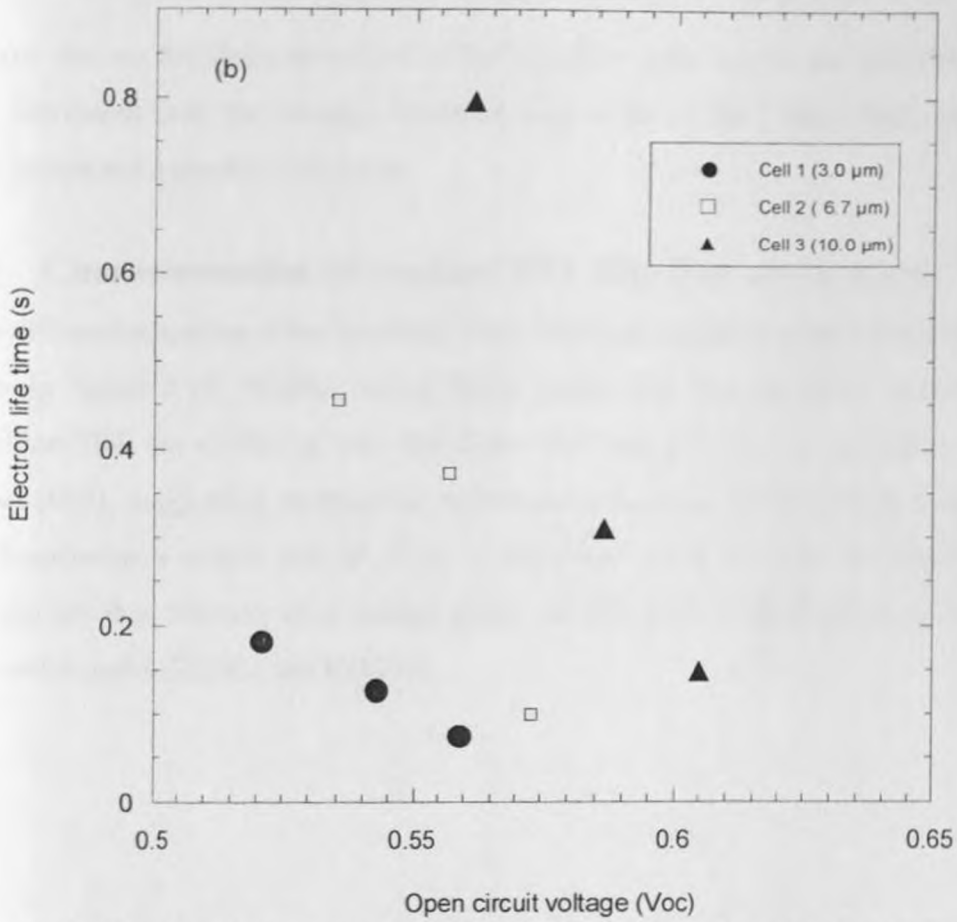

Fig 5.18 (b) Electron lifetime as a function of open circuit voltage for the fabricated solar cells.

It is noted that IMVS times are about one order of magnitude higher than IMPS times at the same light intensities. As the internal potential in the sputtered TiO_2 will be lower under short - circuit conditions than at open circuit, it is clear that the electron lifetime under short - circuit condition will be much longer. Recombination of electrons with the triiodide is therefore negligible under short - circuit conditions. The relatively low short - circuit photocurrents for the sputtered TiO_2 films are therefore

not caused by electron loss through recombination during electron transport. It is therefore likely as mentioned above, that there is back transfer of electrons to the redox couple via the substrate back contact. This observation is in agreement with our earlier analysis (see section 5.2.2).

5.5 Solar cells incorporating compact TiO_2 thin film under layers

We now discuss the characterization of the compact under layers, the thin film solar cells fabricated from the compact layers as well as the as the DSSCs made with the under layers and a porous TiO_2 layer.

5.5.1 Characterization of compact TiO_2 thin film under layers

X-ray diffraction spectra of the sputtered TiO_2 films on conducting glass substrates are shown in figure 5.19. Besides strong SnO_2 peaks from the substrate, peaks from crystalline TiO_2 are visible. In very thin films (~20 nm) only one TiO_2 peak is found: anatase (004), suggesting preferential crystal growth along this direction. From the peak broadening a crystal size of 19 nm is calculated using the Scherrer equation. In films thicker than 100 nm other anatase peaks (A(101) and A(200)) appear, as well as some rutile peaks (R(101) and R(111)).

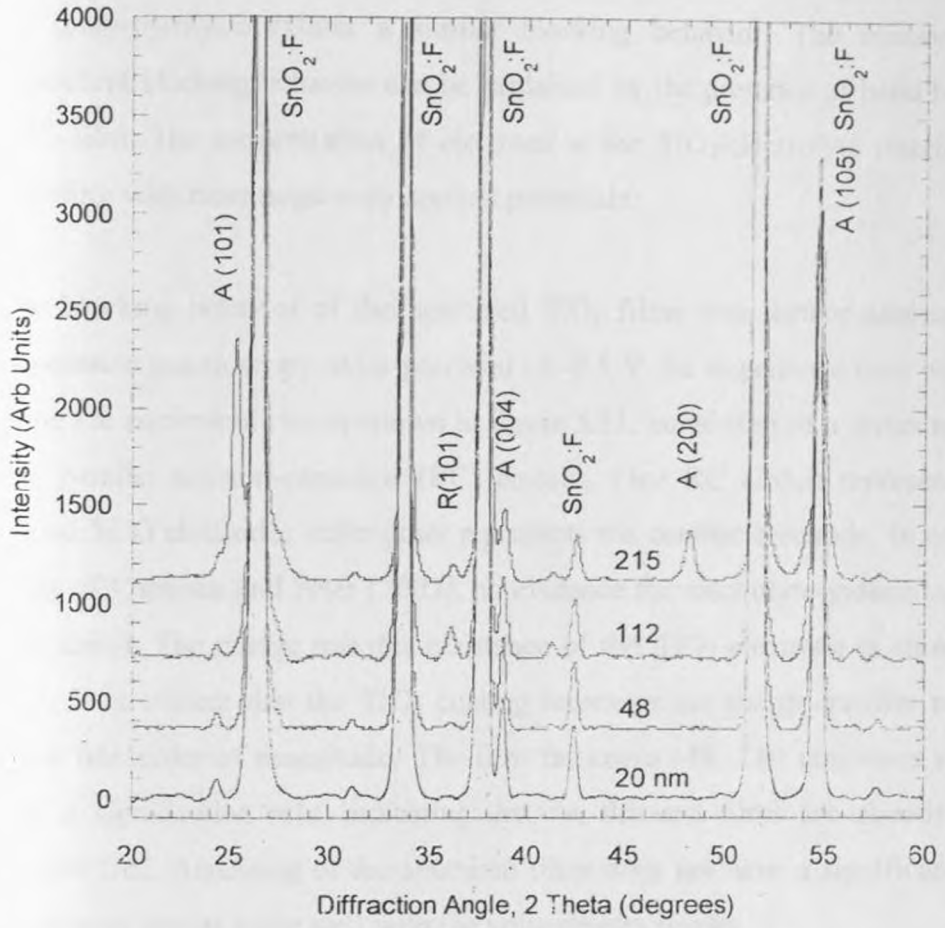

Fig. 5.19. X-ray diffraction spectra of sputtered compact TiO_2 films on FTO glass substrates

5.5.2 Compact TiO_2 thin film solar cells

The I-V characteristics of sputtered TiO_2 films on FTO were recorded in an electrolyte containing the iodide/triiodide redox couple. Typical results in the negative potential range, where the current is due to reduction of triiodide: $I_3^- + 2\ e^- = 3\ I^-$, are shown in Figure 5.20. The presence of a sputtered TiO_2 film decreases the current significantly compared to the bare FTO substrate at potentials in the range of 0 to -0.5 V, but for more negative potentials the difference in current becomes less. Additional annealing

of the sputtered films at 450 °C for 30 min. in air did not have a significant effect. It has been shown by Cameron and Peter [2003, 2005] that blocking TiO_2 films prepared by spray-pyrolysis exhibit a similar blocking behavior. The observed potential-dependent blocking behavior can be explained by the presence of band bending in the TiO_2 film. The concentration of electrons at the TiO_2/electrolyte interface increases therefore with more negatively applied potentials.

The blocking behavior of the sputtered TiO_2 films was further analyzed using ac-impedance spectroscopy. At a potential of -0.5 V the impedance data was well fitted using the equivalent circuit shown in figure 5.21, consisting of a series resistance and two parallel resistor–capacitor (RC) circuits. One RC circuit represents the TiO_2-coated TCO electrode, while other represents the counter electrode. In contrast to the study of Cameron and Peter [2003], no evidence for electrolyte-induced surface states was found. The charge transfer resistance of the TiO_2 electrode is shown in Figure 5.21. It is evident that the TiO_2 coating increases the charge-transfer resistance, by about one order of magnitude. The film thickness (48 -210 nm) does not appear to play a signification role, indicating that the thinnest films are already sufficiently pinhole free. Annealing of the sputtered films does not have a significant effect. The impedance results agree well with the voltammetry results.

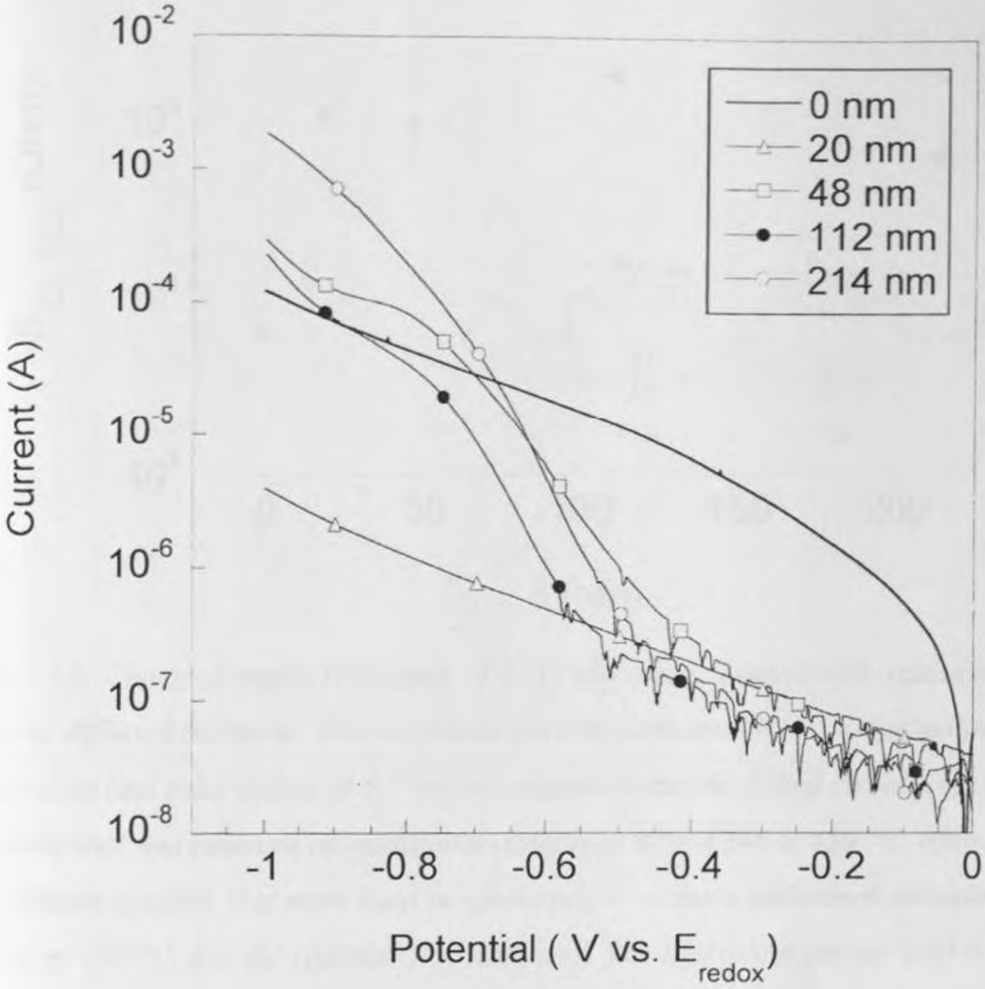

Fig. 5.20. Linear sweep voltammograms of TiO_2 blocking layers on FTO glass substrates. The TiO_2 film thickness is indicated. Sandwich cells were prepared with a FTO + TiO_2 working electrode and platinized FTO. Scan rate 10 mV s^{-1}.

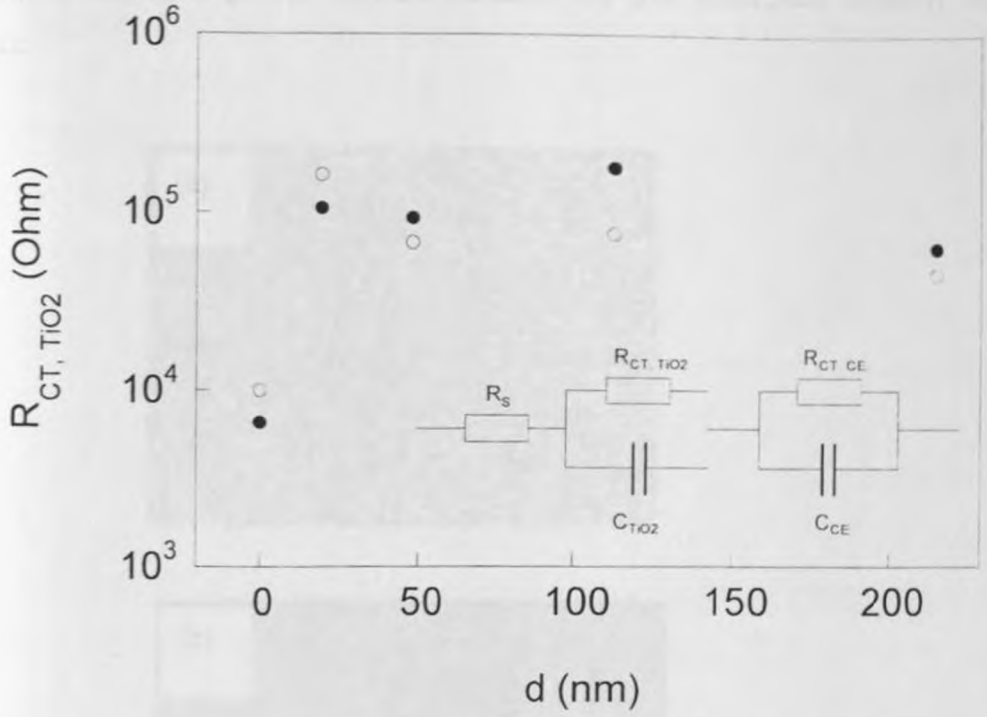

Fig. 5.21. Charge-transfer resistance of FTO electrodes coated with sputtered TiO_2 films of different thickness. The electrodes were in contact with the iodine/iodide redox electrolyte and polarized at -0.5 V vs. the counter electrode. Filled circles (•) indicate samples that had received an additional annealing step in air at 450 °C, open circles (○)indicate samples that were used as sputtered i.e. without additional annealing step in air at 450 °C. d is the compact film thickness. The equivalent circuit used to fit the ac-impedance data is shown.

5.5.3 DSSCs with compact TiO_2 under layers

The SEM images in figure 5.22 show the appearance of the top surfaces of the bare substrate (a), compact underlayer (b) and porous layer on top of an underlayer (c). The FTO bare substrate is rough with clear grain boundaries. The surface assumes a smoother shape when a compact underlayer is deposited as shown in (b). The deposited film occupies the boundaries of the FTO coating (back contact) on making the surface uniform and compact. This compact layer prevents direct contact of the electrolyte with the substrate back contact and therefore blocks electron transfer from the back contact to the electrolyte. A porous layer deposited on the compact

underlayer creates a porous surface increases the dye adsorption capacity of the surface.

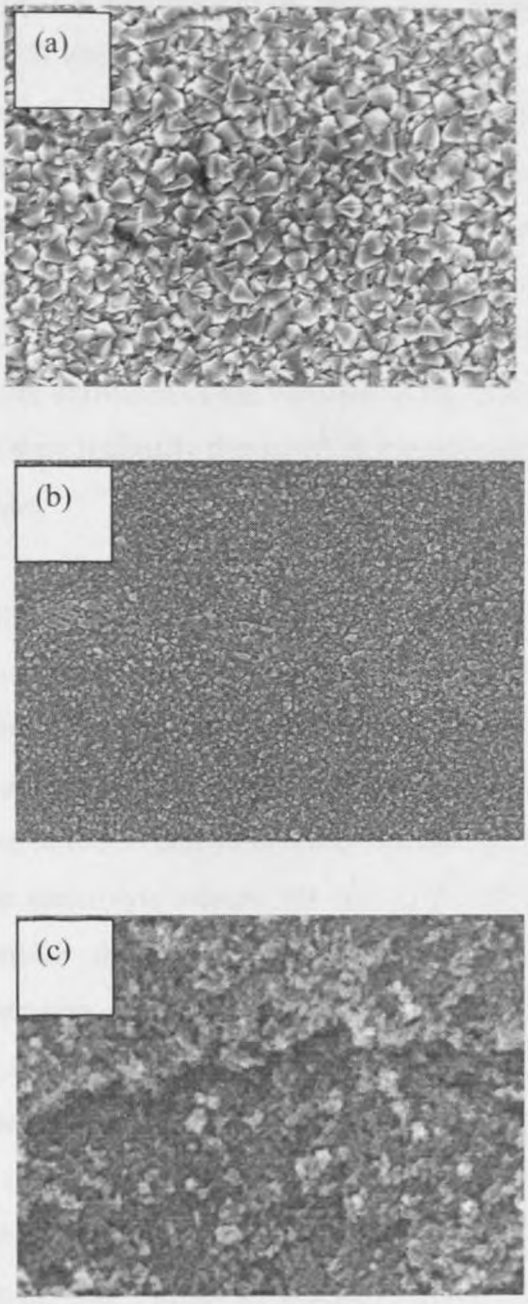

Fig. 5.22. Top-down SEM images for bare FTO 8 substrate (a) sputtered film-105 nm thick (b) and film in (b) after coating a porous layer of TiO_2 by doctor blading (c).

Dye-sensitized solar cells prepared using sputtered blocking underlayers were tested. Typical I-V curves are shown in figure 5.23. Very thin blocking layers (~20 nm) improved the I-V characteristics of the solar cells. More specifically, the fill factor was improved by ~5% while the photoelectric conversion efficiency increased by ~23%. The photocurrent density at shortcircuit point increased by ~15%. A similar effect has been reported for DSSCs with spray-coated TiO_2 underlayers [Hore and Kern, 2005]. This effect can be directly related to the decrease in recombination losses of electron to the electrolyte at the FTO substrate. Blocking layers of 50 nm and thicker, however, decreased the fill factor and thereby the overall solar cell efficiency. Differences in the photocurrent were attributed to the variation in the quality and thickness of the porous TiO_2 films that were manually deposited on top of the blocking layers using the doctor blading technique.

The decay of the open circuit potential of a solar cell in darkness, after a period of illumination, is a useful and easy method to investigate recombination processes in solar cells [Zaban *et al.*, 2003]. In figure 5.24, the voltage decay was significantly slower when a sputtered TiO_2 underlayer was present in the solar cells, indicating that a significant part of the recombination between electrons in the working electrode and triiodide in the electrolyte occurs via the FTO substrate in absence of the TiO_2 underlayer. Similar results have been observed before for spray-coated TiO_2 underlayers [Cameron and Peter, 2003]. The initial voltage decay (around -0.7 V) is, however, not significantly affected. This is agreement with the linear sweep voltammetry measurements (figure 5.20) that show that the blocking behavior of the sputtered TiO_2 underlayers is only apparent at potentials lower than -0.7 V. From the voltage decay transients (figure 5.24) electron lifetimes in the TiO_2 can be calculated using $\tau_e = -kT/e\ (dV/dt)^{-1}$, where kT/e is the thermal energy of electrons [Zaban *et al.*, 2003]. The inset in figure 5.24 shows that the sputtered underlayers improved τ_e by a factor ~2 in the voltage range of -0.6 to -0.3 V.

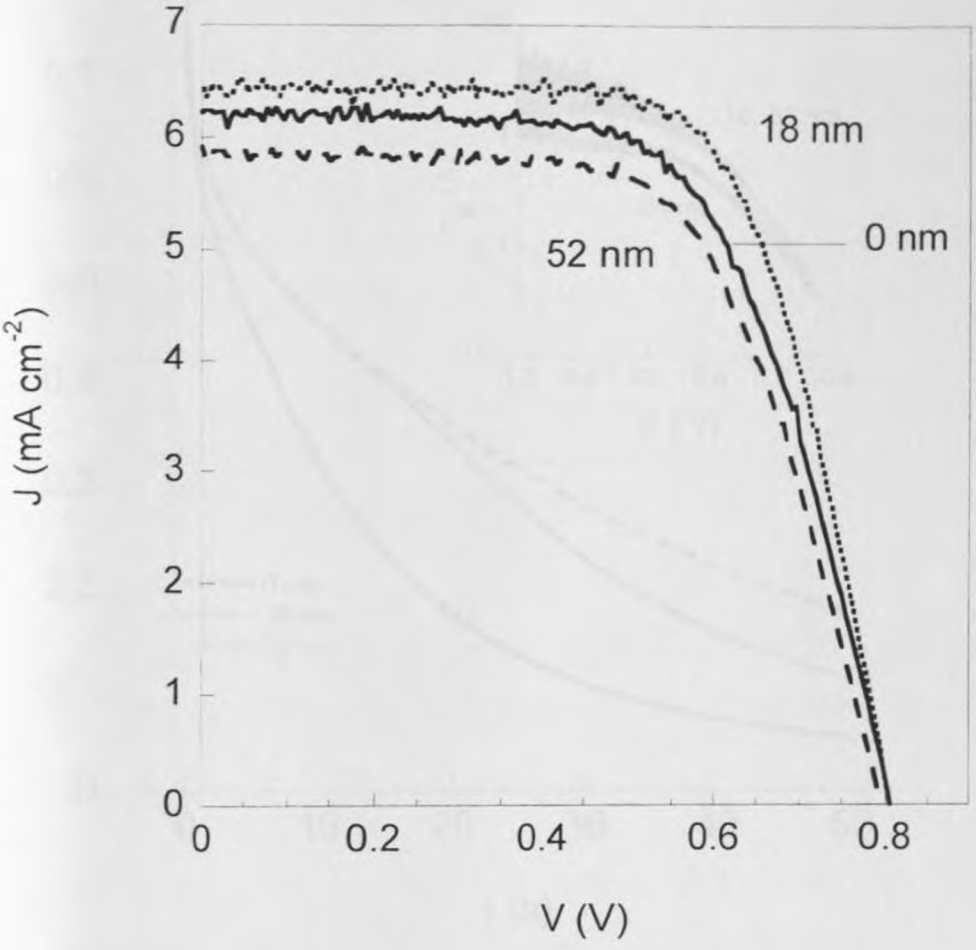

Fig.5.23. I-V characteristics of dye-sensitized solar cells with compact TiO_2 underlayers in simulated sunlight (1000 W m^{-2}, AM 1.5G). Porous TiO_2 films (~8 μm thick) were deposited on top of the sputtered underlayers.

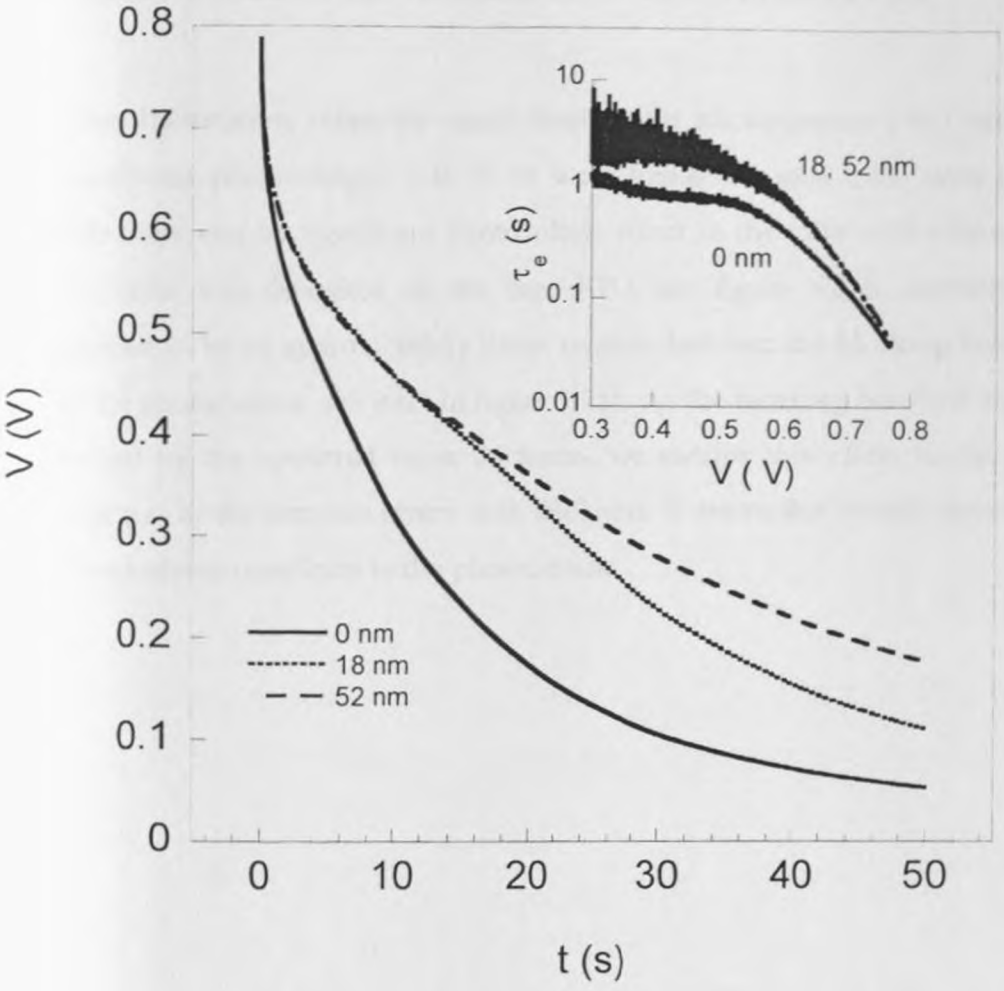

Fig. 5.24. Open-circuit voltage decay transients of dye-sensitized solar cells with compact TiO_2 underlayers. Inset shows the calculated lifetimes vs. voltage.

Finally, dye-sensitized solar cells with sputtered TiO_2 underlayers were tested using a fast one-electron redox couple: ferrocene / ferrocenium. I-V characteristics in the dark and upon illumination are shown in figure 5.25. At over potentials less than 100 mV, the anodic and cathodic dark currents were decreased by the sputtered blocking layer by ~2 orders of magnitude compared to solar cells without underlayers on the FTO. Currents were, however, ~2 orders of magnitude larger than in the case of the iodide /

triiodide electrolyte, because of the much faster kinetics of the ferrocene-based redox couple. The thickness of the blocking layers (18 – 320 nm) did not have a significant effect on the measured dark currents as can be seen in figure 5.25 (a).

Under illumination, relatively small short circuit photocurrents (~0.1 mA cm^{-2}) and open-circuit photovoltages (~0.15 V) were found for solar cells with underlayers, while there was no significant photovoltaic effect in the solar cells where the porous TiO_2 layer was deposited on the bare FTO, see figure 5.25b. Interestingly, there appeared to be an approximately linear relation between the blocking layer thickness and the photocurrent, see inset in figure 5.25b. As the blocking behavior was not much affected by the sputtered layer thickness, we ascribe this effect to the increase in roughness of the compact layers with thickness. It seems that mainly dyes attached on the underlayer contribute to the photocurrent.

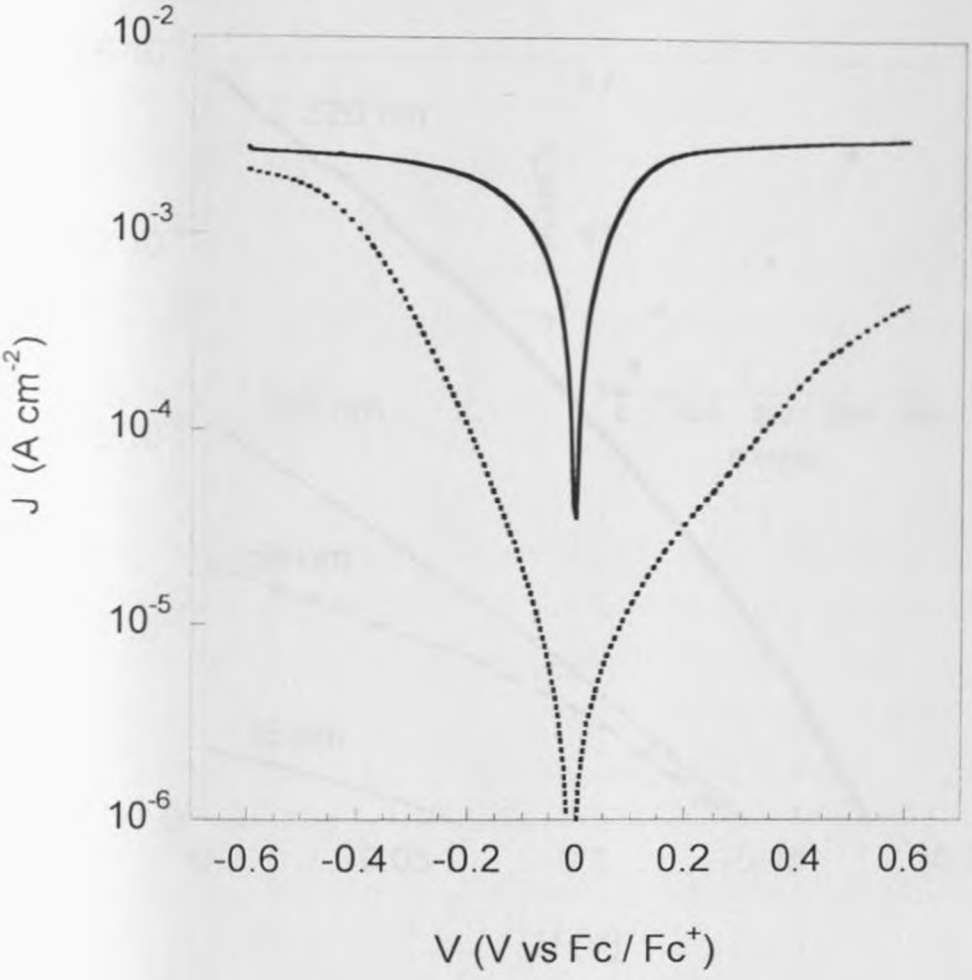

Fig. 5.25(a). I-V characteristics of dye-sensitized solar cells with and without compact TiO_2 underlayers in ferrocene/ferrocenium electrolyte in darkness (1) without underlayer (full line) and (2) with 18 nm thick underlayer (dotted line): Porous TiO_2 films (~2 μm thick) were deposited on top of the sputtered underlayers.

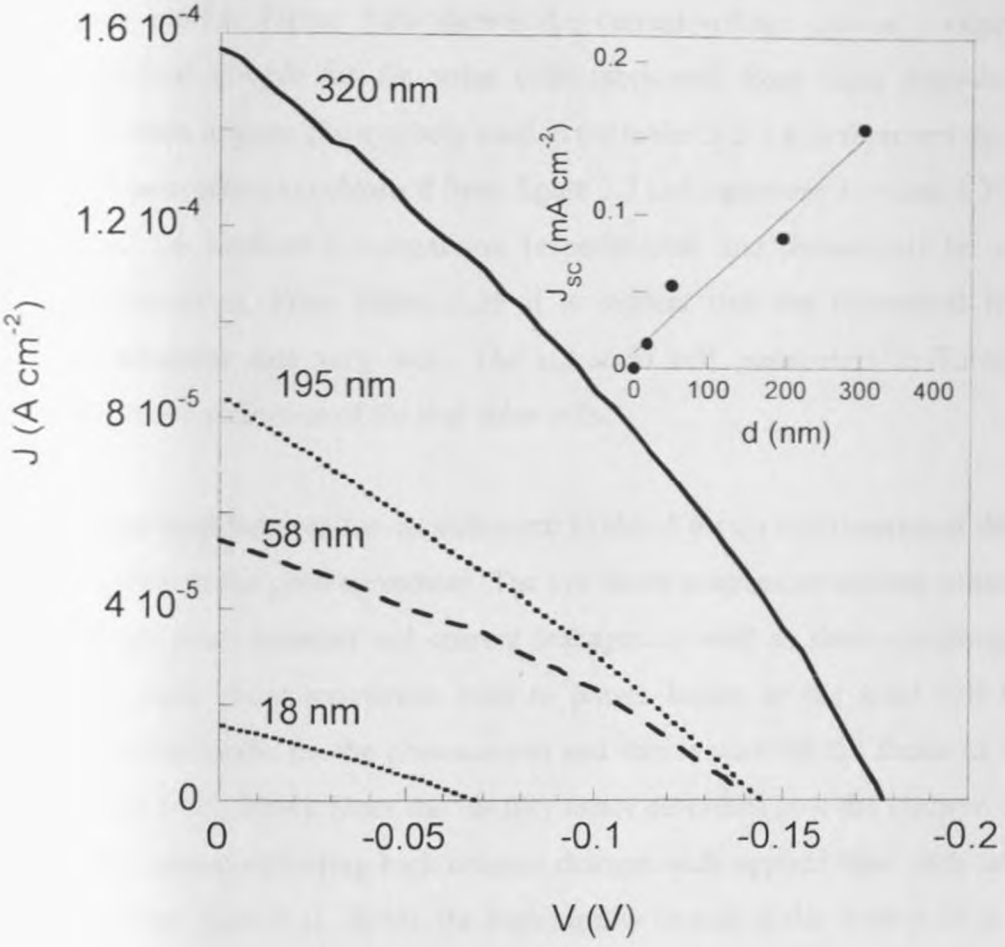

Fig. 5.25(b). I-V characteristics of dye-sensitized solar cells with compact TiO_2 underlayers in ferrocene/ferrocenium electrolyte under illumination (1000 W m^{-2}, AM 1.5G). Porous TiO_2 films (~2 μm thick) were deposited on top of the sputtered underlayers. The inset shows the short-circuit photocurrent as function of TiO_2 underlayer thickness.

5.6 Model fitting

The current-voltage experimental data obtained in our work was fitted with the single diode model. Figure 5.26 shows the current-voltage curves - experimental and theoretical (fitted) for the solar cells fabricated from films deposited at various deposition angles. The symbols used in the tables 5.6-5.8 to represent the various solar cells parameters are obtained from figure 3.7 and equations 3.14 and 3.29 in chapter 3. Table 5.6 outlines a comparison (experimental and theoretical) for the solar cell characteristics. From figure 5.26 it is evident that the theoretical fits match the experimental data very well. The extracted cell parameters in Table 5.6 (b) are therefore a reflection of the real solar cells.

Comparison between the experimental (Table 5.6 (a)) and theoretical data (Table 5.6 (b)) show some good agreement. The low shunt resistances indicate some electron loss through recombination and current leakages as well as short circuiting in the solar cells. Low shunt resistances lead to power losses in the solar cell by providing alternative paths for the photocurrent and this lowers the fill factor of the solar cell [Koide et al., 2006]. Since the ideality factor describes how the electron concentration at the current-collecting back contact changes with applied bias with unity being the ideal case [Lee et al., 2004], the high ideality factors of the solar cells is an indication of high concentration of electrons at the back contact. This suggests that the electron collection to the external circuit is not efficient. When electrons easily find a shorter route to the external circuit then this is called short - circuiting. The low series resistance in our results suggests short circuiting. Poor cell fabrication is therefore the most probable reason for the poor performance of the solar cells.

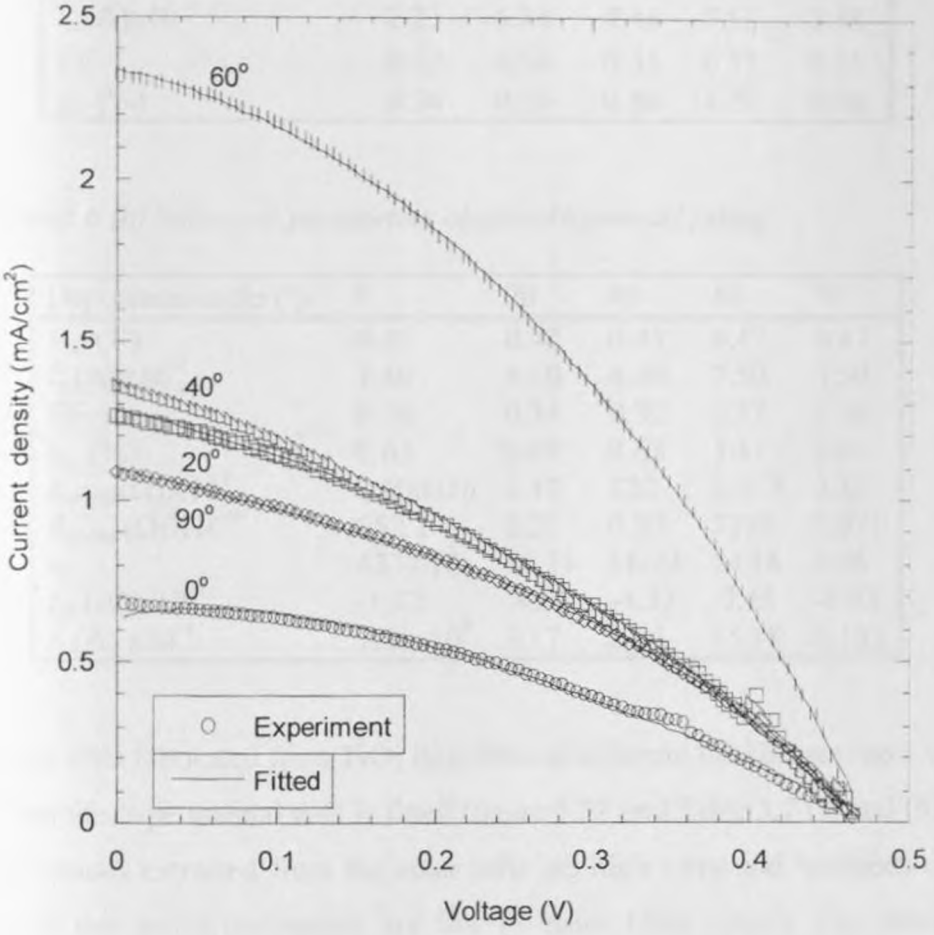

Fig. 5.26. Fitted and experimental current-voltage curves for DSSC's fabricated from TiO_2 films deposited at different deposition angles.

Table 5.6 (a) Solar cell parameters obtained experimentally Irradiance: 30 mW/cm^2; Temperature 250 °C; Cell active area 0.32 cm^2.

Deposition angle (°)	0	20	40	60	90
V_{oc} (V)	0.42	0.40	0.42	0.45	0.43
I_{sc}(A)x10^{-4}	2.23	4.14	4.41	7.51	3.58
FF	0.37	0.34	0.31	0.37	0.35
η_{ce} (%)	0.36	0.58	0.60	1.29	0.56

Table5.6 (b) Solar cell parameters obtained by model fitting

Deposition angle (°)	0	20	40	60	90
V_{oc} (V)	0.47	0.47	0.47	0.47	0.47
I_{sc}(A)x10^{-4}	3.50	4.10	4.40	7.50	3.50
FF	0.36	0.34	0.32	0.37	0.36
η_{ce} (%)	0.63	0.69	0.68	1.37	0.63
R_{shunt} (Ω)X10^3	0.000016	3.17	122	0.477	3.35
R_{series} (Ω)X10^{-9}	652.2	2.27	0.25	7299	2.07
n_{if}	4337.10	18.13	18.23	24.16	5.96
I_{ph} (A) x10^{-4}	-1.12	-4.08	-4.37	-7.45	-3.52
I_o (A) x10^{-4}	7.51x10^9	3.17	2.54	15.18	0.103

Solar cells fabricated from TiO_2 thin films of different thicknesses show very good fits when the experimental data is fitted (figure 5.27 and Table 5.7 (a) and (b)). The shunt resistances extracted from the solar cells are high (tens and hundreds of kilo ohms) while the series resistances are low (< nano Ohm range). The shunt resistances obtained are not infinite as would be the case with ideal solar cells. This suggests the possibility of cell internal leakages that reduce the efficiency of the solar cells. There is also a significant loss of electrons indicated by the values of the ideality factors.

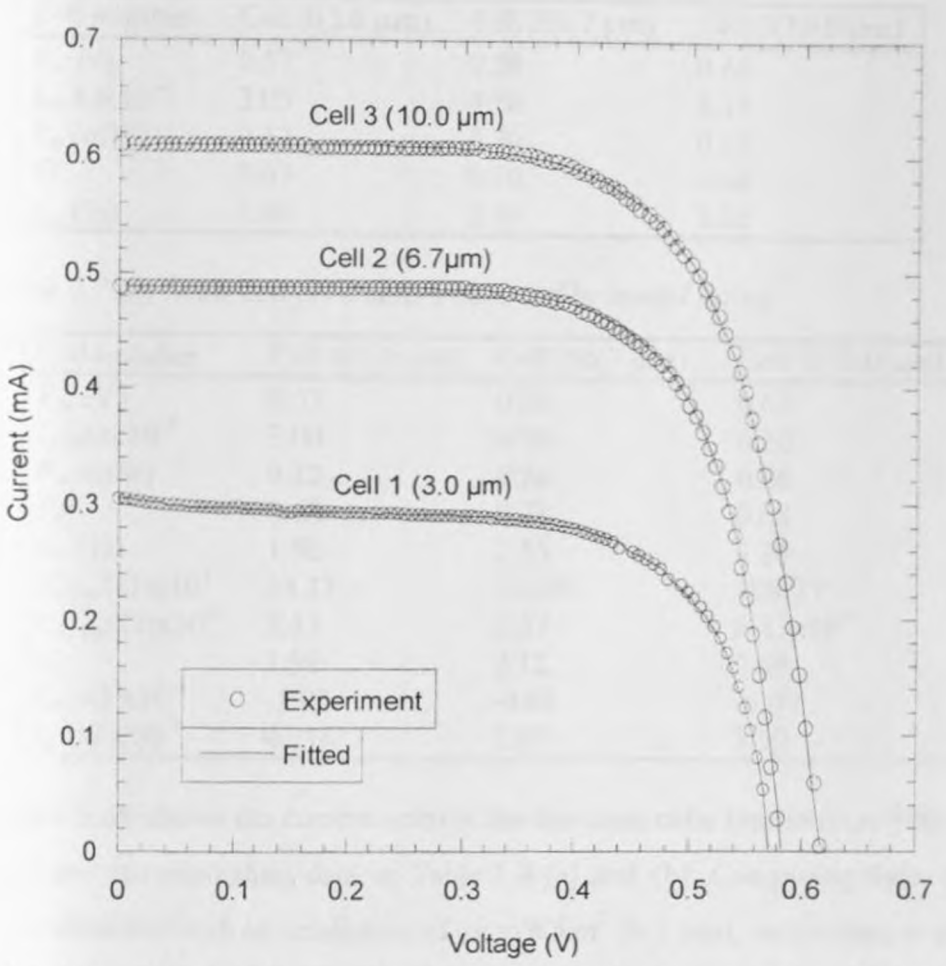

Fig. 5.27. Fitted and experimental current-voltage curves for DSSC's fabricated from TiO_2 films deposited at different thicknesses Irradiation: 10 mW/cm^2 (0.1 sun).

It is seen that the thicker the film solar cell, the higher the ideality factor. This is due to the increased path length of the electrons to the back contact as the film gets thicker. As a result, chances of electron annihilation through electron traps are enhanced reducing the photoelectric conversion efficiency [Ferber and Luther, 1998].

Table 5.7(a) Solar cell parameters obtained experimentally Irradiance:10 mW/cm^2;Temperature 25 °C; Cell active area 0.785 cm^2.

Cell number	Cell 1(3.0 μm)	Cell 2(6.7 μm)	Cell 3(10.0 μm)
V_{oc} (v)	0.57	0.58	0.62
I_{sc}(A)x10^{-4}	3.05	4.88	6.11
P_m (mW)	0.12	0.20	0.25
FF	0.67	0.70	0.68
η_{ce} (%)	1.49	2.56	3.26

Table 5.7 (b) Solar cell parameters obtained by model fitting

Cell number	Cell 1(3.0 μm)	Cell 2(6.7 μm)	Cell 3(10.0 μm)
V_{oc} (V)	0.57	0.58	0.62
I_{sc}(A)x10^{-4}	3.00	4.90	6.10
P_m (mW)	0.12	0.20	0.26
FF	0.68	0.71	0.68
η_{ce} (%)	1.50	2.55	3.26
R_{shunt} (Ω)x10^3	24.13	533.96	108.77
R_{series} (Ω)x10^{-9}	3.13	2.27	6.33x10^{-4}
n_{if}	1.91	2.12	2.58
I_{ph} (A) x10^{-4}	-3.02	-4.88	-6.09
I_o (A) x10^{-8}	0.216	1.09	5.59

Figure 5.28 shows the current-voltage for the solar cells irradiated at 100 mW/cm^2 (1 sun) and corresponding data in Table 5.8 (a) and (b). Comparing these results with those obtained with an irradiation of 10 mW/cm^2 (0.1 sun). an increase in photocurrent and open circuit voltage is observed on irradiating at 1 sun.

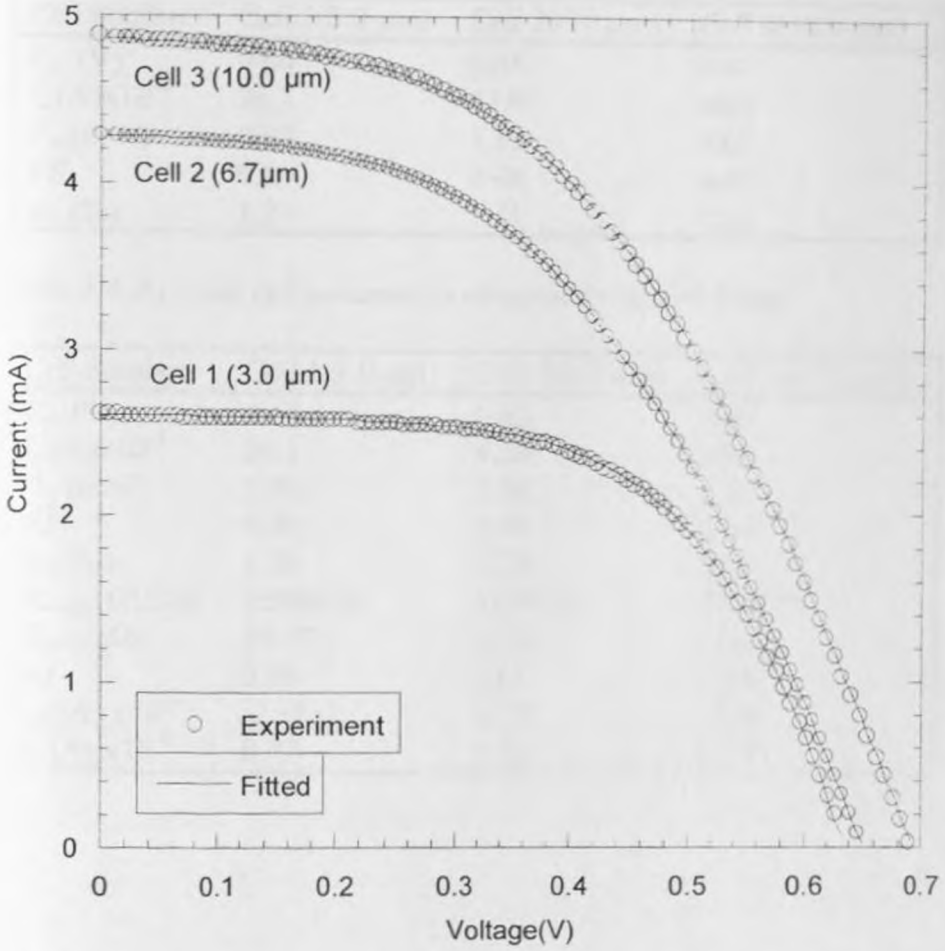

Fig.5.28. Fitted and experimental current-voltage curves for DSSC's fabricated from TiO_2 films deposited at different thicknesses: Irradiation: 100 mW/cm^2 (1 sun).

On the contrary, the fill factor drops as well as the efficiency of the solar cells. The shunt resistance reduces but the series resistance and ideality factor increases significantly. These observations suggest that increased irradiation affects the solar cell in some interesting ways. At low illumination, electrons fill the deep traps. As the irradiation is increased, the electrons gain more energy and jump into shallow traps. This creates more electron loss leading to increased shunt resistance and higher ideality factors. This creates increased series resistance. The fill factor and hence the efficiency of the solar cell reduces.

Table 5.8 (a) Solar cell parameters obtained experimentally. Irradiance:100 mW/cm^2;Temperature 250 ^{o}C; Cell active area 0.785 cm^2.

Cell number	Cell 1(3.0 μm)	Cell 2(6.7 μm)	Cell 3(10.0 μm)
V_{oc} (V)	0.64	0.65	0.69
I_{sc}(A)x10^{-4}	26.3	42.9	48.7
P_m (mW)	0.99	1.35	1.62
FF	0.59	0.48	0.48
η_{ce} (%)	1.27	1.71	2.06

Table 5.8 (b) Solar cell parameters obtained by model fitting

Cell number	Cell 1(3.0 μm)	Cell 2(6.7 μm)	Cell 3(10.0 μm)
V_{oc} (V)	0.63	0.65	0.69
I_{sc}(A)x10^{-4}	26.1	42.8	48.6
P_m (mW)	1.00	1.34	1.62
FF	0.59	0.48	0.48
η_{ce} (%)	1.26	1.70	2.05
R_{shunt} (Ω)X10^3	10086.14	11942.15	8229.78
R_{series} (Ω)	19.97	38.35	36.05
n_{if}	2.08	3.11	3.28
I_{ph} (A) x10^{-3}	-2.62	-4.31	-4.89
I_o (A) x10^{-6}	0.37	1.22	1.29

CHAPTER 6

CONCLUSIONS AND SUGGESTIONS FOR FURTHER WORK

6.1 Conclusions

TiO_2 thin films deposited obliquely by direct current magnetron sputtering as well as dye sensitized solar cells fabricated from the films have been studied. The films were crystalline and had columnar micro structure, rough surfaces and were porous. The porosity of the films increased with deposition angle. The photoelectric conversion efficiency was highest at ~1.3 % for the solar cell fabricated with a TiO_2 thin film deposited at 60^o while the IPCE for the same solar cell was ~28 %.

The role of film thickness on the IPCE and photovoltaic current-voltage (I-V) characteristics of dye sensitised solar cells fabricated from obliquely deposited titanium dioxide thin films was also investigated. The photoelectrochemical and photovoltaic properties were found to depend on the film thickness. DSSCs fabricated from thicker films were found to give higher IPCE and photoelectric conversion efficiencies. The thickest film (~10 μm) gave the highest photoelectric conversion efficiency of ~3.3 %.

Electron transport and lifetime studies carried out on DSSCs made from films of different thicknesses showed that both the electron transport (transit) time and lifetime decreased with increase in light intensity. These transport properties were due to increased density of traps towards the semiconductor conduction band. Further studies showed that the electron transport time as well as electron life time increased with film thickness. This observation is attributed to the presence of grain boundaries with associated trap and / or energy barriers in the films. The observed electron transit and life times for the solar cells ranged a few milliseconds to several hundreds of milliseconds depending on the light intensity and thickness of semiconducting thin film making the solar cell.

Experimental data for dye sensitized solar cells fabricated from crystalline TiO_2 thin films deposited obliquely by reactive DC magnetron sputtering at various deposition angles and at an optimized deposition angle of 60° but with varying film thicknesses was fitted into the one-diode equivalent circuit model in order to obtain the solar cell parameters. For solar cells fabricated from thin films sputtered at varying deposition angles, significant electron loss through recombination, internal circuit leakage and shorting was noted. The solar cells had series resistances of $\sim 10^{-9}$ Ω, shunt resistances of $\sim 10^{2}$ -10^{3} Ω, dark currents of $\sim 10^{-3}$ -10^{-4} A and high ideality factors ~ 6 – 4337. An ideal solar cell should have zero series resistance, infinite shunt resistance and an ideality factor of one. The obtained solar cell resistances, dark currents and ideality factors differ from the ideal values of a solar cell and this was attributed to non-optimized solar cell design. Solar cells fabricated from TiO_2 films of varying thicknesses but at the optimized angle of 60° gave better performance due to both the increase in film thickness and the improved fabrication of the solar cells (sealing) with series resistance in the ~ 20 - 36 Ω range, shunt resistances ~ $8x10^{6}$ - $12x10^{6}$ Ω, dark currents ~ $0.4x10^{-6}$ – $1.3x10^{-6}$ A and ideality factors ~ 2.1 – 3.3). Increasing the light intensity for solar cells with varying film thickness lowers the conversion efficiency due to electron loss through traps.

TiO_2 blocking underlayers prepared by reactive sputtering have a small and subtle effect in dye-sensitized solar cells with iodide/iodine redox couple, where thin layers (~20 nm) appear to improve the fill factor without affecting other properties of the cell. In case of the Fc/Fc+ electrolyte only DSSCs that had underlayers were found to function.

6.2 Suggestions for further work

We have done some studies on obliquely sputtered TiO_2 thin films and applied the same to dye sensitized solar cell studies. We believe by characterizing these films and cells, we have provided some background information for further study in this area or research. Due to the technique of film deposition, the film thicknesses tend to vary along the direction of the sputter beam and this is one of the mainchallenge to overcome before thin films deposited by this technique could be fully accepted as potential candidates for DSSC photoelectrodes. However, the following maybe considered for future work:

- In our work, we used dyes that were readily available. It might be good to try different dyes including solid dyes for the solar cells and see if there are any differences in the cell performance.

- Blocking layers with sputtered porous films should be attempted for DSSCs and a comparison made with DSSCs fabricated from blocking layers with doctor bladed porous films.

- The relation between deposition angle and the angle made by the film column with respect to the substrate normal should be studied for sputtered films and even films deposited by other techniques like evaporation.

APPENDIX

The Orthogonal Distance Regression (ODR) is a method of fitting experimental data when there is noise in the measurements of both the current and voltage. If we let the noise levels in the current and voltage be designated by $\sigma(I)$ and $\sigma(V)$ respectively while the fitted values are designated by V_i^* for the voltage and I_i^* for the current, then the ODR method fits the data by getting the minimum sum of the equation:

$$\min V_i^*, I_i^* \sqrt{\left\{\frac{1}{N}\sum_{i=1}^{N}\left[\left(\frac{V_i - V_i^*}{\sigma(V)}\right)^2 + \left(\frac{I_i - I_i^*}{\sigma(V)}\right)^2\right]\right\}}$$

Where N is the number of data points measured and each pair of the fitted values (V_i^*, I_i^*) is related to the single diode equation 3.29 in chapter 3.

REFERENCES

Abelmann L. and Lodder C. (1997), Oblique evaporation and surface diffusion, *Thin Solid Films* **305** (1-2), 1-21.

Asbury J.B., Ellingson R.J., Ghosh H.N, Ferrere S., Nozik A.J. and Lian T.(1999), Femtosecond IR study of excited-state relaxation and electron-injection dynamics of $Ru(dcbpy)_2(NCS)_2$ in solution and on nanocrystalline TiO_2 and Al_2O_3 thin films, *J. Phys. Chem. B.* **103,** 3110-3119.

Aberle A.G., Wenham S.R. and Green M.A. (1993), A new method for accurate measurements of the lumped resistance of solar cells, Proc. 23rd *IEEE Photovoltaic Specialists Conference*, 10-14th May, Louisville, KY USA, 133-139.

Bach U., Lupo D., Comte P., Moser J.E., Weissorfel F., Salbeck J., Spreitzer H. and Gratzel M. (1998), Solid state dye-sensitized mesoporous TiO_2 solar cells with high photon-to-electron conversion efficiencies, *Nature* **395**, 583-585.

Barbe C.J., Arendse F., Comte P., Jironsek M., Lenzmann F., Shklover V. and Gratzel M. (1997), 'Nanocrystalline TiO_2 oxide electrodes for photovoltaic applications', *J. Am. Ceram. Soc.* **80**(12), 3157-71.

Bauer C., Boschloo G., Mukhtar E. and Hagfeldt A. (2002), Ultrafast studies of electron injection in Ru dye sensitized SnO_2 nanocrystalline film, *Intern. J. of Photoenergy* **4**, 17-20.

Becquerel E. (1839), Memmoire sur les effets electriques produits sous l'influence des rayons solaires, *C.R. Acad. Sci.* **9**, 561-567.

Bisquert J., Cahen D., Hodes G., Ruhle S. and Zaban A. (2004), Physical chemical principles of photovoltaic conversion with nanoparticulate, mesoporous dye-sensitized solar cells, *J. Phys. Chem. B* **108**, 8106-8118.

Boschloo G. and Hagfeldt A. (2005), Activation energy of electron transport in dye-sensitized TiO_2 solar cells, *J. Phys. Chem. B* **109** (24), 12093-12098.

Boschloo G., Lindstrom H., Magnusson E., Holmberg A. and Hagfeldt A. (2002), Optimizing of dye sensitized solar cell prepared by compression method, *J. Photochem. and Photobio. A: Chemistry* **148**, 11-15.

Brett M.J. (1988), Structural transitions in ballistic aggregation simulation of thin-film growth, *J. Vac. Sci. Technol, A* **6** (3), 1749-1751.

Burgers A.R. (2004), Fitting flash test curves with ECN'S I-V curve fitting program IVFIT, Report, Energy Research Centre of the Netherlands ECN. (http://www.ecn.nl/docs/library/report/2004/rx04007.pdf)

Burgers A.R., Eikelboom J.A., Schnecker A. and Sinke W.C (1996), Improved treatment of the strongly varying slope in fitting solar cell I-V curves, Report, Netherlands Energy Research Foundation, ECN (http://www.ecn.nl/docs/library/report/1996/rx96022.pdf).

Cameron P. J. and Peter L. M. (2003), Characterization of titanium dioxide blocking layers in dye-sensitized nanocrystalline solar cells, *J. Phys. Chem. B* **107**, 14394-14400.

Cameron P. J. and Peter L. M. (2005), How does back-reaction at the conducting glass substrate influence the dynamic photovoltage response of nanocrystalline dye-sensitized solar cells?, *J. Phys. Chem. B* **109** (15), 7392-7398.

Chaplin D.M., Fuller C.S and Pearson G.L. (1954), A new silicon *p-n* junction photocell for converting solar radiation into electrical power, *J. Appl. Phys.* **25** (5), 676-677.

Chapman B. (1980), Glow discharge processes: sputtering and plasma etching, John Wiley and Sons, New York, Pg 177-296.

Chopra K.L. and Das S.R (1983), Thin film solar cells, Plenum press, New York and London, 195-272.

Chopra K.L. and Kaur I. (1983), Thin film device applications, Plenum Press, New York, Pg 2-10.

Claesson S. and Holmstrom B. (1982), National Swedish Board for Energy Source Development, Project results: NE 1982: **14**,. Pg. 41-79.

Cullity B.D. (1959), *Elements of X-Ray Diffraction*, Addison-Wesley, Reading, pg 78-103.

de Blas M.A., Torres J.L., Prieto E. and Garcia A. (2002), Selecting a suitable model for characterizing photovoltaic devices, *Renewable Energy* **25**, 371-380.

de Jongh P.E. and Vanmaekelbergh D. (1996), Trap-limited electron transport in assemblies of nanometer-size TiO_2 particles, *Phys. Rev. Lett.* **77**, 16, 3427-3430.

de Jong P.E. and Vanmaekelbergh D. (1997), Investigation of the electronic transport properties of nanocrystalline particulate TiO_2 electrodes by intensity-modulated photocurrent spectroscopy, *J. Phys. Chem. B* **101**, 2716-2722.

Deloach J.D., Scarel G. and Aita C.R (1999) Correlation between titania film and structure and near ultraviolet optical absorption, *J. of Appl. Phys.* **85,** 4, 2377-2384.

Deshmukh M.K. and Deshmukh S.S. (2008), Modeling of hybrid renewable energy systems, *Renewable and sustainable energy reviews* **12**, 235-249.

Dick B., Brett M.J. and Smy T. (2003), Investigation of substrate rotation at glancing incidence on thin Film morphology, *J. Vac. Sci. Technol. B* **21**(6), 2569-2575.

Dirks A.G. and Leamy H.J. (1977) Columnar micro-structure in vapor-deposited thin films, *Thin Solid Films* **47**, 219-233.

Dimitrov D.B., Kaprinarova J., Pazov J. and Anglelov Ch. (2000), Conductivity of microporous magnetron sputtered thin TiO_2, *Vacuum* **58**, 344-350.

Dittrich T. (2000), Porous TiO_2: electron trnasport and application to dye sensitized injection solar cells, *Phys. Stat. Sol. (a)* **182**, 447-455.

Dloczik L., Ileperuma O., Lauermann I., Peter L.M., Ponomarev E.A., Redmond G., Shaw N.J. and Uhlendorf I. (1997). Dynamic response of dye-sensitized nano-crystalline solar cells: Characterization by intensity–modulated photocurrent spectroscopy, *J. Phys. Chem. B* **101**, 10281-10289.

Duffie J. and Beckman W. (1980), Solar energy engineering of thermal processes, Wiley New York, Pg 3-64.

Fabregat-Santiago F., Garcia-Belmonte G., Bisquert J., Zaban A. and Salvador P. (2002), Decoupling of transport, charge storage, and interfacial charge transfer in the nanocrystalline TiO_2 /electrolyte sSyatem by impedance methods, *J. Phys. Chem. B* **106**, 334-339.

Fabregat-Santiago F., Mora –Sero I, Garcia-Belmonte G., and Bisquert J. (2003), Cyclic voltammetry studies of nanoporous semiconductors: capacitive and reactive properties of nanocrystalline TiO_2 electrodes in aqueous electrolyte, *J. Phys. Chem. B* **107**, 758-768.

Fahmi A., Minot C, Silvi B and Cuasa M. (1993), Theoretical analysis of the structures of titanium dioxide crystals, *Phys. Rev. B* **47** (18), 11717 - 11724.

Ferber J. and Luther J. (1998), Computer simulations of light scattering and absorption in dye-sensitized solar cells, *Solar Energy Materials and solar cells* **54**, 265-275.

Ferber J., Stangl R. and Luther J. (1998), An electrical model of the dye sensitized solar cell, *Solar Energy Materials and solar cells* **53**, 29-54.

Ferroni M., Guidi V., Martinelli G. and Sherveglieri G. (1997), Microstructural characterization of a titanium-tungsten oxide gas sensor, *J. Mater. Res.* **12**, (3) 793-798.

Filip G. (2002), EasyFit ver. 2.3, Solar Lab, Wroclaw University of Technology, Wroclaw, Poland.

Finnie S.K., Barlett J.R. and. Woolfrey J.L (1998), Vibrational spectroscopic study of the coordination of (2,2'-Bipyridyl-4,4'-dicarboxylic acid)ruthenium(II) complexes to the surface of nanocrystalline titania, *Langmuir* **14**, 2744-2749.

Fisher A.C., Peter L.M., Ponomarev E.A., Walker A.B. and Wijayantha K.G.U. (2000), Intensity dependence of the back reaction and transport of electrons in dye-sensitized nanocrystalline TiO_2 solar cells, *J. Phys. Chem. B* **104**, 949-958.

Franco G., Gehring J., Peter L.M., Ponomarev E.A and Uhlendorf I. (1999), Frequency resolved optical detection of photoinduced electrons in dye-sensitized nanocrystalline photovoltaic cells, *J. Phys. Chem. B*, **103**, 692-698.

Gofuku E., Toyoda Y., Uehara Y., Kohara M. and Nunoshota M. (1991), Highly conductive TiO_2 thin films prepared by EB-modification, *Applied Surface Science* 48/49, 343-350.

Golego N., Studenikin S. A. and Cocivera M., (1999), Spray pyrolysis preparation of porous polycrystalline thin films of titanium dioxide containing Li and Nb, *J. Mater. Res.* **14**, 3, 698-707.

Gomez M. M. L. (2001), Photoelectrochemical and physical properties of sputter deposited titanium oxide electrodes: A new option for dye-sensitized nanocrystalline solar cells, PhD Thesis, National University of Engineering-Lima, Peru and Uppsala University, Sweden.

Gomez M., Magnusson E., Olsson E., Hagfeldt A., Lindquist S-E and Granqvist C.G. (2000[a]), Nanocrystalline Ti-oxidebased solar cells made by sputter deposition and dye sensitization: efficiency versus film thickness, *Solar Energy Materials and Solar Cells* **62**, 259-263.

Gomez M., Lu J., Olsson E., Hagfeldt A. and Granqvist C.G. (2000[b]), High efficiency dye-sensitized nanocrystalline solar cells based on sputter deposited Ti oxide films, *Solar Energy Materials and Solar Cells* **64**, 385-392.

Gomez M., Rodriguez J., Tingry S., Hagfeldt A., Lindquist S.-E. and Granqvist C.G. (1999[a]) Photoelectrochemical effect in dye sensitized sputter deposited Ti oxide films: the role of thickness - dependent roughness and porosity, *Solar Energy Materials and Solar Cells* **59**, 277-287.

Gomez M., Rodriquez J., Lindquist S-E and Granqvist C.G., (1999[b]), Photoelectrochemical studies of dye-sensitized polycrystalline titanium oxide thin films prepared by sputtering, *Thin Solid Films* **342**, 148-152.

Gratzel M. (1994), Dye sensitized solar cells, *J. Photochem. Photobiol. C: Photochem. Rev.* **4**, 145-153.

Gratzel M., Bonhote P., Fraser D., Kay A. and Rotzinger F. (1994), Development of a new type of solar cell based on sensitized nanocrystalline semiconducting films, Institute of Physics Chemistry II Swiss Federal Institute of Technology, Lausanne, Switzerland.

Gratzel M. (2000), Perspectives for dye-sensitized nanocrystalline solar cells, *Prog. Photovolt. Res. Appl.* **8**, 171-185.

Grätzel M. (2003), Dye-sensitized solar cells, *J. Photochem. Photobiol. C: Photochem Rev.* Vol: **4**, pp. 145-153.

Green M.A. (1992), Solar Cells: Operating principles, technology and system application, The University of South Wales, Kensington, Pg 62-204.

Green M.A., Emery K., Hisikawa Y. and Warta W. (2007), Solar cell efficiency tables (version 30), *Prog. Photovolt: Res. Appl.* **15**, 425-430.

Hagfeldt A. A. and Gratzel M. (2000), Molecular photovoltaics, *Acc. Chem. Res.* **33**, 269-277.

Hagfeldt A. and Gratzel M. (1995), Light-induced redox reactions in nanocrystalline systems, *Chem. Rev.* **95**, 49-68.

Hara K., Itoh K., Kamiya M., Okamoto K., Hashimoto T. and Fujiwara H. (1995), A new type of columnar grain structure in obliquely deposited films, *J. Magnetism and Magnetic Materials*, **148**, 19-20.

Heimer T. and .Heilwell E.J.,.Bignozzi C. A.and .Meyer G.J. (2000), Electron injection, recombination, and halide oxidation dynamics at dye-sensitized metal oxide interfaces, *J. of Phys. Chem. A* **104** (18), pp 4256-4262.

Heller A. and Miller B. (1980). Some Recent Progress in Semiconductor-liquid Junction Solar Cells, *Electrochimica Acta* **25**, 29-41.

Hore S. and Kern R. (2005), Implication of device functioning due to back reaction of electrons via the conducting glass substrate in dye sensitized solar cells, *Applied Physics Letters* **87**, 263504-1 - 263504-3.

http://solarcooking.org/saussure.htm, 17th December 2007

International Center for Diffraction Data, files 00-021-1272, 00-021-1276, 00-041-1445, 00-046-1088

Iqbal M. (1983), An introduction to solar radiation, Academic press, Toronto, Pg 335-373.

Kay A. and Gratzel M. (1996.), Low cost photovoltaic modules based on dye sensitized nanocrystalline titanium dioxide and carbon powder, *Solar Energy Materials and Solar Cells* **44** (1), 99-117.

Karunagaran B., Rajendra Kumar R.T., Viswanathan C., Mangalaraj D., Narayandass Sa. K. and Mohan Rao G. (2003), Optical constants of DC magnetron sputtered titanium dioxide thin films measured by spectroscopic ellipsometry, *Cryst. Res. Technol.* **38**, No. 9, 773-778.

Kiema G.K., Colgan M.J. and Brett M.J. (2005), Dye-sensitized solar cells incorporating obliquely deposited titanium oxide layers, *Solar Energy Materials and Solar Cells* **85**, 321-331.

Kim S.Y. (1996), Simultaneous determination of refractive index extinction coefficient and void distribution of titanium dioxide thin film by optical methods, *Applied Optics* **35** (34) 6703-6707.

Knorr T.G. and Hoffman R.W. (1959), Dependence of geometric magnetic anisotropy in thin iron films, *Phys. Rev.* **113** (4), 1039 – 1046.

Koide N., Ashraful Islam, Yasuo Chiba and Liyuan Han (2006), Improvement of efficiency of dye-sensitized solar cells based on analysis of equivalent circuit, *J. Photochem. Photobiol. A: Chemistry* **182**, 296-305.

Konenkamp R. (2000), Carrier transport in nanoporous TiO_2 films, *Phys. Rev. B.* **61**(16), 11057-11064.

Kroon J.M., Bakker N.J., Smit H.J.P., Liska P., Thampi K.R., Wang P., Zakeeruddin S.M., Gratzel M., Hinsch A., Hore S., Wurfel U., Sastrawan R., Durrant J.R., Palomares E., Petterson H., Gruszecki T., Waltyer J., Skupien K. and Tulloch G.E. (2007), Nanocrystalline dye-sensitized solar cells having maximum performance, *Prog. Photovolt: Res. Appl.* **15**, 1-18.

Lee S., Jun Y., Kim K. J. and Kim D. (2001), Modification of electrodes in nanocrystalline dye sensitized TiO_2 solar cells, *Solar Energy Materials and Solar Cells* **65**, 193-200.

Lee J.J., Coia G.M., and Lewis N.S. (2004), Current density vs. potential characteristics of dye-sensitized nanostructured semiconductor photoelectrodes. I. Analytical Expressions, *J. Phys. Chem. B* **108** *(17)*, 5269-5281.

Lee K-M., Suryanarayanan V. and Ho K-C (2007), A study on the electron transport properties of TiO_2 electrodes in dye-sensitize solar cells, *Solar energy Materials and Solar cells* **91**, 1416-1420.

Liang L., Dai S., Hu L., Kong F., Xu W. and Wang K. (2006), Porosity effects on electron transport in TiO_2 films and its application to dye-sensitized solar cells, *J. Phys. Chem. B*, **110**, 12404-12409.

Lokhande C. D. and Dhumre S. S., (1992), *Transcations of the SAEST* **27**, 2-3, 141-145.

Malac M., Egerton R.F., Brett M.J., and Dick B. (1999), Fabrication of submicrometer regular arrays of pillars and helices, *J. Vac. Sci. Technol. B* **17**(6), 2671-2674.

Mbise G.W., Le Bellac D., Niklasson G.A and Granqvist C.G. (1997), Angular selective window coatings: Theory and experiments, *J. Phys. D: Appl. Phys.* **30**, 2103-2122.

Memming R. (1980), Solar energy conversion by photoelectrochemical processes, *Electrochimica Acta* **25**, 77- 88.

Memming R. (2001). Semiconductor electrochemistry, Wiley-Vch, Weinheim, pg 46-60.

Meng L.J., Andritschky M. and dos Santos M. P. (1993), The effect of substrate temperature on the properties of d.c reactive magnetron sputtered titanium oxide films, *Thin Solid films* **223**, 242-247.

Messier R. and Lakhtakia A. (1999), Sculptured thin films II. Experiments and applications, *Mat. Res. Innovat.* **2**, 217- 222.

Messier R., Vijayakumar C.V. and Paul D.S. (2000), Origin and evolution of sculptured thin films, *J. Vac. Sci. Technol. A* **18** (4), 1538-1545.

Mills A. and Hunte S.L. (1997), An overview of semiconductor photocatalysis, *J. Photochem. Photobiol. A: Chem.* **108**, 1-35.

Muller K.H. (1985), Dependence of thin-film microstructure on deposition rate by means of a computer simulation, *J. Appl. Phys.* **58** (7), 2573-2576.

Nakade S., Saito Y., Kubo W., Kitamura T., Wada Y., Yanagida S. (2003), Influence of TiO_2 nanoparticle size on electron diffusion and recombination in dye-sensitized TiO_2 solar cells, *J. Phys. Chem. B*, **107**, 8607-8611.

Nazeeruddin K.M. (2006), Proceedings of the International summer school conference on advanced phosphorescent materials based on organic complexes of platinum group metals, Krutyn, Mazurian Lake District, Poland, 26 May - 2 June.

Nazeeruddin M.K., Pechy P., Renouard T., Zakeeruddin S.M., Humphr-Baker R., Comte P., Liska P., Cevey L., Costa E., Shklover V., Spiccia L., Deacon G.B., Bignozzi C.A. and Gratzel M. (2001), Engineering of efficient panchromatic sensitizers for nanocrystalline TiO_2-based solar cells, *J. Am. Chem. Soc.* **123** (8), 1613-1624.

Nazeeruddin M.K. Kay A., Rodicio I., Humphry-Baker R., Muller E., Liska P.,Vlachopoulos N. and Gratzel M. (1993), Conversion of light to electricity by cis-X_2Bis(2,2'-bipyridyl-4,4'-dicarboxylate) ruthenium(II) charge-transfer sensitizers (X=Cl^-, Br^-, I^-, CN^- and SCN^-) on nanocrystalline TiO_2 electrodes, *J. Am. Chem. Soc.* **115**, 6382-6390.

Nelson J., Eppler A. M. and Ballard I.M. (2002), Photoconductivity and charge trapping in porous nanocrystalline titanium dioxide, *J. Photochem. and Photobiol.y A: Chemistry* **148**, 25-31.

Nelson J., Haque S.A., Klug D.R. and Durrant J.R. (2001), Trap-limited recombination in dye sensitized nanocrystalline metal oxide electrode, *Physical Review B* **63**, 205321-205329.

Ni M., Leung M. K.H., Leung D. Y.C. and Sumathy K. (2006), An analytical study of the porosity effect on dye-sensitized solar cell performance, *Solar Energy Materials and Solar Cells* **90**, 1331-1344.

Oekermann T., Zhang D., Yoshida T. and Minoura H. (2004), Electron transport and back reaction in nanocrystalline TiO_2 films prepared by hydrothermal crystallization, *J. Phys. Chem. B* **108**, 2227-2235.

Ohring M. (1992), The materials science of thin films, Academic Press, New York, Pg 79-246.

O'Regan B. and Gratzel M. (1991), A Low-cost high efficiency solar cell based on dye-sensitized colloidal TiO_2 films, *Nature* **353**, 737-739.

Palomares E., Clifford J.N, Haque S.A Lutz. and Durrant J.R. (2003), Control of Charge recombination dynamics in dye sensitized solar cells by the use of conformally deposited metal oxide blocking layers, *J. Am. Chem. Soc.* **125** No. 2, 475-482.

Paritosh and Srolovitz D.J. (2002), Shadowing effects on the microstructure of obliquely deposited films, *J. Appl. Phys.* **91**(4), 1963-1972.

Patthey L., Rensmo H., Person P., Westermark K., Vayssieres L., Stashans A., Peterson A. Bruhwiler P.A, Siegbahn H., Lunell S. and Martensson N. (1999), Adsorption of bi-isonicotinic acid on rutile TiO_2 , *J. Chem.. Phys.* **110** (12), 5913-5918.

Paulsson H., Kloo L., Hagfeldt A and Boschloo G. (2006), Electron transport and recombination in dye-sensitized solar cells with ionic liquid electrolytes, *J. Electroanal. Chem.* **586** (1), 56-61.

Peng B., Gert J., Claus J.,Dietrich H., Hans-Werner S. and Thelakkat M. (2004), Systematic investigation of the role of compact TiO_2 layer in solid state dye-sensitized TiO_2 solar cells, *Coordination Chemistry Reviews* **248**, 1479-1489.

Peter L.M. and Wijayantha K.G.U. (1999), Intensity dependence of the electron diffusion length in dye-sensitized nanocrystalline TiO_2 photovoltaic cells, *Electrochemistry Communications* **1**, 576-580.

Peter L.M. and Wijayantha K.G.U (2000), Electron transport and back reaction in dye-sensitised nanocrystalline photovoltaic cells, *Electrochimica Acta* **45**, 4543-4551.

Pulker H.K., Paesold G. and Ritter E., (1976), Refractive indices of TiO_2 films produced by reactive evaporation of various titanium-oxygen phases, *Applied Optics* **15**, 12, 2986-2991.

Prince M.B. (1955), Silicon energy converters, *J. Appl. Phy.*, Vol. **26,** (5), 534-540.

Radecka M., Zakrzewska K., Czternastek H. and Stapinski T. (1993), The influence of thermal annealing on the structural, electrical and optical properties of TiO_{2-x} thin films, *Applied Surface Science* **65/66**, 227-234.

Rensmo H. (1998), Dye-sensitized nanostructured metal oxide electrodes: Photo electrochemical, quantum chemical and electron spectroscopic studies, Ph.D Thesis Department of Physical Chemistry, Uppsala University, Uppsalla, Pg. 9-48.

Rensmo H., Keis K., Lindstrom H., Sodergren S., Solbrand A., Hagfeldt A. and Lindquist S-E ; Wang L.N. and Muhammed M. (1997), High light-to-energy conversion efficiencies for solar cells based on nanostructured ZnO electrodes, *J. Phys. Chem. B* **110**, 2598-2601.

Rensmo H., Lunell S. and Siegbahn H. (1998), Absorption and electrochemical properties of ruthenium(II) dyes, studied by semiempirical quantum chemical calculations, *J. Photochem. Photobiol. A* **114** (2), 117-124.

Robbie K. and Brett M.J. (1997), Sculptured thin films and glancing angle deposition: growth mechanics and applications, *J. Vac. Sci. Technol. A* **15** (3), 1460-1465.

Robbie K., Friedrich L.J., Dew S.K., Smy T. and Brett M.J. (1995), Fabrication of thin films with highly porous microstructures, *J. Vac. Sci. and Tech. A* **13**(3), Pg 1032-1035.

Robbie K., Sit J.C., and Brett M.J. (1998), Advanced techniques for glancing angle deposition, *J. Vac. Sci. and Tech. B* **16**(3) 1115-1122.

Sayigh A.A.M. (1977), Solar energy engineering, Academic Press, New York, Pg. 1-50.

Sayigh A.A.M. (1991), Photovoltaic and solar radiation in: Generating electricity from the sun, Treble F.C. Pergamon Press, Oxford, 1st Ed., Pg 1-77.

Schlichthorl G., Huang S.Y., Sprague J. and Frank A.J. (1997), Band edge movement and recombination kinetics in dye-sensitized nanocrystalline TiO_2 solar cells: A study by intensity-modulated photovoltage spectroscopy, *J. Phys. Chem. B* **101**(41), 8141-8155.

Sit J.C., Vick D., Robbie K., Brett M.J. (1999), Thin film microstructure control using glancing angle deposition by sputtering, *J. Mater. Res.* **Vol. 14**, (4), Pg. 1197-1199.

Smith D.L. (1995), Thin film deposition, McGraw- Hill, New York, Pg 119-179.

Södergren S., Hagfeldt A., Olsson J. and Lindquist S-E (1994), Theoretical models for the action spectrum and the current-voltage characteristics of microporous semiconductor films in photoelectrochemical cells, *J. Phys. Chem.* **98** (21), 5552-5556.

Solbrand A., Henningsson A., Södergren S., Lindstrom H., Hagfeldt A. and Lindquist S-E (1999), Charge transport properties in dye sensitized nanostructred TiO_2 thin film electrodes studied by photoinduced current transients, *J. Phys. Chem. B* **103**, 1078-1083.

Solbrand A., Lindstrom H., Resnmo H., Hagfeldt A. and Lindquist S-E (1997), Electron transport in nanostructred TiO_2-electrolyte systems studied with time-resolved photocurrents, *J. Phys. Chem. B* **101**, 2514-2518.

Stefanovich E., Shidlovskaya E., Shluger A. and Zakharov M.A. (1990), Modification of the INDO calculation scheme and parametrization for ionic crystals, *Phys. Stat. Sol. B.* **160** (2), 529, Pg. 529-540.

Suzuki M. and Taga Y. (2001), Numerical study of the effective surface area of obliquely deposited thin films, *J. Appl. Phys.* Vol. **90**, (11) 5599-5605.

Szczyrbowski J., Brauer G., Ruske M., Bartella J., Schroeder J. and Zmelty A. (1999), Some properties of TiO_2 layers prepared by medium frequency reactive sputtering, *Surface and Coatings Technology* **112,** 261 – 266.

Sze S.M. (1969), Physics of semiconductor devices, Wiley – Interscience, Wiley International Edition, New York, Pg 132, 640-653.

Tait R.N., Smy T. and Brett M. J. (1993), Modelling and characterization of columnar growth in evaporated films, *Thin Solid Film* **226,** 196-201.

Takahashi J., Itoh H., and motai S. and Shimada S. (2003), Dye adsorption behavior of anatase-and rutile-type TiO_2 nanoparticles modified by various heat-treatments, *Journal of Material Science* **38**, 1695-1702.

Tang H., Prasad K., Sanjines R., Schmid P.E. and Levy F. (1994), Electrical and optical properties of TiO_2 anatase thin films, *J. Appl. Phys.* **75** (4) 2042-2047.

Tennakone K., Jayasundara B., Priyangi K., Mudiyanselage B., Gamaralalage R. Asoka K. and Akinori K.(2001), Enhanced efficiency of a dye-sensitized solar cell made from MgO-coated nanocrystalline SnO_2, *Jpn J.Appl. Phys.* **Vol. 40** part 2 No. 7B, pp L732-L734

Thornton J.A. (1986), The microstructure of sputter-deposited coatings, *J. Vac. Sci. Technol. A* **4**(6), 3059-3065.

Thornton J.A. (1974.), Influence of apparatus geometry and deposition conditions on the structure and topography of thick sputtered coatings, *J. Vac. Sci. Technol.* **11**(4), 666, Pg. 666-670.

Timoshenko V. Y., Duzhko V. and Dittrich Th. (2000), Diffusion voltage in porous semiconductors and dielectrics, *Phys. Stat. Sol. (A)* **182**, 227-232.

Usami A. and Ozaki H. (2001), Computer simulation of charge transport in dye-sensitized nanocrystalline photovoltaic cells, *J. Phys. Chem. B* **105,** 4577-4583.

van der Lagemaat J. and Frank A.J. (2000), Effect of the surface state distribution on electron transport in dye-sensitized TiO_2 solar cells: nonlinear electron – transport kinetics, *J. Phys. Chem. B* **104**, 4292-4294.

Vancoppenolle V., Jouan P-Y, Wantelet M. and Hecq Dauchot J-P. (1999), D.C. magnetron sputtering deposition of TiO_2 films in argon-gas mixtures: Theory and experiments, *Surface and Coatings Technolog*, **116-119**, 933-937.

Vossen J.L. and Cuomo J.J (1978), Glow discharge sputter deposition, Pg 12-62; and Waits R. K (1978), Planar magnetron sputtering, Pg 131-170 in: Vossen J.L and and R. Kern (1978), Thin film processes , Academic Press Inc., New York.

Wanzeller M. G., Alves R. N. C., Neto J. V. F. and Fonseca W. A. S. (2004), Current control loop for tracking of maximum power point supplied for photovoltaic array, *IEEE Transactions on Instrumentation and Measurement* Vol. **53** (4), Pg. 1304-1310.

Wasa K. and Hayakawa S. (1992), Handbook of sputter deposition: Principles and technology and applications, Noyes Park Ridge, USA, Pg. 49-80.

Watson D.F. and Meyer G.J.(2005), Electron injection at dye-sensitized semiconductor electrodes, *Annu. Rev. Phys Chem.* **56**, 119-156.

Weinberger B.R. and Garber R.B. (1995), Titanium dioxide photocatalysts produced by reactive magnetron sputtering, *Applied Physics Letters* **66**(18), 2409-2411.

Yang S., Quan X., Li X. and Sun C. (2006), Photoelectrocatalytic treatment of pentachlorophenol in aqueous solution using a rutile nanotube–like TiO_2/Ti electrode, *Photochem. Photobiol. Sci.* **5**, 808-814.

Zaban, A.; Greenshtein, M.; Bisquert, (2003), Determination of the electron lifetime in nanocrystalline dye solar cells by open-circuit voltage decay measurements, J. *Chem Phys Chem* **4**, 859-864.

Zhang J.Z. (2000), Interfacial charge carrier dynamics of colloidal semiconductor nanoparticles, *J. Phys. Chem. B* **104**, 7239-7253.

Zhang S., Zhu Y. F. and Brodie D. E., (1992), Photoconducting TiO_2 prepared by spray pyrolysis using $TiCl_4$, *Thin Solid Films* **213**, 265-270.